Università degli Studi di Trento
Dottorato di Ricerca in Ingegneria dei
Materiali e delle Strutture
XVI ciclo

ELASTOPLASTIC MODELS OF COMPACTION
OF GRANULAR MATERIALS

di
ANDREA PICCOLROAZ

Relatore: Prof. Davide Bigoni
Correlatori: Prof. John R. Willis, Prof. Alessandro Gajo

Trento, Gennaio 2004

Università degli Studi di Trento

Dottorato di Ricerca in Ingegneria dei Materiali e delle Strutture

XVI ciclo

Esame finale: 13 febbraio 2004

Commissione esaminatrice:

Prof. Guido Borino, Università di Palermo

Prof. Leone Corradi Dell'Acqua, Politecnico di Milano

Prof. Antonio Maria Cazzani, Università degli Studi di Trento

Membri esperti aggiunti:

Prof. Marc Bonnet, Ecole Polytechnique, Francia

Prof. Pedro Ponte Castañeda, University of Pennsylvania, Stati Uniti

Acknowledgements

This thesis would never have been written without the encouragement and incitement of my advisor, Prof. Davide Bigoni, whose support and general enthusiasm proved invaluable during the three years of my Ph.D. and, particularly, in the recent months.

I am indebted to Prof. John R. Willis for his supervision and for supporting me during my visit to the Department of Applied Mathematics and Theoretical Physics at the University of Cambridge during the period May–September 2003.

I wish to thank Prof. Alessandro Gajo for his comments and constructive criticisms about the topics of the thesis.

Special thanks also go to Dr. Stefano Guicciardi who contributed to the experimental work performed at CNR-ISTEC (Faenza, Italy).

I am deeply grateful to Prof. Giorgio Novati, head of the board of Professors of the Ph.D. course, and to all members of the group of mechanics at the University of Trento: Prof. Marco Rovati, Prof. Antonio Cazzani, Prof. Walter J. Drugan, Dr. Roberta Springhetti, Dr. Massimiliano Gei.

I dedicate this thesis to my parents.

Trento, January 2004

Andrea Piccolroaz

Contents

Chapter 1

Introduction

Powder compaction is a process in which granular materials are made cohesive through mechanical densification. This may or may not involve temperature and permit an efficient production of parts ranging widely in size and shape to close tolerances with low drying shrinkage (Reed, 1995). Metallurgical (German, 1984) and pharmaceutical (Lordi and Cuitiño, 1997) applications are common; moreover, forming of traditional (for instance: ceramic tiles, porcelain products) and structural ceramics (for instance: chip carriers, spark plugs, cutting tools) involves essentially powder compaction.

In the case of advanced ceramics, a ceramic powder is usually obtained through spray-drying and is made up of particles (granules) of dimensions ranging between 50 and 200 μm (Fig. 1.1), coated with the binder system.
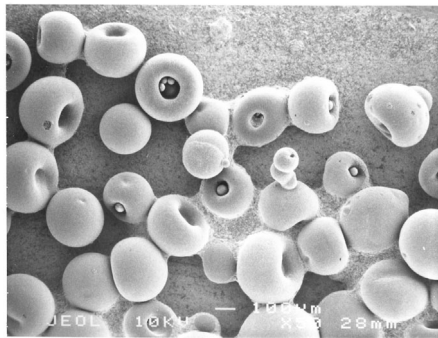
Figure 1.1: SEM micrograph of alumina powder (bar = 100 μm).

The granules are aggregates of crystals having dimensions on the order 1 μm.

Densification of ceramic powders induced by cold pressing can be divided in three main stages (Matsumoto, 1986; Reed, 1995; Bortzmeyer, 1996):

- **Phase I** granule sliding and rearrangement,

- **Phase II** granule deformation,

- **Phase III** granule densification.

The three phases of densification can be distinguished by the changes in the inclination of the semi-logarithmic plot of density versus applied pressure. These determine the "breakpoint pressure" and "joining pressure" points. The Phase I always occurs in early volumetric deformation of granular materials (at low stress), so that it has been thoroughly investigated for geomaterials. However, densification process in ceramic powders is often highly non homogeneous, so that usually at least two phases coexist. With reference to continuum mechanics modelling, Phases II and III of deformation are related to the gain in cohesion of the material and have been scarcely investigated.

Many technical, unresolved difficulties arise in the forming process of ceramic materials (Brown and Weber, 1988; Bortzmeyer, 1996). In fact, if on one hand the compact should result intact after ejection, should be handleable without failure and essentially free of macro defects, on the other hand, defects of various nature are always present in the greens (Deis and Lannutti, 1998; Ewsuk, 1997; Hausner and Kumar-Mal, 1982; Glass and Ewsuk, 1997; Thompson, 1981b), badly influencing local shrinkage during sintering (Deis and Lannutti, 1998; Hausner and Kumar-Mal, 1982). Defects can be caused by densification process, that may involve highly inhomogeneous strain fields, or by mold ejection, often producing end and ring capping, laminations, shape distortions, surface defects, vertical cracks, and large pores (Glass and Ewsuk, 1997).

In view of a reduction in the defects – crucial in setting the reliability of the final piece – simulations of the forming process become an important tool to optimize ceramics design (in terms of shape of final piece and type and composition of the powder).

This monograph is dedicated to the *development of a constitutive model capable of describing the mechanical behaviour of ceramic powders.* A phenomenological approach has been adopted, in the framework of the classical theory of plasticity. In particular, two fundamental features of the densification process are investigated: the increase in cohesion and the coupling between elastic and plastic properties.

Compaction of granular materials requires the description of the transition from a granular material (corresponding to Phase I) to a dense (Phase II) or, even, a fully-dense (Phase III) solid. *Since granular materials are characterized by peculiar properties, much different from dense solids, the constitutive modelling has to describe a transition between two remarkably different materials. A solution for this problem is provided in this monograph.*

The first step in developing an elastoplastic constitutive model is the adoption of a yield surface. This is done in Chapter 2, where *a new yield function has been proposed* for modelling the inelastic behaviour of granular materials and, more in general, quasibrittle and frictional materials. The formulation of the yield fuction has been made necessary by the observation that the proposed yield function allows the possibility of describing a transition between the shape of a yield surface typical of a class of materials to that typical of another class of materials. This peculiar feature is the fundamental key to model the behaviour of materials which become cohesive during hardening, such as ceramic powders, so that the shape of the yield surface evolves from that typical of a granular material to that typical of a dense material. No yield functions with this property were previously available.

The yield function —which is shown to fit very well experimental data relative to a broad class of materials including soils, concretes, rocks, metallic foams, porous metals, and polymers— represents a single, convex and smooth surface in stress space approaching as limit situations well-known criteria and the extreme limits of convexity in the deviatoric plane. The yield function is therefore a generalization of several criteria, including von Mises, Drucker-Prager, Tresca, modified Tresca, Coulomb-Mohr, modified Cam-clay, and — concerning the deviatoric section— Rankine and Ottosen. Convexity of the function is proved by developing two propositions relating convexity of the yield surface to convexity of the corresponding function. These proposition are general and therefore may be employed to generate other convex yield functions.

The elastoplastic coupling formulation (in the sense of Hueckel, 1976; Maier and Hueckel, 1979) needed to develop the constitutive model in a small strain formulation is introduced in Chapter 3. The use of elastoplastic coupling to model the densification process of granular materials may be motivated by the observation that elastic unloading in uniaxial deformation tests exhibits a tendency towards stiffening driven by increase in cohesion, as sketched in Fig. 1.2. In particular, *a new law for the elastic potential is formulated*, function of both elastic and plastic strains. When the cohesion is null, as in the
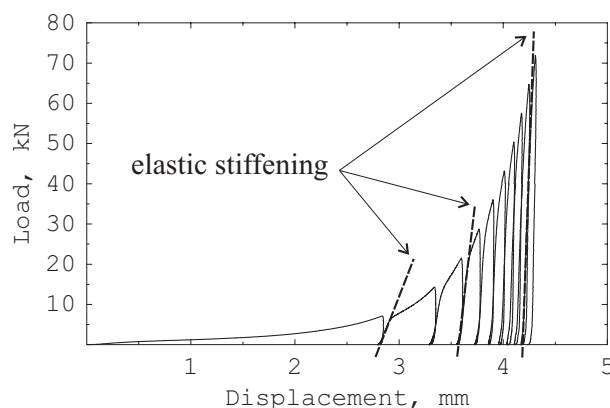
Figure 1.2: Elastic stiffening during uniaxial deformation test (experimental results on alumina powder).

case of ceramic powders during the Pashe I of densification, the elastic law reduces to that typical of granular materials [namely the elastic law employed in the Cam-clay model (Roscoe and Schofield, 1963; Roscoe and Burland, 1968)], but when the porosity decreases and consequently the cohesion increases, the elastic law approaches the usual linear elastic law, typical of a dense material.

Two hardening rules are introduced. The first one, relating forming pressure and material density, accounts for the compaction characteristics of ceramic powders. The second one, relating forming pressure and cohesion, accounts for the increase in cohesion during Phase II and III of compaction. The model has been calibrated on the basis of experimental results (partly already available and partly *ad hoc* performed) on an alumina powder. Finally, the model has been implemented employing the subroutine UMAT, available in the Finite Element general-purpose code ABAQUS, in order to simulate a simple forming process, which has been subsequently realized to validate the model capabilities.

In Chapter 4 the model is extended to a finite strain formulation. This may be motivated by the fact that large strains, up to 50%, are usually involved in the forming process of ceramic powders. A general constitutive framework for isothermal and time independent large elastoplastic deformations is presented following concepts developed by Hill and Rice (1973), Hill (1978) and Bigoni (2000). This general framework does not imply a particular choice of elastic and plastic strain decomposition, hypo- or hyper-elastic law,

flow and hardening rules, and therefore allows us to include the elastoplastic coupling already developed in small strain. In order to set up the constitutive model, we introduce: the multiplicative elastic and plastic decomposition; the requirement of isotropy of the elastic law; finally, the generalization to finite strains of the elastic potential, yield function, flow and hardening rules, which were introduced in Chapter 3 within the context of the infinitesimal theory. As a result, *a large-strain formulation is found of a model capable of describing the mechanical behaviour of a granular material becoming cohesive during compaction.* While remarking again that no similar model was available in the literature, we note that the given constitutive framework could also 'vice-versa' be used to describe degradation of cohesion due to damage in quasibrittle materials such as for instance concrete or cemented sands.

The modelling of forming of ceramic powders is concluded in Chapter 4, with the large strain formulation. It is however known that deformation of granular materials occurring during forming is accompanied by several material instabilities, occurring at different scales. Aimed at a clarification of this broad topic, the last part of the thesis (Chapter 5) has been devoted to a peculiar kind of material instability, the so-called 'flutter instability', which is thought to be characteristic of granular material, or, in other words of materials where the microscopic behaviour is dominated by Coulomb friction. This instability, precognized by Rice (1977) and studied by Loret (1992), Bigoni (1995), Bigoni and Loret (1999) and Loret et al. (2000), corresponds to the occurrence of two complex conjugate eigenvalues of the acoustic tensor and results still largely unknown. In particular, a clear mechanical interpretation of this isntability is still lacking. A rational step toward the clarification of this issue is performed in Chapter 5, where flutter instability is analyzed as the response of an infinite medium to a dynamic perturbation in terms of a pulsating force dipole superimposed upon a given uniform deformation. The infinite-body, dynamic Green's function is obtained for the plastic branch of a constitutive equation evidencing flutter and this is employed to produce the dipole providing the perturbation to the infinite medium. The response is investigated in various circumstances, including the case where the eigenvalues of the acoustic tensor are complex. It is shown that the response to the dynamic perturbation remains bounded until the eigenvalues lie in the real range, while a blow-up of the solution is detected as soon as the complex range is entered.

Chapter 2

Yield criteria for granular materials

2.1 Introduction

Yielding or damage of quasibrittle and frictional materials (a collective de-
nomination for soil, concrete, rock, granular media, coal, cast iron, ice, porous
metals, metallic foams, as well as certain types of ceramic) is complicated by
many effects, including dependence on the first and third stress invariants
(the so-called 'pressure-sensitivity' and 'Lode-dependence' of yielding), and
represents the subject of an intense research effort. Restricting attention to
the formulation of yield criteria, research moved in two directions: one was
to develop such criteria on the basis of micromechanics considerations, while
another was to find direct interpolations to experimental data. Examples of
yield functions generated within the former approach are numerous and, as
a paradigmatic case, we may mention the celebrated Gurson criterion (Gur-
son, 1977). The latter approach was also broadly followed, providing some
very successful yield conditions, such as for instance the Ottosen criterion
for concrete (Ottosen, 1977). Although very fundamental in essence, the mi-
cromechanics approach has limits however, particularly when employed for
geomaterials. For instance, it is usually based on variational formulations,
possible —for inelastic materials— only for solids obeying the postulate of
maximum dissipation at a microscale, which is typically violated for frictional
materials such as for instance soils.

A purely phenomenological point of view is assumed in the present work,
wherein a new yield function[1] is formulated, tailored to interpolate experi-

---

[0]This part is taken from Bigoni and Piccolroaz (2004) Yield criteria for quasibrittle and
frictional materials, in press.

[1]We need not distinguish here between yield, damage and failure. Within a phenomeno-

mental results for quasibrittle and frictional materials, under the assumption
of isotropy. The interest in this proposal lies in the features evidenced by the
criterion. These are:

- finite extent of elastic range both in tension and in compression;

- non-circular deviatoric section of the yield surface, which may approach
  both the upper and lower convexity limits for extreme values of material
  parameters;

- smoothness of the yield surface;

- possibility of stretching the yield surface to extreme shapes and related
  capability of interpolating a broad class of experimental data for different
  materials;

- reduction to known criteria in limit situations;

- convexity of the yield function (and thus of the yield surface);

- simple mathematical expression.

None of the above features is *essential*, in the sense that a plasticity theory can
be developed without all of the above, but all are *desirable* for the development
of certain models of interest, particularly in the field of geomaterials. This is
a crucial point, deserving a carefully explanation. In particular, while some of
the above requirements have a self-evident meaning, smoothness and convexity
need some discussion.

   Although experiments are inconclusive in this respect (Naghdi et al. 1958;
Paul, 1968; Phillips, 1974), theoretical speculations (sometimes criticized,
Naghdi and Srinivasa, 1994) suggest that corners should be expected to form
in the yield surface for single crystals and polycrystals (Hill, 1967a). There-
fore, smoothness of the yield surface might be considered a mere simplification
in the constitutive modelling of metals. However, the situation of quasibrittle
and frictional materials is completely different. For such materials, in fact,
evidence supporting corner formation is weak[2], so that, presently, smooth-
ness of the yield surface is a broadly employed concept and models developed
under this assumption are still very promising. Moreover, corners often are

logical approach, all these situations are based on the concept of stress range, bounded by
a given hypersurface defined in stress space.

   [2]Some argument in favour of corner formation in geomaterials have been given by Rud-
nicki and Rice (1975).

included in the constitutive description of a material for the mere fact that an appropriate, smooth yield function is simply not available (this is usually the case of the apex of the Drucker-Prager yield surface and of the corner which may exist at the intersection of a smooth, open yield surface with a cap).

Regarding convexity of the yield surface, we note that this follows for polycrystals from Schmid laws of single crystals (Bishop and Hill, 1951; Mandel, 1966). However, differently from smoothness, convexity is supported by experiments in practically all materials and is a useful mathematical property, which is the basis of limit analysis and becomes of fundamental importance in setting variational inequalities for plasticity (Duvaut and Lions, 1976). We may therefore conclude that —in the absence of a clear and specific motivation— it is not sensible to employ a yield function that violates convexity.

A number of failure surfaces have been proposed meeting some of the above requirements, among others, we quote the Willam and Warnke (1975), Ottosen (1977) and Hisieh et al. (1982) criteria for concrete, the Argyris et al. (1974), Matsuoka and Nakai (1977), Lade and Kim (1995), and Lade (1997) criteria for soils. For all these criteria, while some information can be found about the range of parameters corresponding to convexity of the yield *surfaces*, nothing is known about the convexity of the corresponding yield *functions*.

Convexity of a yield function implies convexity of the corresponding yield surface, but convexity of a level set of a function does not imply convexity of the function itself. While it can be pointed out that a convex yield function can *in principle* always be found to represent a convex yield surface, the 'practical problem' of finding it in a reasonably simple form may be a formidable one. From this respect, general propositions would be of interest, but the only contribution of which the authors are aware in this respect is quite recent (Mollica and Srinivasa, 2002). A purpose of the present work is to provide definitive results in this direction. In particular, the range of material parameters corresponding to convexity of the yield function proposed in this work is obtained by developing a general proposition that can be useful for analyzing convexity of a broad class of yield functions. The proposition is finally extended to introduce the possibility of describing a modification in shape of the deviatoric section with pressure. The propositions are shown to be constructive, in the sense that these may be employed to generate convex yield functions (examples of which are also included).

Beyond the issue of convexity, the central purpose of this work is the proposal of a yield criterion [see eqns. (2.6)–(2.9)]. This meets all of the above-listed requirements and can be viewed as a generalization of the following

criteria: von Mises, Drucker-Prager, Tresca, modified Tresca, Coulomb-Mohr, modified Cam-clay, Deshpande and Fleck (2000), Rankine, and Ottosen (1977) (the last two for the deviatoric section). Obviously, the criterion may account for situations which cannot be described by the simple criteria to which it reduces in particular cases. Several examples of this may be found in the field of granular media, where several *ad hoc* yield conditions have been proposed, which may describe *one peculiar material, but cannot describe another*. In the present work, it is shown with several examples that our yield criterion provides a unified description for a extremely broad class of quasi-brittle and frictional materials. Beyond the evident interest in generalization, there is a specific motivation for advocating the necessity of having a single criterion describing different materials. This lies in the fact that *during hardening, a yield surface may evolve from the shape typical of a certain material to that typical of another.* An evident example of this behaviour can be found in the field of granular materials, referring in particular to metal powders. These powders become cohesive during compaction, so that the material is initially a true granular material, but becomes finally a porous metal, whose porosity may be almost completely eliminated through sintering. The key to simulate this process is plasticity theory, so that a yield function must be employed evolving from the typical shape of a granular material ('triangular' deviatoric and 'drop-shaped' meridian sections), to that of a porous metal (circular deviatoric and elliptic meridian sections) and, in case of sintering, to that of a fully-dense metal (von Mises criterion). Another example of extreme shape variation of yield function during hardening is the process of decohesion of a rock-like material due to damage accumulation, a situation in a sense opposite to that described above. Evidently, a continuous distortion of the yield surface can be described employing the criterion proposed in this work and simply making material parameters depend on hardening.

2.2   A premise on Haigh-Westergaard representation

The analysis will be restricted to isotropic behaviour, therefore the Haigh-Westergaard representation of the yield locus is employed (Hill, 1950a). This is well-known, so that we limit the presentation here to a few remarks that may be useful in the following. First, we recall that:

$\mathcal{A}$1. a single point in the Haigh-Westergaard space is representative of the infinite (to the power three) stress tensors having the same principal values;

$\mathcal{A}$2. due to the arbitrariness in the ordering of the eigenvalues of a tensor, six different points correspond in the Haigh-Westergaard representation to a given stress tensor. As a result, the yield surface results symmetric about the projections of the principal axes on the deviatoric plane (Fig. 2.1);

$\mathcal{A}$3. the Haigh-Westergaard representation preserves the scalar product only between coaxial tensors;

$\mathcal{A}$4. a convex yield surface —for a material with a fixed yield strength under triaxial compression— must be internal to the two limit situations shown in Fig. 2.1 (Haythornthwaite, 1985). Note that the inner bound will be referred as 'the Rankine limit'.
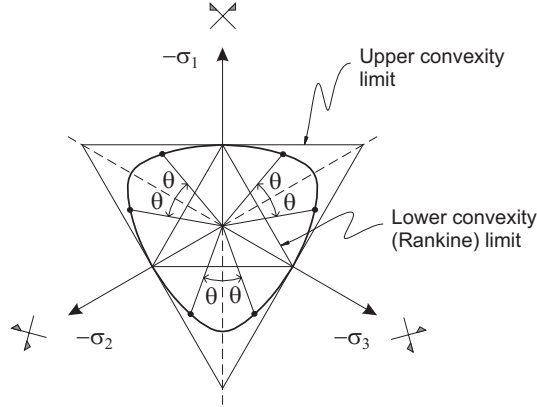
Figure 2.1: Deviatoric section: definition of angle θ, symmetries, lower and upper convexity bounds.

Due to isotropy, the analysis of yielding can be pursued fixing once and for all a reference system and restricting to all stress tensors diagonal in this system. We will refer to this setting as to the Haigh-Westergaard representation. When tensors (for instance, the yield function gradient) coaxial to the reference system are represented, the scalar product is preserved, property $\mathcal{A}$3. In the Haigh-Westergaard representation, the hydrostatic and deviatoric stress components are defined by the invariants

$$p = -\frac{\operatorname{tr}\boldsymbol{\sigma}}{3}, \quad q = \sqrt{3J_2}, \tag{2.1}$$

where

$$J_2 = \frac{1}{2}\boldsymbol{S} \cdot \boldsymbol{S}, \quad \boldsymbol{S} = \boldsymbol{\sigma} - \frac{\operatorname{tr}\boldsymbol{\sigma}}{3}\boldsymbol{I}, \tag{2.2}$$

in which $\boldsymbol{S}$ is the deviatoric stress, $\boldsymbol{I}$ is the identity tensor, a dot denotes scalar product and tr denotes the trace operator, so that $\boldsymbol{A} \cdot \boldsymbol{B} = \operatorname{tr} \boldsymbol{A} \boldsymbol{B}^T$, for every second-order tensors $\boldsymbol{A}$ and $\boldsymbol{B}$. The position of the stress point in the deviatoric plane is singled out by the Lode (1926) angle θ defined as

$$\theta = \frac{1}{3} \cos^{-1} \left(\frac{3\sqrt{3}}{2} \frac{J_3}{J_2^{3/2}} \right), \quad J_3 = \frac{1}{3} \operatorname{tr} \boldsymbol{S}^3, \tag{2.3}$$

so that $\theta \in [0, \pi/3]$. As a consequence of property $(\mathcal{A}2)$ of the Haigh-Westergaard representation, a single value of θ corresponds to six different points in the deviatoric plane (Fig. 2.1). The following gradients of the invariants, that will be useful later,

$$\frac{\partial p}{\partial \boldsymbol{\sigma}} = -\frac{1}{3} \boldsymbol{I}, \quad \frac{\partial J_2}{\partial \boldsymbol{\sigma}} = \boldsymbol{S}, \quad \frac{\partial J_3}{\partial \boldsymbol{\sigma}} = \boldsymbol{S}^2 - \frac{\operatorname{tr} \boldsymbol{S}^2}{3} \boldsymbol{I},$$

$$\frac{\partial \theta}{\partial \boldsymbol{\sigma}} = -\frac{9}{2q^3 \sin 3\theta} \left(\boldsymbol{S}^2 - \frac{\operatorname{tr} \boldsymbol{S}^2}{3} \boldsymbol{I} - q \frac{\cos 3\theta}{3} \boldsymbol{S} \right), \tag{2.4}$$

can be obtained from well-known formulae (e.g. Truesdell and Noll, 1965, Sect. 9) using the identity

$$\frac{\partial \boldsymbol{S}}{\partial \boldsymbol{\sigma}} = \boldsymbol{I} \,\overline{\underline{\otimes}}\, \boldsymbol{I} - \frac{1}{3} \boldsymbol{I} \otimes \boldsymbol{I}, \tag{2.5}$$

where the symbol $\otimes$ denotes the usual dyadic product and $\boldsymbol{I} \,\overline{\underline{\otimes}}\, \boldsymbol{I}$ is the symmetrizing fourth-order tensor, defined for every tensor $\boldsymbol{A}$ as

$$(\boldsymbol{I} \,\overline{\underline{\otimes}}\, \boldsymbol{I})[\boldsymbol{A}] = \frac{\boldsymbol{A} + \boldsymbol{A}^T}{2}.$$

Note that $\partial \theta / \partial \boldsymbol{\sigma}$ is orthogonal to $\boldsymbol{I}$ and to the deviatoric stress $\boldsymbol{S}$.

2.3   A new yield function

We propose the seven-parameters yield function $F : \mathsf{Sym} \to \mathbf{R} \cup \{+\infty\}$ defined as:

$$F(\boldsymbol{\sigma}) = f(p) + \frac{q}{g(\theta)}, \tag{2.6}$$

where the dependence on the stress $\boldsymbol{\sigma}$ is included in the invariants p, q and θ, eqns. (2.1) and (2.3), through the 'meridian' function

$$f(p) = \begin{cases} -Mp_c \sqrt{(\Phi - \Phi^m)\left[2(1 - \alpha)\Phi + \alpha\right]} & \text{if } \Phi \in [0, 1], \\ \\ +\infty & \text{if } \Phi \notin [0, 1], \end{cases} \tag{2.7}$$

where

$$\Phi = \frac{p + c}{p_c + c},\tag{2.8}$$

describing the pressure-sensitivity[3] and the 'deviatoric' function

$$g(\theta) = \frac{1}{\cos\left[\beta\frac{\pi}{6} - \frac{1}{3}\cos^{-1}\left(\gamma\cos 3\theta\right)\right]},\tag{2.9}$$

describing the Lode-dependence of yielding. The seven, non-negative material parameters:

$$\underbrace{M > 0, \ p_c > 0, \ c \geq 0, \ 0 < \alpha < 2, \ m > 1}_{\text{defining } f(p)}, \quad \underbrace{0 \leq \beta \leq 2, \ 0 \leq \gamma < 1}_{\text{defining } g(\theta)}, \quad (2.10)$$

define the shape of the associated (single, smooth) yield surface. In particular, M controls the pressure-sensitivity, p_c and c are the yield strengths under isotropic compression and tension, respectively. Parameters α and m define the distortion of the meridian section, whereas β and γ model the shape of the deviatoric section. Note that the deviatoric function describes a piecewise linear deviatoric surface in the limit $\gamma \longrightarrow 1$. Finally, it is important to remark that within the interval of $\beta \in [0, 2]$ the yield function is convex independently of the values assumed by parameter γ. Convexity requirements, that will be proved later, impose a broader variation of β than $(2.10)_6$, but the interval where β may range becomes a function of γ. In particular, the yield function is convex when

$$2 - \mathcal{B}(\gamma) \leq \beta \leq \mathcal{B}(\gamma),\tag{2.11}$$

where function $\mathcal{B}(\gamma)$ takes values within the interval $]2, 4]$, when γ ranges in $[0, 1[$ and is defined as

$$\mathcal{B}(\gamma) = 3 - \frac{6}{\pi}\tan^{-1}\frac{1 - 2\cos z - 2\cos^2 z}{2\sin z(1 - \cos z)}\bigg|_{z=2/3(\pi-\cos^{-1}\gamma)}.\tag{2.12}$$

The yield function (2.6) corresponds to the following yield surface:

$$q = -f(p)g(\theta), \quad p \in [-c, p_c], \quad \theta \in [0, \pi/3],\tag{2.13}$$

---

[3]The meridian function can be written in an alternative form by using the Macauley bracket operator, defined for every scalar α as $< \alpha >= \max\{0, \alpha\}$, and the indicator function $\chi_{[0,1]}(\Phi)$, which takes the value 0 when $\Phi \in [0, 1]$ and is equal to $+\infty$ otherwise

$$f(p) = -Mp_c\sqrt{\left(\tilde{\Phi} - \tilde{\Phi}^m\right)\left[2(1 - \alpha)\tilde{\Phi} + \alpha\right]} + \chi_{[0,1]}(\Phi), \quad \tilde{\Phi} = < \Phi > - < \Phi - 1 > .$$

which makes explicit the fact that $f(p)$ and $g(\theta)$ define the shape of the meridian and deviatoric sections, respectively.

The yield surface (2.13) is sketched in Figs. 2.2–2.3 for different values of the seven above-defined material parameters (non-dimensionalization is introduced through division by p_c in Fig. 2.2). In particular, meridian sections are reported in Figs. 2.2 ($g(\theta) = 1$ has been taken), whereas Fig. 2.3 pertains to deviatoric sections.
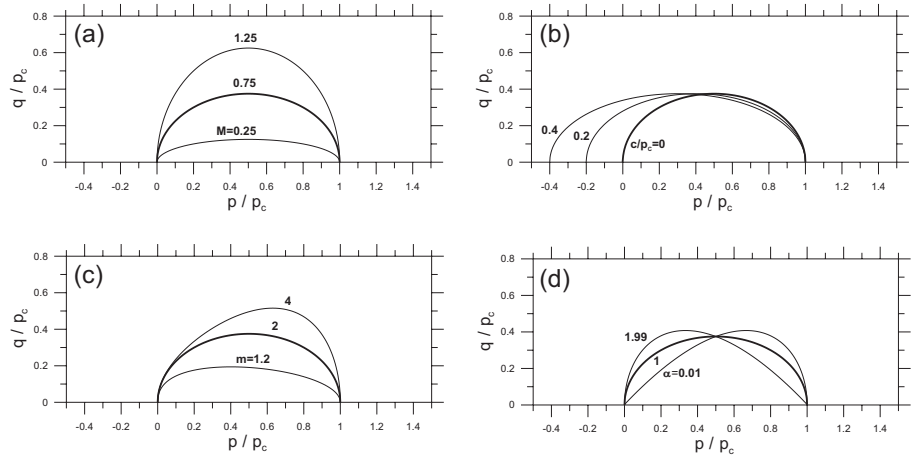
Figure 2.2: Meridian section: effects related to the variation of parameters M (a), c/p_c (b), m (c), and α (d).

As a reference, the case corresponding to the modified Cam-clay introduced by Roscoe and Burland (1968) and Schofield and Wroth (1968) and corresponding to $\beta = 1$, $\gamma = 0$, $\alpha = 1$, $m = 2$, and $c = 0$ is reported in Fig. 2.2 as a solid line, for $M = 0.75$. The distortion of meridian section reported in Fig. 2.2 (a) —where $M = 0.25, 0.75, 1.25$— can also be obtained within the framework of the modified Cam-clay, whereas the effect of an increase in cohesion reported in Fig. 2.2 (b) —where $c/p_c = 0, 0.2, 0.4$— may be employed to model the gain in cohesion consequent to plastic strain, during compaction of powders.

The shape distortion induced by the variation of parameters m and α, Fig. 2.2 (c) —where $m = 1.2, 2, 4$— and (d) —where $\alpha = 0.01, 1.00, 1.99$— is crucial to fit experimental results relative to frictional materials.

A unique feature of the proposed model is the possibility of extreme shape distortion of the deviatoric section, which may range between the upper and
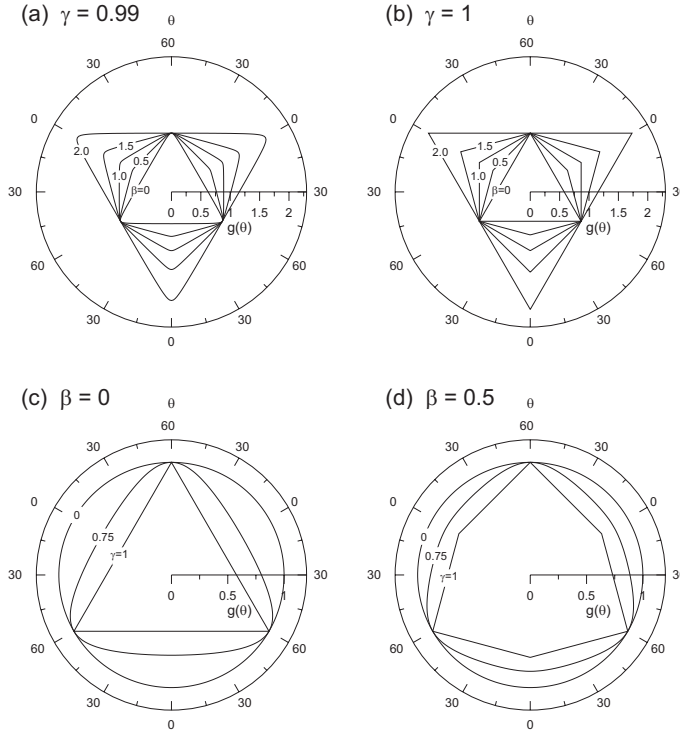
Figure 2.3: Deviatoric section: effects related to the variation of β and γ. Variation of $\beta = 0, 0.5, 1, 1.5, 2$ at fixed $\gamma = 0.99$ (a) and $\gamma = 1$ (b). Variation of $\gamma = 1, 0.75, 0$ at fixed $\beta = 0$ (c) and $\beta = 0.5$ (d).

lower convexity limits, and approach Tresca, von Mises and Coulomb-Mohr. This is sketched in Fig. 2.3, where to simplify reading of the figure, function $g(\theta)$ has been normalized through division by $g(\pi/3)$, so that all deviatoric sections coincide at the point $\theta = \pi/3$. The use of our model may therefore allow one to simply obtain a convex, smooth approximation of several yielding criteria (Tresca and Coulomb-Mohr, for instance). If this may be not substantial from theoretical point of view, it clearly avoids the necessity of introducing independent yielding mechanisms.

Parameter γ is kept fixed in Figs. 2.3 (a) and (b) and equal to 0.99 and 1, respectively, whereas parameter β is fixed in Figs. 2.3 (c) and (d) and equal to 0 and 1/2. Therefore, figures (a) and (b) demonstrate the effect of the variation in β (= 0, 0.5, 1, 1.5, 2) which makes possible a distortion of the

yield surface from the upper to lower convexity limits going through Tresca and Coulomb-Mohr shapes. The role played by γ (= 1, 0.75, 0) is investigated in figures (c) and (d), from which it becomes evident that γ has a smoothing effect on the corners, emerging in the limit $\gamma = 1$. The von Mises (circular) deviatoric section emerges when $\gamma = 0$.

The yield surface in the biaxial plane σ_1 versus σ_2, with $\sigma_3 = 0$ is sketched in Fig. 2.4, where axes are normalized through division by the uniaxial tensile strength f_t. In particular, the figure pertains to $M = 0.75$, $p_c = 50c$, $m = 2$, and $\alpha = 1$, whereas $\gamma = 0.99$ is fixed and β is equal to $\{0, 0.5, 1, 1.5, 2\}$ in Fig. 2.4 (a) and, vice-versa, $\beta = 0$ is fixed and γ is equal to $\{0, 0.75, 0.99\}$ in Fig. 2.4 (b).
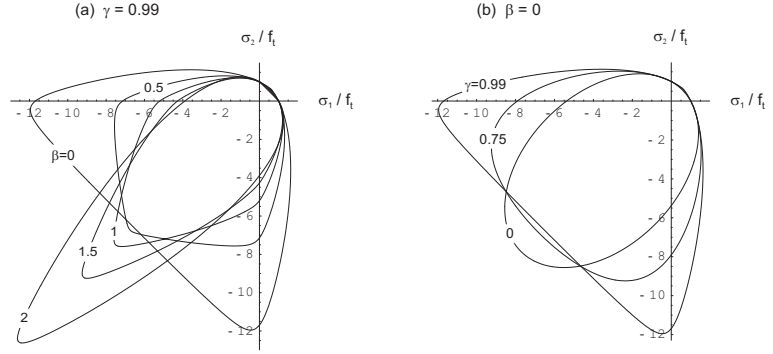
Figure 2.4: Yield surface in the biaxial plane σ_1/f_t vs. σ_2/f_t, with $\sigma_3 = 0$. Variation of $\beta = 0, 0.5, 1, 1.5, 2$ at fixed $\gamma = 0.99$ (a) and variation of $\gamma = 0, 0.75, 0.99$ at fixed $\beta = 0$ (b).

2.3.1   Smoothness of the yield surface

Smoothness of yield surface (2.13) within the interval of material parameters defined in (2.10)–(2.11) can be proved considering the yield function gradient. This can be obtained from (2.4) in the form

$$\frac{\partial F}{\partial \boldsymbol{\sigma}} = a(p)\boldsymbol{I} + b(\theta)\tilde{\boldsymbol{S}} + c(\theta)\tilde{\boldsymbol{S}}^{\perp}, \tag{2.14}$$

where

$$\tilde{\boldsymbol{S}} = \sqrt{\frac{3}{2}}\frac{\boldsymbol{S}}{q}, \quad \tilde{\boldsymbol{S}}^{\perp} = -\sqrt{\frac{2}{3}}q\frac{\partial \theta}{\partial \boldsymbol{\sigma}} = \frac{1}{\sin 3\theta}\left[\sqrt{6}\left(\tilde{\boldsymbol{S}}^2 - \frac{1}{3}\boldsymbol{I}\right) - \cos 3\theta\tilde{\boldsymbol{S}}\right], \tag{2.15}$$

and

$$
\begin{aligned}
a(p) &= \frac{Mp_c}{3(p_c + c)} \frac{\left(1 - m\Phi^{m-1}\right)\left[2(1-\alpha)\Phi + \alpha\right] + 2(1-\alpha)\left(\Phi - \Phi^m\right)}{2\sqrt{(\Phi - \Phi^m)\left[2(1-\alpha)\Phi + \alpha\right]}}, \\
b(\theta) &= \sqrt{\frac{3}{2}}\frac{1}{g(\theta)}, \\
c(\theta) &= -\frac{\sqrt{3}\gamma \sin 3\theta}{\sqrt{2}\sqrt{1 - \gamma^2 \cos^2 3\theta}} \sin\left[\beta\frac{\pi}{6} - \frac{1}{3}\cos^{-1}(\gamma \cos 3\theta)\right].
\end{aligned}
\tag{2.16}
$$

It should be noted that $c(0) = c(\pi/3) = 0$ and that $\tilde{\boldsymbol{S}}$ and $\tilde{\boldsymbol{S}}^{\perp}$ are unit norm, coaxial and normal to each other tensors.[4] Coaxiality and orthogonality are immediate properties, whereas the proof that $|\tilde{\boldsymbol{S}}^{\perp}| = 1$ is facilitated when the following identities are taken into account

$$
\tilde{\boldsymbol{S}}^3 - \frac{1}{2}\tilde{\boldsymbol{S}} - \frac{\cos 3\theta}{3\sqrt{6}}\boldsymbol{I} = \boldsymbol{0}, \quad \rightsquigarrow \quad \tilde{\boldsymbol{S}}^2 \cdot \tilde{\boldsymbol{S}}^2 = \frac{1}{2},
\tag{2.17}
$$

the former of which is the Cayley-Hamilton theorem written for $\tilde{\boldsymbol{S}}$. Let us consider now from (2.14) the unit-norm yield function gradient

$$
\boldsymbol{Q} = \frac{a}{\sqrt{3a^2 + b^2 + c^2}}\boldsymbol{I} + \frac{b}{\sqrt{3a^2 + b^2 + c^2}}\tilde{\boldsymbol{S}} + \frac{c}{\sqrt{3a^2 + b^2 + c^2}}\tilde{\boldsymbol{S}}^{\perp},
\tag{2.18}
$$

defining, for stress states satisfying $F(\boldsymbol{\sigma}) = 0$, the unit normal to the yield surface. The following limits can be easily calculated

$$
\lim_{\Phi \to 0^+} \boldsymbol{Q} = \frac{1}{\sqrt{3}}\boldsymbol{I}, \qquad \lim_{\Phi \to 1^-} \boldsymbol{Q} = -\frac{1}{\sqrt{3}}\boldsymbol{I},
\tag{2.19}
$$

so that the yield surface results to be smooth at the limit points where the hydrostatic axis is met. Moreover, smoothness of the deviatoric section of the yield surface is proved observing that

$$
\lim_{\theta \to 0, \pi/3} \boldsymbol{Q} = \frac{a}{\sqrt{3a^2 + b^2}}\boldsymbol{I} + \frac{b}{\sqrt{3a^2 + b^2}}\tilde{\boldsymbol{S}},
\tag{2.20}
$$

where $\tilde{\boldsymbol{S}}$ and b are evaluated at $\theta = 0$ and $\theta = \pi/3$, and noting that $\tilde{\boldsymbol{S}}$ and $\tilde{\boldsymbol{S}}^{\perp}$ are coaxial, deviatoric tensors so that they are represented by two orthogonal

---

[4]Note that $c\tilde{\boldsymbol{S}}^{\perp} = \boldsymbol{0}$ at $\theta = 0, \pi/3$. This can be deduced from the fact that $|\tilde{\boldsymbol{S}}^{\perp}| = 1$ and $c = 0$ for $\theta = 0, \pi/3$ or, alternatively, can be proved directly observing that for $\theta = 0, \pi/3$ the deviatoric stress can be generically written as $\{S_1, -S_1/2, -S_1/2\}$, unless all (uninfluent) permutations of components.

vectors in the deviatoric plane in the Haigh-Westergaard stress space. We
observe, finally, that limits (2.19) do not hold true when α equals 0 and 2
and that limits (2.20) does not hold true when $\gamma = 1$. In particular, a corner
appears at the intersection of the yield surface with the hydrostatic axis in the
former case and the deviatoric section becomes piecewise linear in the latter.

2.3.2   Reduction of yield criterion to known cases

The yield function (2.6)–(2.9) reduces to almost all[5] 'classical' criteria of yield-
ing. These can be obtained as limit cases in the way illustrated in Tab. 2.1
where the modified Tresca criterion was introduced by Drucker (1953), whereas
the Haigh-Westergaard representation of the Coulomb-Mohr criterion was pro-
posed by Shield (1955). In Tab. 2.1 parameter r denotes the ratio between
the uniaxial strengths in compression (taken positive) and tension, indicated
by f_c and f_t, respectively. We note that for real materials $r \geq 1$ and that we
did not explicitly consider the special cases of no-tension $f_t = 0$ or granular
$f_t = f_c = 0$ materials [which anyway can be easily incorporated as limits of
(2.6)–(2.9)].

   We note that the expression of the Tresca criterion which follows from
(2.6)–(2.9) in the limits specified in Tab. 2.1, was provided also by Bardet
(1990) and answers —in a positive way— the question (raised by Salençon,
1974) if a proper[6] form of the criterion in terms of stress invariants exist.

   The Mohr-Coulomb limit merits a special mention. In fact, if the following
values of the parameters are selected

$$\alpha = 0, \quad c = \frac{f_c \left[\cos\left(\beta\frac{\pi}{6} - \frac{\pi}{3}\right) + \cos\beta\frac{\pi}{6} \right]}{3r\cos\left(\beta\frac{\pi}{6} - \frac{\pi}{3}\right) - 3\cos\beta\frac{\pi}{6}},$$
$$M = \frac{3\left[r\cos\left(\beta\frac{\pi}{6} - \frac{\pi}{3}\right) - \cos\beta\frac{\pi}{6} \right]}{\sqrt{2}(r+1)}, \tag{2.21}$$

---

[5]A remarkable exception is the isotropic Hill (1950b) criterion, corresponding to a Tresca
criterion rotated of $\pi/6$ in the deviatoric plane.

[6]The expression

$$f(\boldsymbol{\sigma}) = 4J_2^3 - 27J_3^2 - 36k^2J_2^2 + 96k^4J_2 - 64k^6,$$

where k is the yield stress under shear (i.e. $k = f_t/2$), reported in several textbooks on
plasticity, is definitively wrong. This can be easily verified taking a stress state belonging to
one of the planes defining the Tresca criterion, but outside the yield locus, for instance, the
point $\{\sigma_1 = 0, \ \sigma_2 = -2k, \ \sigma_3 = 2k\}$, corresponding to $J_2 = 4k^2$ and $J_3 = 0$. Obviously, the
point lies well outside the yield locus, but satisfies $f(\boldsymbol{\sigma}) = 0$, when the above, wrong, yield
function is used.

Table 2.1: Yield criteria obtained as special cases of (2.6)–(2.9), $r = f_c/f_t$ and f_c and f_t are the uniaxial strengths in compression and tension, respectively.

Criterion	Meridian function $f(p)$	Deviatoric function $g(\theta)$
von Mises	$\alpha = 1, \qquad m = 2,$ $M = \dfrac{2f_t}{p_c}, \quad c = p_c \longrightarrow \infty$	$\beta = 1, \gamma = 0$
Drucker-Prager	$\alpha = 0, \qquad M = \dfrac{3(r-1)}{\sqrt{2}(r+1)},$ $c = \dfrac{2f_c}{3(r-1)}, \quad p_c = f_c m \longrightarrow \infty$	as for von Mises
Tresca	as for von Mises, except that $M = \dfrac{\sqrt{3}f_t}{p_c}$	$\beta = 1, \gamma \longrightarrow 1$
mod. Tresca	as for Drucker-Prager, except that $M = \dfrac{3\sqrt{3}(r-1)}{2\sqrt{2}(r+1)}$	as for Tresca
Coulomb-Mohr	as for Drucker-Prager, except that $M = \dfrac{3\left[r\cos\left(\beta\frac{\pi}{6} - \frac{\pi}{3}\right) - \cos\beta\frac{\pi}{6}\right]}{\sqrt{2}(r+1)}$ $c = \dfrac{f_c\left[\cos\left(\beta\frac{\pi}{6} - \frac{\pi}{3}\right) + \cos\beta\frac{\pi}{6}\right]}{3r\cos\left(\beta\frac{\pi}{6} - \frac{\pi}{3}\right) - 3\cos\beta\frac{\pi}{6}}$	$\beta = \dfrac{6}{\pi}\tan^{-1}\dfrac{\sqrt{3}}{2r+1},$ $\gamma \longrightarrow 1$
mod. Cam-clay	$m = 2, \ \alpha = 1, \ c = 0$	as for von Mises

and then the limits

$$\gamma \longrightarrow 1, \quad p_c = f_c m \longrightarrow \infty, \tag{2.22}$$

are performed, a three-parameters generalization of Coulomb-Mohr criterion is obtained, which reduces to the latter criterion in the special case when β is selected in the form specified in Tab. 2.1 (yielding an expression noted also

by Chen and Saleeb, 1982).

The cases reported in Tab. 2.1 refer to situations in which the criterion (2.6)–(2.9) reduces to known yield criteria both in terms of function $f(p)$ and of function $g(\theta)$. It is however important to mention that the Lode's dependence function $g(\theta)$ reduces also to well-known cases, but in which the pressure-sensitivity cannot be described by the meridian function (2.7). These are reported in Tab. 2.2. It is important to mention that the form of our function $g(\theta)$, eqn. (2.9), was indeed constructed as a generalization of the deviatoric function introduced by Ottosen (1977).

Table 2.2: Deviatoric yield functions obtained as special cases of (2.9)

Criterion	Deviatoric function $g(\theta)$
Lower convexity (Rankine)	$\beta = 0, \quad \gamma \longrightarrow 1$
Upper convexity	$\beta = 2, \quad \gamma \longrightarrow 1$
Ottosen	$\beta = 0, \quad 0 \leq \gamma < 1$

2.3.3   A comparison with experiments

A brief comparison with experimental results referred to several materials is reported below. We limit the presentation to a few representative examples demonstrating the extreme flexibility of the proposed model to fit experimental results. In particular, we concentrate on the meridian section, whereas only few examples are provided for the deviatoric section, which has a shape so deformable and ranging between well-known forms that fitting experiments is a-priori expected. Results on the biaxial plane $\sigma_1 - \sigma_2$ are also included.

Typical of soils are the experimental results reported in Fig. 2.5, on Aio dry sand and Weald clay, taken, respectively, from Yasufuku et al. (1991, their Fig. 10a) and Parry (reported by Wood, 1990, their Fig. 7.22, so that p_e is the equivalent consolidation pressure in Fig. 2.5 (b)). Note that the upper plane of the graphs refers to triaxial compression ($\theta = \pi/3$), whereas triaxial extension
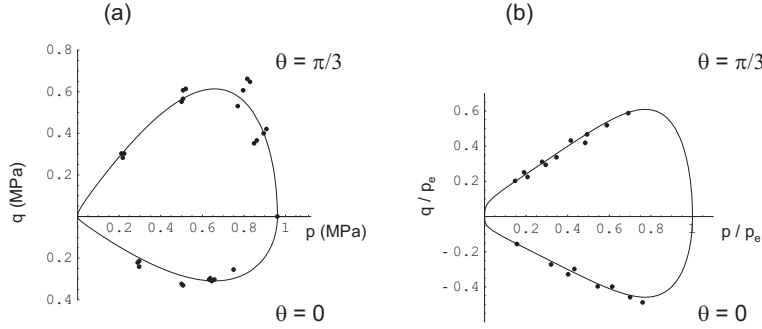
Figure 2.5: Comparison with experimental results relative to sand (Yasufuku et al. 1991) (a) and clay (Parry, reported by Wood, 1990) (b).

is reported in the lower part of the graphs ($\theta = 0$). It may be concluded from the figure that experimental results can be easily fitted by our function $f(p)$, still maintaining a smooth intersection of the yield surface with $p-$axis.

In addition to soils, the proposed function (2.6)–(2.9) can model yielding of porous ductile or cellular materials, metallic and composite powders, concrete and rocks. To further develop this point, a comparison with experimental results given by Sridhar and Fleck (2000) —their Figs. 5(b) and 9(c)— relative to ductile powders is reported in Fig. 2.6. In particular, Fig. 2.6 (a) is relative to an aluminum powder (Al $D_0 = 0.67$, $D = 0.81$ in Sridhar and Fleck, their Fig. 5b), Fig. 2.6 (b) to an aluminum powder reinforced by 40 vol.%SiC (Al-40%Sic $D_0 = 0.66$, $D = 0.82$ in Sridhar and Fleck, their Fig. 5b), Fig. 2.6 (c) to a lead powder (0% steel in Sridhar and Fleck, their Fig. 9c), and Fig. 2.6 (d) to a lead shot-steel composite powder (20% steel in Sridhar and Fleck, their Fig. 9c). Beside the fairly good agreement between experiments and proposed yield function, we note that the aluminium powder has a behaviour —different from soils and lead-based powders— resulting in a meridian section of the yield surface similar to the early version of the Cam-clay model (Roscoe and Schofield, 1963).

Regarding concrete, among the many experimental results currently available, we have referred to Sfer et al. (2002, their Fig. 6) and to the Newman and Newman (1971) empirical relationship

$$\frac{\sigma_1}{f_c} = 1 + 3.7 \left(\frac{\sigma_3}{f_c}\right)^{0.86},\tag{2.23}$$

where σ_1 and σ_3 are the maximum and minimum principal stresses at failure
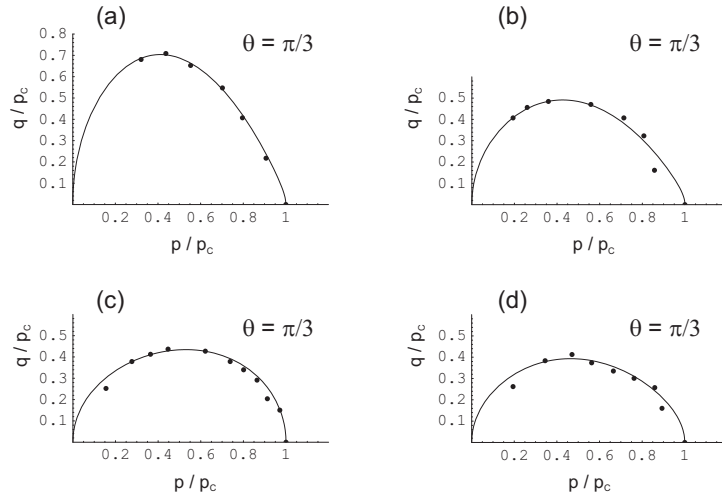
Figure 2.6: Comparison with experimental results relative to aluminium powder (a) aluminum composite powder (b), lead powder (c) and lead shot-steel composite powder(d), data taken from Sridhar and Fleck (2000).

and f_c is the value of the ultimate uniaxial compressive strength. Small circles in Fig. 2.7 represents results obtained using relationship (2.23) in figure (a) and experimental results by Sfer et al. (2002) in figure (b); the approximation provided by the criterion (2.7)–(2.9) is also reported as a continuous line.
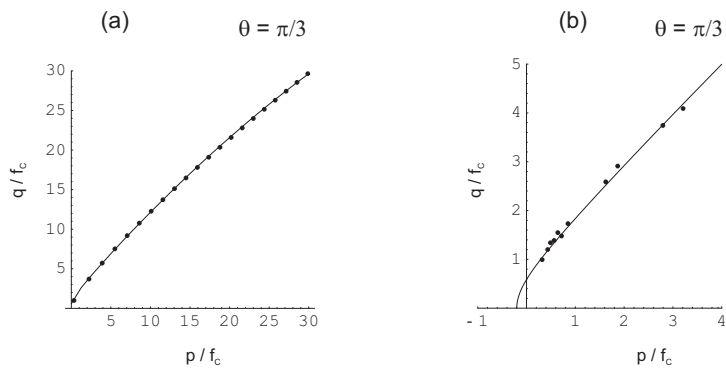
Figure 2.7: Comparison with the experimental relation (2.23) proposed by Newman and Newman (1971) (a) and with results by Sfer et al. (2002) (b).

As far as rocks are concerned, we limit to a few examples. However, we believe that due to the fact that our criterion approaches Coulomb-Mohr, it should be particularly suited for these materials. In particular, data taken from Hoek and Brown (1980, their pages 143 and 144) are reported in Fig. 2.8 as small circles for two rocks, chert (Fig. 2.8 a) and dolomite (Fig. 2.8 b).
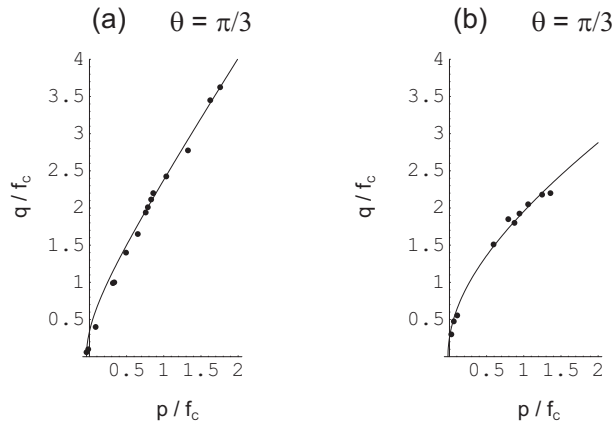
Figure 2.8: Comparison with experiments for rocks. Chert (a) and dolomite (b), data taken from Hoek and Brown (1980).

A few data on polymers are reported in Fig. 2.9 —together with the fitting provided by our model— concerning polymethil methacrylate (Fig. 2.9 a) and an epoxy binder (Fig. 2.9 b), taken from Ol'khovik (1983, their Fig. 5), see also Altenbach and Tushtev (2001, their Figs. 2 and 3).
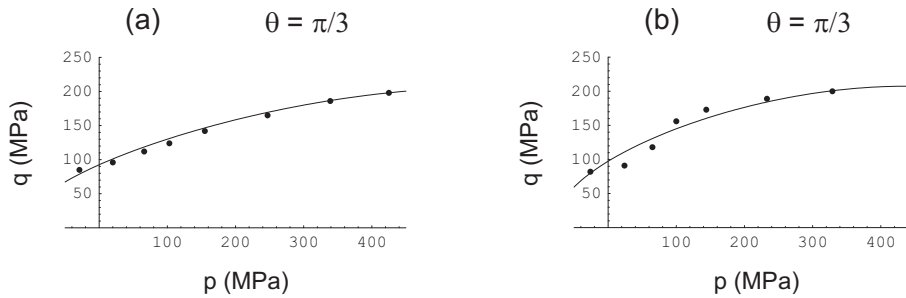
Figure 2.9: Comparison with experimental results for polymers. Methacrylate (a) and an epoxy binder (b), data taken from Ol'khovik (1983).

Finally, our model describes —with a different yield function— the same yield surface proposed by Deshpande and Fleck (2000) to describe the behaviour of metallic foams. In particular, the correspondence between parameters of our model (2.6)–(2.9) and of the yield surface proposed by Deshpande and Fleck [2000, their eqns. (2)–(3)] is obtained setting

$$\beta = 1, \quad \gamma = 0, \quad m = 2, \quad \alpha = 1,$$

and assuming the correlations given in Tab. 2.3.

Table 2.3: Correspondence between parameters of (2.6)–(2.9) and Deshpande and Fleck (2002) yield functions —the latter shortened as 'DF model'— to describe the behaviour of metallic foams.

	Model (2.6)–(2.9)			DF model	
	M	c	p_c	Y	α
DF model Y, α	2α	$\dfrac{Y}{\alpha}\sqrt{1+\left(\dfrac{\alpha}{3}\right)^2}$	$\dfrac{Y}{\alpha}\sqrt{1+\left(\dfrac{\alpha}{3}\right)^2}$	—	—
Model (2.6)–(2.9) M, p_c, c	—	—	—	$\dfrac{cM}{2\sqrt{1+\left(\frac{M}{6}\right)^2}}$	$\dfrac{M}{2}$

The proposed function (2.6)–(2.9) is also expected to model correctly yielding of porous ductile metals. As a demonstration of this, we present in Fig. 2.10 a comparison with the Gurson (1977) model. The Gurson yield function has a circular deviatoric section so that $\beta = 1$ and $\gamma = 0$ in our model, in addition, we select

$$\alpha = 1, \quad m = 2,$$

$$p_c = c = \sigma_M \frac{2}{3q_2} \cosh^{-1} \frac{1 + q_3 f^2}{2fq_1}, \tag{2.24}$$

$$M = \sigma_M \frac{2}{p_c} \sqrt{1 + q_3 f^2 - 2fq_1},$$
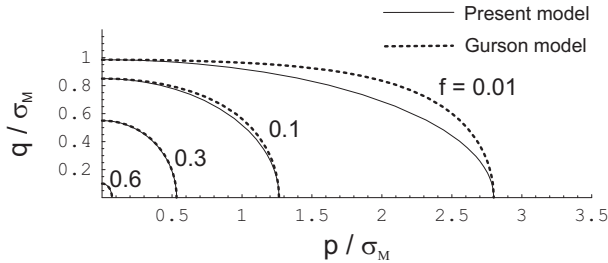
Figure 2.10: Comparison with the Gurson model at different values of void volume fraction f.

where f is the void volume fraction (taking the values {0.01, 0.1, 0.3, 0.6 } in Fig. 2.10), σ_M is the equivalent flow stress in the matrix material and $q_1 = 1.5$, $q_2 = 1$ and $q_3 = q_1^2$ are the parameters introduced by Tvergaard (1981, 1982). A good agreement between the two models can be appreciated from Fig. 2.10, increasing when the void volume fraction f increases.

As far as the deviatoric section is regarded, we limit to two examples —reported in Fig. 2.11— concerning sandstone and dense sand, where the experimental data have been taken from Lade (1997, their Figs. 2 and 9a).
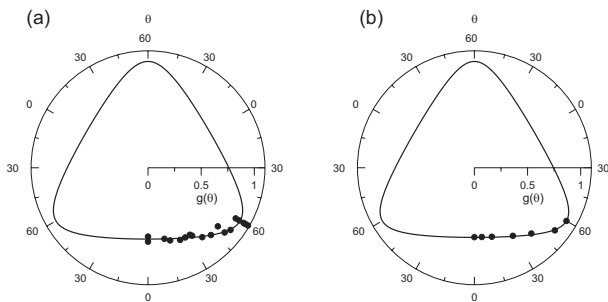
Figure 2.11: Comparison with experimental results relative to deviatoric section for sandstone (a) and dense sand (b) data taken from (Lade, 1997).

Experimental data referred to the biaxial plane $\sigma_3 = 0$ for grey cast iron and concrete (taken respectively from Coffin and Schenectady, 1950, their Fig. 5 and Tasuji et al. 1978, their Figs. 1 and 2) are reported in Fig. 2.12.
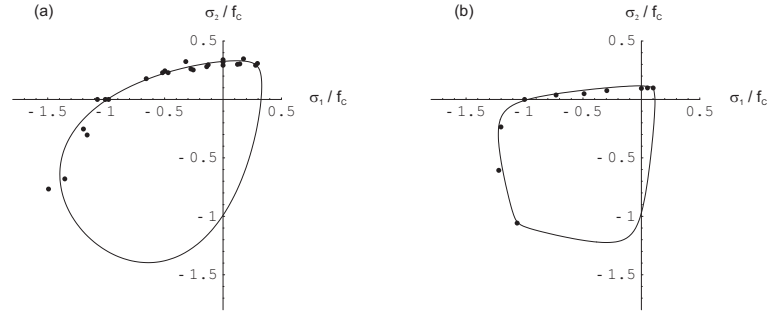
Figure 2.12: Comparison with experimental results on biaxial plane for cast iron (data taken from Coffin and Schenectady, 1950) (a) and concrete (data taken from Tasuji et al. 1978) (b).

2.4   On convexity of yield function and yield surface

Convexity of the yield function (2.6)–(2.9) within the range of parameters (2.10)–(2.11) was simply stated in the previous Section and still needs a proof. This will be given at the end of the present Section as an application of a general proposition relating convexity of yield functions and surfaces that is given below.

    We begin noting that while convexity of the yield function implies convexity of the corresponding yield surface, the converse is usually false, namely, convexity of a level set of a function is unrelated to convexity of the function itself. As an example, let us consider the non-convex yield function

$$f(p,q) = \frac{p^4}{a^4} - \frac{p^2}{a^2} + \frac{q^2}{b^2}, \quad 0 \le \frac{p}{a} \le 1, \tag{2.25}$$

(where a and b are material parameters having the dimension of stress) which corresponds to a convex yield surface $f(p,q) = 0$, Fig. 2.13. After the pioneering work of de Finetti (1949), it became clear that convexity of *every* level set of a function represents its *quasi-convexity*, a property defining a class of functions much broader than the class of convex functions. In more detail, let us consider a function $f(\boldsymbol{x}) : U \longrightarrow \mathbf{R}$, with U being a convex set, and its level sets

$$L_\alpha = \{\boldsymbol{x} \in U \mid f(\boldsymbol{x}) \le \alpha\}, \tag{2.26}$$

so that:

    f is quasi-convex if the level sets L_α are convex for every $\alpha \in \mathbf{R}$.
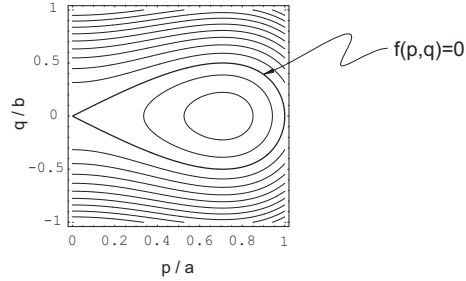
Figure 2.13: Level sets of function (2.25).

Now, the above definition of quasi-convexity is equivalent (Roberts and Varberg, 1973) to the definition

$$f[\lambda \boldsymbol{x} + (1 + \lambda)\boldsymbol{y}] \leq \max \{f(\boldsymbol{x}), f(\boldsymbol{y})\}, \quad \forall \boldsymbol{x}, \boldsymbol{y} \in U, \quad \forall \lambda \in [0, 1], \qquad (2.27)$$

and, if f is continuous and differentiable, to

$$f(\boldsymbol{y}) \leq f(\boldsymbol{x}) \quad \Rightarrow \quad \nabla f(\boldsymbol{x}) \cdot (\boldsymbol{x} - \boldsymbol{y}) \geq 0, \quad \forall \boldsymbol{x}, \boldsymbol{y} \in U. \qquad (2.28)$$

Convexity of the yield *surface* can be either accepted on the basis of experimental results, or on some engineering argumentation, such as for instance Drucker's postulate. Obviously, a convex yield locus can be expressed as a level set of a function, that generally may lack convexity and, even, quasi-convexity. For example, the level sets of function (2.25) are given in Fig. 2.13.

It can be observed that while $f(p, q) = 0$ may perfectly serve as a (convex) yield surface, the corresponding yield function even lacks quasi-convexity.[7] It is true that, in principle, a convex yield function can always be found to represent a convex yield surface, but to find this in a reasonably simple form may be an hard task. In other words, a number of yield functions that were formulated as an interpolation of experimental results still need a proof of convexity, even in cases where the corresponding yield locus is convex. The propositions that will be given below set some basis to provide these proofs.

---

[7]As noted by Franchi et al. (1990), definition (2.28) is very similar to Drucker's postulate. However, Drucker's postulate merely prescribes the so-called normality rule of plastic flow and convexity of yield surface (Drucker, 1956, 1964). Quasi-convexity becomes a consequence of Drucker's postulate only in the special case —considered by Franchi et al. (1990)— in which convexity of yield surface implies convexity of all level sets of the corresponding function.

2.4.1   A general result for a class of yield functions

The yield function (2.6)–(2.9) presented in the previous section may be viewed as an element of a family of models specified by the generic form (2.6). This family includes, among others, the models by Gudheus (1973), Argyris et al. (1974), Willam and Warnke (1975), Eekelen (1980), Lin and Bazant (1986), Bardet (1990), Ehlers (1995), and Menétrey and Willam (1995) and Christensen (1997) and Christensen et al. (2002).

A general result is provided below showing that for the range of material parameters for which the Haigh-Westergaard representation of a yield surface (2.13) is convex, the function is also convex.

Proposition 1: Convexity of the yield *function* (2.6) is equivalent to convexity of the meridian and deviatoric sections of the corresponding yield *surface* (2.13) in the Haigh-Westergaard representation. In symbols:

$$\text{convexity of } F(\boldsymbol{\sigma}) = f(p) + \frac{q}{g(\theta)} \iff f'' \geq 0, \quad \& \quad g^2 + 2g'^{\,2} - gg'' \geq 0, \quad (2.29)$$

where $g(\theta)$ is a positive function.

Proof. It is a well-known theorem of convex analysis (Ekeland and Temam, 1976) that the sum of two convex functions is also a convex function. Since q, p and θ are independent parameters, failure of convexity of $f(p)$ or $q/g(\theta)$ implies failure of convexity of $F(\boldsymbol{\sigma})$ and therefore convexity of both $f(p)$ and $q/g(\theta)$ are necessary and sufficient conditions for convexity of $F(\boldsymbol{\sigma})$.

Now, let us first analyze $f(p)$. The fact that convexity of $f(p)$ as a function of $\boldsymbol{\sigma}$ is equivalent to convexity of the meridian section follows from linearity of the trace operator, in view of the fact that $p = -\text{tr}\boldsymbol{\sigma}/3$.

Second, the fact that convexity of $q/g(\theta)$ as function of $\boldsymbol{\sigma}$ is equivalent to the convexity of the deviatoric section follows from the 3 lemmas listed below. $\square$

Lemma 1 (Hill, 1968): Convexity of an isotropic function of a symmetric (stress) tensor $\boldsymbol{\sigma}$ is equivalent to convexity of the corresponding function of the principal (stress) values σ_i $(i = 1, 2, 3)$. In symbols, given:

$$\phi(\boldsymbol{\sigma}) = \tilde{\phi}(\sigma_1, \sigma_2, \sigma_3), \qquad (2.30)$$

then:

$$\Delta \frac{\partial \phi}{\partial \boldsymbol{\sigma}} \cdot \Delta \boldsymbol{\sigma} \geq 0 \iff \sum_{i=1}^{3} \Delta \frac{\partial \tilde{\phi}}{\partial \sigma_i} \Delta \sigma_i \geq 0, \qquad (2.31)$$

where Δ denotes an ordered difference in the variables, so that, denoting with A and B two points in the tensor space

$$\Delta \frac{\partial \phi}{\partial \boldsymbol{\sigma}} \cdot \Delta \boldsymbol{\sigma} = \left(\frac{\partial \phi}{\partial \boldsymbol{\sigma}}\bigg|_{\boldsymbol{\sigma}^A} - \frac{\partial \phi}{\partial \boldsymbol{\sigma}}\bigg|_{\boldsymbol{\sigma}^B} \right) \cdot (\boldsymbol{\sigma}^A - \boldsymbol{\sigma}^B), \qquad (2.32)$$

$$\Delta \frac{\partial \tilde{\phi}}{\partial \sigma_i} \Delta \sigma_i = \left(\frac{\partial \tilde{\phi}}{\partial \sigma_i}\bigg|_{\{\sigma_1^A, \sigma_2^A, \sigma_3^A\}} - \frac{\partial \tilde{\phi}}{\partial \sigma_i}\bigg|_{\{\sigma_1^B, \sigma_2^B, \sigma_3^B\}} \right) (\sigma_i^A - \sigma_i^B). \qquad (2.33)$$

Proof. That convexity of ϕ implies convexity of $\tilde{\phi}$ is self-evident. The converse is not trivial and a proof was given by Hill (1968) with reference to an elastic strain energy function. The proof, omitted here for brevity, was later obtained also by Yang (1980) with explicit reference to a yield function. $\square$

Lemma 2: Given a generic isotropic function ϕ of the stress that can be expressed as

$$\phi(\sigma_1, \sigma_2, \sigma_3) = \tilde{\phi}(S_1, S_2), \qquad (2.34)$$

where S_1 and S_2 are two of the principal components of deviatoric stress, i.e.

$$S_1 = \frac{1}{3}(2\sigma_1 - \sigma_2 - \sigma_3), \quad S_2 = \frac{1}{3}(-\sigma_1 + 2\sigma_2 - \sigma_3), \qquad (2.35)$$

convexity of $\phi(\sigma_1, \sigma_2, \sigma_3)$ is equivalent to convexity of $\tilde{\phi}(S_1, S_2)$.

Proof. The proof follows immediately from the observation that the relation (2.35) between $\{S_1, S_2\}$ and $\{\sigma_1, \sigma_2, \sigma_3\}$ is linear. $\square$

Lemma 3: Convexity of

$$\frac{q}{g(\theta)} \qquad (2.36)$$

as a function of S_1, S_2 is equivalent to the convexity of the deviatoric section in the Haigh-Westergaard space:

$$g^2 + 2g'^2 - gg'' \geq 0. \qquad (2.37)$$

Proof. The Hessian of (2.36) is

$$
\frac{\partial^2 q/g(\theta)}{\partial S_i \partial S_j} = \frac{1}{g^3} \left[g^2 \frac{\partial^2 q}{\partial S_i \partial S_j} + q(2g'^{\,2} - gg'') \frac{\partial \theta}{\partial S_i} \frac{\partial \theta}{\partial S_j} \right.
$$
$$
\left. - gg' \left(\frac{\partial q}{\partial S_i} \frac{\partial \theta}{\partial S_j} + \frac{\partial q}{\partial S_j} \frac{\partial \theta}{\partial S_i} + q \frac{\partial^2 \theta}{\partial S_i \partial S_j} \right) \right],
\tag{2.38}
$$

where i and j range between 1 and 2 and all functions q and θ are to be understood as functions of S_1 and S_2 only. Derivatives of q may be easily calculated to be

$$
\frac{\partial q}{\partial S_i} = 2S_i - (-1)^i m_i, \quad \frac{\partial^2 q}{\partial S_i \partial S_j} = \frac{27}{4q^3} m_i m_j,
\tag{2.39}
$$

where indices are not summed and vector $\boldsymbol{m}$ has the components

$$
\{\boldsymbol{m}\} = \{S_2, -S_1\}.
\tag{2.40}
$$

The derivatives of θ can be performed through $\cos 3\theta$, eqn. $(2.3)_1$, noting that

$$
\frac{\partial \theta}{\partial S_i} = \frac{-1}{3 \sin 3\theta} \frac{\partial \cos 3\theta}{\partial S_i},
$$
$$
\frac{\partial^2 \theta}{\partial S_i \partial S_j} = \frac{-1}{3 \sin 3\theta} \left(\frac{\cos 3\theta}{\sin^2 3\theta} \frac{\partial \cos 3\theta}{\partial S_i} \frac{\partial \cos 3\theta}{\partial S_j} + \frac{\partial^2 \cos 3\theta}{\partial S_i \partial S_j} \right),
\tag{2.41}
$$

so that

$$
\frac{\partial q}{\partial S_i} \frac{\partial \theta}{\partial S_j} + \frac{\partial q}{\partial S_j} \frac{\partial \theta}{\partial S_i} + q \frac{\partial^2 \theta}{\partial S_i \partial S_j} =
$$
$$
\frac{-1}{\sin 3\theta} \left[\frac{\partial^2 q \cos 3\theta}{\partial S_i \partial S_j} - \cos 3\theta \frac{\partial^2 q}{\partial S_i \partial S_j} + q \frac{\cos 3\theta}{\sin^2 3\theta} \frac{\partial \cos 3\theta}{\partial S_i} \frac{\partial \cos 3\theta}{\partial S_j} \right],
\tag{2.42}
$$

where

$$
\frac{\partial \cos 3\theta}{\partial S_i} = \frac{9\sqrt{3} \sin 3\theta}{2q^2} m_i, \quad \frac{\partial^2 q \cos 3\theta}{\partial S_i \partial S_j} = -27^2 \frac{J_3}{q^6} m_i m_j.
\tag{2.43}
$$

A substitution of (2.43) into (2.42) yields

$$
\frac{\partial q}{\partial S_i} \frac{\partial \theta}{\partial S_j} + \frac{\partial q}{\partial S_j} \frac{\partial \theta}{\partial S_i} + q \frac{\partial^2 \theta}{\partial S_i \partial S_j} = 0,
\tag{2.44}
$$

so that we may conclude that the Hessian (2.38) can be written as

$$\frac{\partial^2 q/g(\theta)}{\partial S_i \partial S_j} = \frac{27}{4} \frac{\left(g^2 + 2g'^2 - gg''\right)}{q^3 g^3} m_i m_j.$$ (2.45)

Positive semi-definiteness of the Hessian (2.45) is condition (2.37), which, in turn, represents non-negativeness of the curvature (and thus convexity) of deviatoric section. $\square$

2.4.2 Applications of Proposition 1

The scope of this section is on one hand to prove the convexity of function (2.6)–(2.9) within the range (2.10)–(2.11) of material parameters, on the other hand to show that Proposition 1 is constructive, in the sense that can be used to invent convex yield functions. Let us begin with the first issue.

The proposed yield function (2.6)–(2.9)

First, we show that $f(p)$, eqn. (2.6), is a convex function of p (so that the meridian section is convex) and, second, that the deviatioric section described by $g(\theta)$, eqn. (2.9), is convex for the range of material parameters listed in (2.10)–(2.11). Therefore, as a conclusion from Proposition 1, function $F(\boldsymbol{\sigma})$ results to be convex.

A well-known result of convex analysis (Ekeland and Temam, 1976) states that function $f(p)$ is convex if and only if the restriction to its effective domain (i.e. $\Phi \in [0,1]$) is convex. Moreover, the function Φ appearing in (2.8) is a linear function of p so that convexity of $f(p)$ can be inferred from convexity of the corresponding function, say $\tilde{f}$, of Φ. Introducing for simplicity the function

$$h(\Phi) = (\Phi - \Phi^m)\left[2(1-\alpha)\Phi + \alpha\right],$$ (2.46)

the convexity of function $\tilde{f}(\Phi)$ reduces to the condition

$$\left[h'(\Phi)\right]^2 - 2h''(\Phi)h(\Phi) \geq 0,$$ (2.47)

where

$$h'(\Phi) = \left(1 - m\Phi^{m-1}\right)\left[2(1-\alpha)\Phi + \alpha\right] + 2(1-\alpha)\left(\Phi - \Phi^m\right),$$

$$h''(\Phi) =$$ (2.48)
$$- m(m-1)\Phi^{m-2}\left[2(1-\alpha)\Phi + \alpha\right] + 4(1-\alpha)\left(1 - m\Phi^{m-1}\right).$$

Fulfillment of eqn (2.47) can be now easily proven considering the inequality

$$h''(\Phi) \leq 4(1 - \alpha)\left(1 - m\Phi^{m-1}\right), \quad \forall \ \Phi \in [0, 1]. \tag{2.49}$$

It remains now to show convexity of $q/g(\theta)$. To this purpose, Proposition 1 can be employed, through substitution of (2.9) into the convexity condition eqn. (2.37), thus yielding

$$\frac{1}{g(\theta)} + \frac{3\gamma \cos 3\theta}{\sqrt{1 - \gamma^2 \cos^2 3\theta}} \sin\left[\beta\frac{\pi}{6} - \frac{1}{3}\cos^{-1}(\gamma \cos 3\theta)\right] \geq 0, \tag{2.50}$$

where $\theta \in [0, \pi/3]$ and $g(\theta)$ is given by eqn. (2.9). For values of γ belonging to the interval specified in $(2.10)_7$, condition (2.50) can be transformed into

$$\sin\left(\frac{\beta\pi}{6} - \frac{4}{3}x\right) + 2\sin\left(\frac{\beta\pi}{6} + \frac{2}{3}x\right) \geq 0, \tag{2.51}$$

with $x \in [\cos^{-1}\gamma, \ \pi - \cos^{-1}\gamma]$ and then into

$$\frac{-1 + 2\cos z + 2\cos^2 z}{2\sin z(1 - \cos z)} \sin\beta\frac{\pi}{6} + \cos\beta\frac{\pi}{6} \geq 0, \tag{2.52}$$

with $z \in [2/3\cos^{-1}\gamma, \ 2/3(\pi - \cos^{-1}\gamma)]$, an inequality that can be shown to be verified within the interval of β specified in (2.11) and thus also within its subinterval $(2.10)_6$.

Generating convex yield functions

Proposition 1 can be easily employed to build convex yield functions within the class described by eqn. (2.6). The simplest possibility is to maintain $f(p)$ in the form (2.7) and change the deviatoric function eqn. (2.9). As a first proposal, we can introduce the following function

$$g(\theta) = [1 + \beta(1 + \cos 3\theta)]^{-1/n}, \tag{2.53}$$

instead of (2.9). This describes a smooth deviatoric section approaching (without reaching) the triangular (Rankine) shape when parameters $n > 0$ and $\beta \geq 0$ are varied. The yield function is convex within the range of parameters reported in Tab. 2.4. The yield function defined by eqns. (2.7) and (2.53) does not possess the extreme deformability of (2.7) and (2.9) and does not admit Mohr-Coulomb and Tresca as limits, but results in a simple expression. The performance of the deviatoric shape of the yield surface is analyzed in

Table 2.4: Conditions for the convexity of deviatoric yield function (2.53).

$0 < n \leq 11/3$	$n \geq 11/3$
$\beta \leq \dfrac{n}{9 - 2n}$	$\beta \leq \left(-1 + \sqrt{1 + \dfrac{9(n-2)^2}{n^2(4n-13)}}\right)^{-1}$
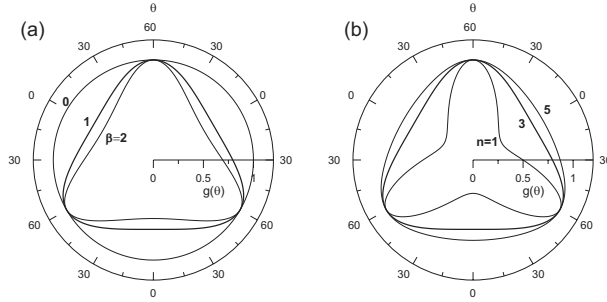
Figure 2.14: Deviatoric section (2.53): effects related to the variation of β (a) and n (b).

Fig. 2.14, where the solid lines correspond to the limit of convexity, $\beta = 1$ and $n = 3$. The curves reported in Fig. 2.14 (a) are relative to the values of $\beta = 0, 1, 2$, whereas for Fig. 2.14 (b) n takes the values $\{1, 3, 5\}$.

A limitation of the yield surface described by eqns. (2.7) and (2.53) is that the deviatoric section cannot be stretched until the Rankine limit. This can be easily emended assuming for $g(\theta)$ our expression (2.9) or that proposed by Willam and Warnke (1975) (see also Menétrey and Willam, 1995)

$$g(\theta) = \frac{2(1-e^2)\cos\theta + (2e-1)\left[4(1-e^2)\cos^2\theta + 5e^2 - 4e\right]^{0.5}}{4(1-e^2)\cos^2\theta + (2e-1)^2}, \quad (2.54)$$

where $e \in]0.5, 1]$ is a material parameter, yielding in the limit $e \longrightarrow 0.5$ the Rankine criterion and the von Mises criterion when $e = 1$.

It is already known that the deviatoric section of the yield surface corresponding to eqn. (2.54) remains convex for any value of the parameter e rang-

ing within the interval $]0.5, 1]$, so that —from Proposition 1— the function (2.6) equipped with the definition (2.54) of the function $g(\theta)$ is also convex.

As a final example, we can employ function $g(\theta)$ defined by the expression proposed by Gudheus (1973) and Argyris et al. (1974)

$$g(\theta) = \frac{2k}{1 + k + (1 - k) \cos 3\theta}, \qquad (2.55)$$

where $k \in]0.777, 1]$ is a material parameter.

Otherwise, we can act on the meridian function. For instance, we can modify a Drucker-Prager criterion —which again fits in the framework described by eqn. (2.6)— obtaining a non-circular deviatoric section described by eqn. (2.9)

$$F(\boldsymbol{\sigma}) = -\Gamma (p + c) + q \cos \left[\beta \frac{\pi}{6} - \frac{1}{3} \cos^{-1} (\gamma \cos 3\theta) \right], \qquad (2.56)$$

where c is the yield strength under isotropic tension and Γ is a material parameter, or by eqn. (2.53)

$$F(\boldsymbol{\sigma}) = -\Gamma (p + c) + q[1 + \beta(1 + \cos 3\theta)]^{1/n}, \qquad (2.57)$$

or by the Gudheus/Argyris condition (2.55)

$$F(\boldsymbol{\sigma}) = -\Gamma (p + c) + \frac{q}{2k} [1 + k + (1 - k) \cos 3\theta]. \qquad (2.58)$$

It may be noted that the yield criterion (2.58) has been employed by Laroussi et al. (2002) to describe the behaviour of foams. In all the above cases, Proposition 1 ensures that for the range of parameters in which the Haigh-Westergaard representation of the yield surface is convex, the yield function is also convex.

2.4.3   A note on the behaviour of concrete and a generalization of Proposition 1

In the modelling of concrete there is some experimental evidence that the deviatoric section starts close to the Rankine limit for low hydrostatic stress component and tends to approach a circle, when confinement increases. This effect has been described by Ottosen (1977) through a model which does not fit the general framework specified by eqn. (2.6) and can be written in our notation in the form

$$F(\boldsymbol{\sigma}) = Aq^2 + B\frac{q}{g(\theta)} + C - p, \qquad (2.59)$$

where $A > 0$, $B \geq 0$ and $C \leq 0$ are constants and $g(\theta)$ is in the form (2.9) with $\beta = 0$. The criterion is therefore defined by four parameters.

The above-expression (2.59) of the yield function suggests the following generalization of Proposition 1:

Proposition 2: Convexity of the yield function

$$F(\boldsymbol{\sigma}) = Aq^2 + B\frac{q}{g(\theta)} + f(p), \tag{2.60}$$

where A and B are positive constants, is equivalent to

$$f'' \geq 0, \quad \& \quad g^2 + 2g'^{\,2} - gg'' \geq 0, \tag{2.61}$$

which in turn is equivalent to the convexity of the surface

$$B\frac{q}{g(\theta)} + f(p) = 0, \tag{2.62}$$

in the Haigh-Westergaard stress space.

Proof. Let us begin assuming that (2.61) holds true. In this condition Proposition 1 ensures that $f(p)$ and $q/g(\theta)$ are convex functions of $\boldsymbol{\sigma}$, so that (2.60) results the sum of three convex functions and its convexity follows. Vice-versa, failure of convexity of $f(p)$ immediately implies failure of convexity of (2.60) since p is independent of θ and q. Finally, let us assume that condition $(2.61)_2$ is violated, for a certain value, say $\tilde{\theta}$, of θ. The Hessian of

$$Aq^2 + Bq/g(\theta), \tag{2.63}$$

as a function of two components of deviatoric stress S_1 and S_2, is given by eqn. (2.45) summed to a constant and positive definite matrix

$$3A \begin{bmatrix} 2 & 1 \\ 1 & 2 \end{bmatrix} + B\frac{27}{4}\frac{\left(g^2 + 2g'^{\,2} - gg''\right)}{q^3 g^3} \begin{bmatrix} S_2^2 & -S_1 S_2 \\ -S_1 S_2 & S_1^2 \end{bmatrix}. \tag{2.64}$$

Considering now the Haigh-Westergaard representation, it is easy to understand that we can keep $\theta = \tilde{\theta}$ fixed and change S_1 and consequently S_2 so that S_1/S_2 remains constant. In this situation, while g and its derivatives remain fixed, the quantity

$$\frac{S_1^2}{q^3}, \tag{2.65}$$

in matrix (2.64) tends to $+\infty$ when S_1 tends to zero. Therefore, violation of $(2.61)_2$ cannot be compensated by a constant term and function (2.60) is not convex. $\square$

Proposition 2 provides the conditions for convexity of the Ottosen criterion. Moreover, the same proposition allows us to generalize our yield function (2.6)–(2.9) adding a q^2 term as in the Ottosen criterion. This leads immediately to

$$F(\boldsymbol{\sigma}) = Aq^2 + Bq \cos\left[\beta\frac{\pi}{6} - \frac{1}{3}\cos^{-1}\left(\gamma\cos 3\theta\right)\right] + f(p), \qquad (2.66)$$

where $f(p)$ is given by eqn (2.7).

Chapter 3

Elastoplastic coupling in a small strain formulation

3.1 Introduction

A model capable of describing cold forming of ceramic powders is presented here. The main feature is that it describes gain in cohesion and related variations of yield surface shape and of elastic properties, the latter employing the concept of elastoplastic coupling.

The peculiar mechanism of variation in cohesion due to plastic deformation can be described making recourse to the concept of hardening. We remind that the compaction of a ceramic powder is a process essentially consisting of the following three phases: (I) granule sliding and rearrangement, (II) granule deformation, (III) granule densification. Let us assume that a yield function exists for a granular material, defining its elastic range, so that when the material is in the initial cohesionless state, the null stress state lies on the yield surface, Fig. 3.1. Now, if the material is subject to increasing hydrostatic
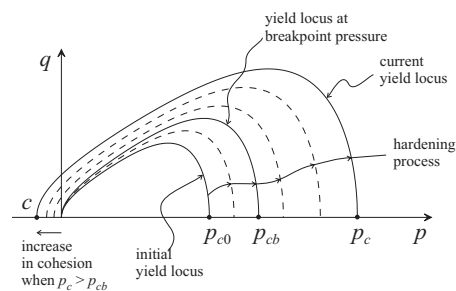
Figure 3.1: Increase in cohesion and hardening.

compression, after an initial (small) deformation in the elastic range, an early development of plastic deformation occurs from a virgin state, corresponding to Phase (I) compaction. In this phase, the increase in cohesion is limited and almost negligible. However, when the pressure reaches the breakpoint value, so that material enters Phase (II), the gain in cohesion becomes crucially important. In order to describe this process, we may employ a hardening law of the type sketched in Fig. 3.1, where the yield surface shape distortion changes qualitatively, when the applied pressure p exceeds the breakpoint pressure p_{cb}.[1]

At this point, one can get the impression that a model for the mechanism of increase in cohesion during densification of granular materials could be not particularly complicated and that this could be pursued just employing an appropriate hardening rule. The delicate point is however that *the elastic range of granular materials cannot be properly described by linear elasticity*, at least during Phase (I) of densification. It is a well-established concept in fact that the elastic law relating the volumetric deformation to the applied mean pressure is logarithmic, as sketched in Fig. 3.2. Since, for a cohesionless
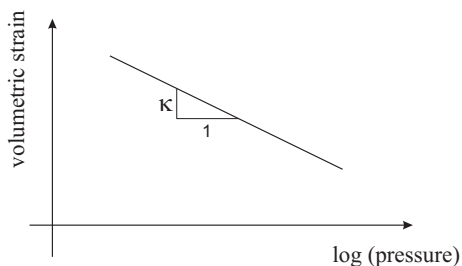
Figure 3.2: Logarithmic elastic law.

material the logarithmic law is simply not defined for null pressures, increasing the cohesion of the material implies a modification to the elastic law dependent on the plastic deformation, which is the driving mechanism for densification. This means that *the elastic properties of the material must depend on the plastic deformation*, a feature that can be described making recourse to the

---

[1]The type of increase in cohesion could also qualitatively change after the Phase (III) of densification is entered, but since we do not possess enough experimental data relative to this behaviour (occurring however at very high pressures, higher than those involved in the usual forming of ceramics), this is not accounted for in the modelling. We believe anyway that its consideration would be not difficult, once experimental results were made available.

concept of elastoplastic coupling (Hueckel, 1976; Dougill, 1976).

In the following, we will introduce the three fundamental ingredients in the modelling of the densification processes, namely, (i) the yield function appropriate for the description of the behaviour of granular materials, (ii) the nonlinear elastic model, coupled to plasticity, (iii) the hardening law.

3.2 The constitutive model

3.2.1 The yield function

The yield function was introduced in Chapter 2 and is thought to be suitable for describing a broad class of materials, particularly granular media. We recall here its expression, namely

$$F(\boldsymbol{\sigma}, p_c, c) = f(p, p_c, c) + \frac{q}{g(\theta)}, \qquad (3.1)$$

where p_c and c are the parameters governing hardening, q is the deviatoric invariant, $f(p)$ is the function describing the dependence on the mean pressure p, assumed in the form

$$f(p, p_c, c) = \begin{cases} -M p_c \sqrt{(\Phi - \Phi^m)\left[2(1-\alpha)\Phi + \alpha\right]} & \text{if } \Phi \in [0, 1], \\ +\infty & \text{if } \Phi \notin [0, 1], \end{cases} \qquad (3.2)$$

in which

$$\Phi = \frac{p + c}{p_c + c}, \qquad (3.3)$$

and $g(\theta)$ describes dependence on the Lode's invariant θ

$$g(\theta) = \frac{1}{\cos\left[\beta\dfrac{\pi}{6} - \dfrac{1}{3}\cos^{-1}\left(\gamma\cos 3\theta\right)\right]}. \qquad (3.4)$$

The yield function described by eqn. (3.1)-(3.4) has been motivated and explained in great detail in Chapter 2. We mention here that the yield surface corresponding to eqns. (3.1)-(3.4) is extremely versatile and remains convex for a broad variation of parameters M, p_c, c, m, α, β, γ.

3.2.2 Elastoplastic coupling

Dependence of elastic properties of a material on plastic deformation for describing degradation of elastic properties was suggested independently by Hueckel (1976) for soils and Dougill (1976) for concrete. The model was then developed by Hueckel and Maier (1977), Capurso (1979), Maier and Hueckel (1979), and Bigoni and Hueckel (1991). The idea of coupling is implicitely included in the general treatment by Hill and Rice (1973) (see also Hill, 1978), resumed and slightly generalized by Bigoni (2000). It is important to mention that we will develop the concept of elastoplastic coupling in the way suggested by Bigoni (2000), which —differently from the approach pursued by Hueckel and Dougill— yields a symmetric constitutive operator in the specific case of associative flow rule. This fact follows from different constitutive assumptions, in particular, it will be assumed here as in (Bigoni, 2000; Gajo et al., 2004) that the flow rule sets the so-called 'irreversible' strain rate, which in the case of coupling is different from the plastic strain rate.

The necessity of elastoplastic coupling to model the densification process of granular materials considered here may be motivated —as sketched in Fig. 3.3— by the observation that elastic unloading in a uniaxial deformation test shows a tendency toward a stiffening caused by the increase in cohesion. However, even if this effect would be disregarded in a first approxia-
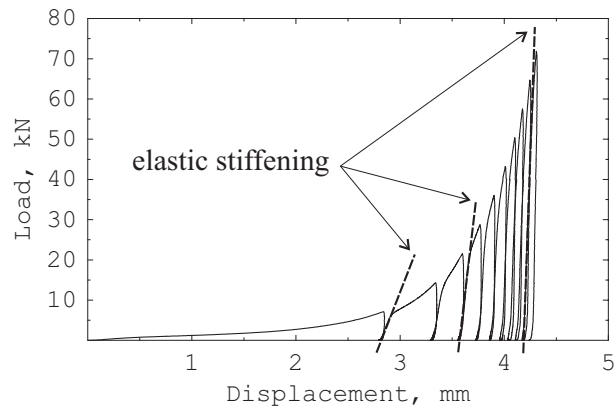
Figure 3.3: Elastic stiffening during uniaxial deformation test (experimental results on alumina powder).

tion, elastoplastic coupling would always be needed, for the reason mentioned

at the beginning of this Chapter, namely, to match the increase in cohesion with the nonlinear elastic model usually accepted for granular materials.

The basic concept of the elastoplastic coupling is that the elastic potential ϕ depends, in addition to the elastic, also on the plastic strain, so that

$$\boldsymbol{\sigma} = \frac{\partial \phi \left(\boldsymbol{\epsilon}^e, \boldsymbol{\epsilon}^p \right)}{\partial \boldsymbol{\epsilon}^e}, \tag{3.5}$$

where $\boldsymbol{\epsilon}^e$ and $\boldsymbol{\epsilon}^p$ are the elastic and plastic components of deformation, respectively.

In the elastic range, granular cohesionless material obey the well-known logarithmic law, relating the increment in the void ratio $\Delta e = e - e_0$ (measured with respect to an initial value e_0) to the current mean pressure $p = -\mathrm{tr}\boldsymbol{\sigma}/3$

$$\Delta e^e = -\kappa \log \frac{p}{p_0}, \tag{3.6}$$

where the suffix e remaks that we are referring to the elastic range, p_0 is the value of p corresponding to the initial void ratio e_0, and κ is the logarithmic bulk modulus. Eqn. (3.6) is the starting point to obtain the nonlinear elastic potential employed in the Cam-clay model (Roscoe and Schofield, 1963; Roscoe and Burland, 1968), which is particularly suitable for the description of cohesionless granular media. However, our intention here is to describe the behaviour of materials which may increase (or decrease) cohesion as a function of the plastic deformation. Therefore, we have to introduce a modification in the elastic Cam-clay potential, first, to include a cohesion and, second, to make this dependent on plastic deformation. The easiest way to do this is to introduce a plastic-dependent cohesion in eqn. (3.6), playing the role of a modification to the mean pressure

$$\Delta e^e = -\kappa \log \frac{p + c \left(\boldsymbol{\epsilon}^p \right)}{p_0 + c \left(\boldsymbol{\epsilon}^p \right)}, \tag{3.7}$$

where $c \left(\boldsymbol{\epsilon}^p \right)$ is the (positive) parameter describing the cohesion and depending on plastic deformation. In particular, the cohesion is assumed to depend on the *volumetric* component only of plastic deformation. This may be motivated by micromechanical considerations following, for instance, the Rowe (1962) model of a granular material, in which a shear deformation yields a loss (gain) in cohesion when accompanied by dilatancy (contractivity), Fig. 3.4.

We are in a position now to proceed with eqn. (3.7) in the standard way as usually done in the case of eqn. (3.6). Assuming incompressibility
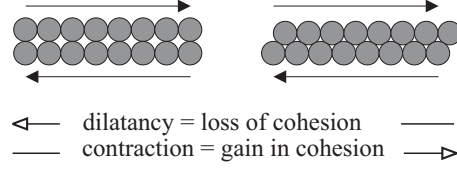
Figure 3.4: The mechanism of gain and loss of cohesion visualized in terms of the Rowe model.

of grains, the volumetric elastic deformation is given by $(e - e_0)/(1 + e_0)$, so that eqn. (3.6) defines a volumetric nonlinear elastic law, to be added to a linear elastic deviatoric constitutive equation. The resulting elastic potential is therefore

$$\phi(\boldsymbol{\epsilon}^e, \boldsymbol{\epsilon}^p) = -\frac{\mu}{3}(\operatorname{tr}\boldsymbol{\epsilon}^e)^2 + c\operatorname{tr}\boldsymbol{\epsilon}^e + \tilde{\kappa}(p_0 + c)\exp\left(-\frac{\operatorname{tr}\boldsymbol{\epsilon}^e}{\tilde{\kappa}}\right) + \mu\,\boldsymbol{\epsilon}^e \cdot \boldsymbol{\epsilon}^e, \quad (3.8)$$

where μ is the elastic shear modulus and $\tilde{\kappa} = \kappa/(1 + e_0)$. This elastic potential is suitable to describe the behaviour of the material in the first stage of the compaction process, as long as the material is still granular and the void ratio is high, but becomes unrealistic for the second stage, in which the material gains cohesion and can be regarded as a porous solid. Moreover, as the porosity decreases, the volumetric elastic behaviour changes from the nonlinear logaritmic law (3.7) to the simpler linear one. In order to describe this transition in the material behaviour, we modifiy the elastic potential as follows

$$\phi(\boldsymbol{\epsilon}^e, \boldsymbol{\epsilon}^p) = -\frac{\mu}{3}(\operatorname{tr}\boldsymbol{\epsilon}^e)^2 + c\operatorname{tr}\boldsymbol{\epsilon}^e \qquad\qquad\qquad (3.9)$$
$$+ (p_0 + c)\left[\left(d - \frac{1}{d}\right)\frac{(\operatorname{tr}\boldsymbol{\epsilon}^e)^2}{2\tilde{\kappa}} + d^{1/n}\tilde{\kappa}\exp\left(-\frac{\operatorname{tr}\boldsymbol{\epsilon}^e}{d^{1/n}\tilde{\kappa}}\right)\right] + \mu\,\boldsymbol{\epsilon}^e \cdot \boldsymbol{\epsilon}^e,$$

where d is a parameter depending on the plastic volumetric strain and governing the transition and n is a material constant defining the decay of the exponential term. Moreover we make the elastic shear modulus μ dependent on the volumetric plastic strain. In conclusion, the nonlinear elastic stress/strain law may be obtained from eqn. (3.9) and results dependent on the plastic strain through c, d, and μ (the dependence is not made explicit for

conciseness)

$$\boldsymbol{\sigma} = \left\{ -\frac{2}{3}\mu \operatorname{tr} \boldsymbol{\epsilon}^e + c \right. \tag{3.10}$$

$$\left. + (p_0 + c) \left[\left(d - \frac{1}{d} \right) \frac{\operatorname{tr} \boldsymbol{\epsilon}^e}{\tilde{\kappa}} - \exp\left(-\frac{\operatorname{tr} \boldsymbol{\epsilon}^e}{d^{1/n}\tilde{\kappa}} \right) \right] \right\} \boldsymbol{I} + 2\mu \boldsymbol{\epsilon}^e.$$

Taking the time derivative of (3.10), we get the rate equations

$$\dot{\boldsymbol{\sigma}} = \mathbb{E}[\dot{\boldsymbol{\epsilon}}^e] + \dot{c} \left[1 + \left(d - \frac{1}{d} \right) \frac{\operatorname{tr} \boldsymbol{\epsilon}^e}{\tilde{\kappa}} - \exp\left(-\frac{\operatorname{tr} \boldsymbol{\epsilon}^e}{d^{1/n}\tilde{\kappa}} \right) \right] \boldsymbol{I}$$

$$+ \dot{d} \frac{p_0 + c}{\tilde{\kappa}} \operatorname{tr} \boldsymbol{\epsilon}^e \left[1 + \frac{1}{d^2} - \frac{1}{nd^{1+1/n}} \exp\left(-\frac{\operatorname{tr} \boldsymbol{\epsilon}^e}{d^{1/n}\tilde{\kappa}} \right) \right] \boldsymbol{I} \tag{3.11}$$

$$+ \dot{\mu} \left(-\frac{2}{3} \operatorname{tr} \boldsymbol{\epsilon}^e \boldsymbol{I} + 2\boldsymbol{\epsilon}^e \right),$$

where $\dot{c}$, $\dot{d}$, and $\dot{\mu}$ arise from elastoplastic coupling ($\dot{c} = \dot{d} = \dot{\mu} = 0$ in the usual uncoupled models) and the elastic fourth-order tensor $\mathbb{E}$, together with its inverse $\mathbb{E}^{-1}$ (restricted to the space of all symmetric tensors) is given by

$$\mathbb{E} = \left[-\frac{2}{3}\mu + K_t \right] \boldsymbol{I} \otimes \boldsymbol{I} + 2\mu \boldsymbol{I} \,\overline{\overline{\otimes}}\, \boldsymbol{I},$$

$$\mathbb{E}^{-1} = \frac{2\mu - 3K_t}{18\mu K_t} \boldsymbol{I} \otimes \boldsymbol{I} + \frac{1}{2\mu} \boldsymbol{I} \,\overline{\overline{\otimes}}\, \boldsymbol{I}, \tag{3.12}$$

in which the tangent bulk modulus K_t depends on the plastic deformation through c and d and on the elastic deformation in the way

$$K_t = \frac{p_0 + c}{\tilde{\kappa}} \left[d - \frac{1}{d} + d^{-1/n} \exp\left(-\frac{\operatorname{tr} \boldsymbol{\epsilon}^e}{d^{1/n}\tilde{\kappa}} \right) \right]. \tag{3.13}$$

In order to further develop eqn. (3.11), evolution laws for the coupling parameters c, d, and μ are needed, providing the functional dependences of c, d, and μ on the plastic deformation. Obviously, a recourse to experimental evidence is necessary. Concerning the parameter c, experimental results referred to isotropic compression tests (Reed, 1995) suggest that the cohesion depends on the difference between the forming pressure p_c and the breakpoint pressure p_{cb}, following the law

$$c = c_\infty \left[1 - \exp\left(-\Gamma < p_c - p_{cb} > \right) \right], \tag{3.14}$$

where the symbol $<>$ denotes the Macaulay brackets operator (defined for every scalar α as $< \alpha >= (\alpha + |\alpha|)/2$), c_∞ and Γ are two positive material parameters, the former defining the limit value of cohesion reached after substantial plastic deformation, the latter related to the 'velocity of growth' of cohesion. With regard to elastic moduli K_t and μ, experimental results referred to triaxial compression tests (Zeuch et al., 2001) suggest that, when the material gains cohesion, the dependences of the tangent bulk modulus and the shear modulus on the forming pressure p_c are linear. This may be accomplished taking d and μ in the forms

$$d = 1 + B < p_c - p_{cb} > \quad \text{and} \quad \mu = \mu_0 + c\left(d - \frac{1}{d}\right)\mu_1, \qquad (3.15)$$

respectively, where B, μ_0, and μ_1 are positive material constants, so that the asimptotic behaviours of K_t and μ as $p_c \to \infty$ are

$$K_t \sim \frac{p_0 + c_\infty}{\tilde{\kappa}} B p_c \quad \text{and} \quad \mu \sim c_\infty B \mu_1 p_c, \qquad (3.16)$$

respectively.

On the other hand, the parameter p_c is related to the plastic deformation. The general form of this relationship can be understood making recourse to a micromechanical model proposed by Cooper and Eaton (1962), which takes into account the fundamental fact that compaction can be divided into three phases. Based on statistical micromechanics considerations and validated on several experimental results on ceramic powders, Cooper and Eaton (1962) provide a double-exponential law describing the first two phases of densification in terms of the relation between the plastic increment of void ratio Δe^p and the pressure parameter p_c,

$$-\frac{\Delta e^p}{e_0} = a_1 \exp\left(-\frac{\Lambda_1}{p_c}\right) + a_2 \exp\left(-\frac{\Lambda_2}{p_c}\right), \qquad (3.17)$$

where a_1, a_2, Λ_1 and Λ_2 are material (positive) constants. In particular, coefficients $-e_0 a_1$ and $-e_0 a_2$ denote the increment of void ratio that would be achieved at infinite pressure by each of the two processes of densification, so that $0 < a_1 + a_2 \leq 1$. Coefficients Λ_1 and Λ_2, which have the dimension of a pressure, indicate the magnitude of the pressure at which the particular process of deformation has the maximum probability density.

It may be noted that we restrict the attention to the double-exponential law (3.17) for simplicity, but there are not difficulties in including a more

complicated relationship, that —as suggested by Cooper and Eaton— may include an arbitrary number of exponential and may therefore describe even the third phase of compaction behaviour.

Since, assuming the grains incompressible, the plastic volumetric deformation is related to the plastic void ratio increment according to the rule

$$\Delta e^p = (1 + e_0) \operatorname{tr} \boldsymbol{\epsilon}^p, \tag{3.18}$$

we get from eqn. (3.17)

$$\operatorname{tr} \boldsymbol{\epsilon}^p = -\tilde{a}_1 \exp\left(-\frac{\Lambda_1}{p_c}\right) - \tilde{a}_2 \exp\left(-\frac{\Lambda_2}{p_c}\right), \tag{3.19}$$

where $\tilde{a}_i = e_0 a_i/(1 + e_0)$, $i = 1, 2$. Eqn. (3.19) defines an implicit relation between the plastic deformation and p_c, so that we may conclude that, together with eqns. (3.14)-(3.15), defines the relations between the parameters c, d, and μ and the volumetric plastic deformation $\operatorname{tr}\boldsymbol{\epsilon}^p$. These relations become explicit when the increments are considered. In particular, the rate of eqn. (3.19),

$$\dot{p}_c = -\frac{p_c^2}{\tilde{a}_1 \Lambda_1 \exp\left(-\dfrac{\Lambda_1}{p_c}\right) + \tilde{a}_2 \Lambda_2 \exp\left(-\dfrac{\Lambda_2}{p_c}\right)} \operatorname{tr} \dot{\boldsymbol{\epsilon}}^p, \tag{3.20}$$

combined with the rates of eqn. (3.14)-(3.15), gives

$$\dot{c} = \xi_2 \operatorname{tr} \dot{\boldsymbol{\epsilon}}^p, \quad \dot{d} = \xi_3 \operatorname{tr} \dot{\boldsymbol{\epsilon}}^p, \quad \text{and} \quad \dot{\mu} = \xi_4 \operatorname{tr} \dot{\boldsymbol{\epsilon}}^p, \tag{3.21}$$

where

$$\xi_2 = -\frac{c_\infty \Gamma \, H(p_c - p_{cb}) \exp\left[-\Gamma(p_c - p_{cb})\right] p_c^2}{\tilde{a}_1 \Lambda_1 \exp\left(-\dfrac{\Lambda_1}{p_c}\right) + \tilde{a}_2 \Lambda_2 \exp\left(-\dfrac{\Lambda_2}{p_c}\right)},$$

$$\xi_3 = -\frac{B \, H(p_c - p_{cb}) \, p_c^2}{\tilde{a}_1 \Lambda_1 \exp\left(-\dfrac{\Lambda_1}{p_c}\right) + \tilde{a}_2 \Lambda_2 \exp\left(-\dfrac{\Lambda_2}{p_c}\right)}, \tag{3.22}$$

$$\xi_4 = \left(d - \frac{1}{d}\right) \mu_1 \xi_2 + c\left(1 + \frac{1}{d^2}\right) \mu_1 \xi_3,$$

in which H denotes the Heaviside step function (defined for every scalar α as $H(\alpha) = 1$, if $\alpha \geq 0$, $H(\alpha) = 0$ otherwise).

Using (3.21) into (3.11), we may write

$$\dot{\boldsymbol{\sigma}} = \mathbb{E}[\dot{\boldsymbol{\epsilon}}^e] + \mathbb{P}[\dot{\boldsymbol{\epsilon}}^p], \tag{3.23}$$

where the fourth-order tensor $\mathbb{P}$ defines the contribution of the elastoplastic coupling, in the sense that $\mathbb{P} = \mathbb{O}$ in the usual, uncoupled plasticity and is defined as

$$\mathbb{P} = \xi_5 \boldsymbol{I} \otimes \boldsymbol{I} + 2\xi_4 \boldsymbol{\epsilon}^e \otimes \boldsymbol{I}, \tag{3.24}$$

in which

$$\xi_5 = -\frac{2}{3}\xi_4 \operatorname{tr} \boldsymbol{\epsilon}^e + \xi_2 \left[1 + \left(d - \frac{1}{d} \right) \frac{\operatorname{tr} \boldsymbol{\epsilon}^e}{\tilde{\kappa}} - \exp\left(-\frac{\operatorname{tr} \boldsymbol{\epsilon}^e}{d^{1/n}\tilde{\kappa}} \right) \right] \tag{3.25}$$
$$+ \xi_3 \frac{p_0 + c}{\tilde{\kappa}} \operatorname{tr} \boldsymbol{\epsilon}^e \left[1 + \frac{1}{d^2} - \frac{1}{nd^{1+1/n}} \exp\left(-\frac{\operatorname{tr} \boldsymbol{\epsilon}^e}{d^{1/n}\tilde{\kappa}} \right) \right].$$

Introducing now the strain rate additive decomposition

$$\dot{\boldsymbol{\epsilon}} = \dot{\boldsymbol{\epsilon}}^e + \dot{\boldsymbol{\epsilon}}^p, \tag{3.26}$$

we may transform the rate equation (3.23) into the equivalent form

$$\dot{\boldsymbol{\sigma}} = \mathbb{E}[\dot{\boldsymbol{\epsilon}}] - \mathbb{E}[\dot{\boldsymbol{\epsilon}}^i], \tag{3.27}$$

where the deformation rate called 'irreversible' (in an infinitesimal stress cycle) has been introduced, defined as

$$\dot{\boldsymbol{\epsilon}}^i = \mathbb{G}[\dot{\boldsymbol{\epsilon}}^p], \tag{3.28}$$

in which

$$\mathbb{G} = \boldsymbol{I} \,\overline{\underline{\otimes}}\, \boldsymbol{I} - \mathbb{E}^{-1}\mathbb{P} = \boldsymbol{I} \,\overline{\underline{\otimes}}\, \boldsymbol{I} + \xi_6 \boldsymbol{I} \otimes \boldsymbol{I} + \xi_7 \boldsymbol{\epsilon}^e \otimes \boldsymbol{I}, \tag{3.29}$$

with the inverse

$$\mathbb{G}^{-1} = \boldsymbol{I} \,\overline{\underline{\otimes}}\, \boldsymbol{I} + \xi_8 \boldsymbol{I} \otimes \boldsymbol{I} + \xi_9 \boldsymbol{\epsilon}^e \otimes \boldsymbol{I}, \tag{3.30}$$

where

$$\xi_6 = -\frac{\xi_5}{3K_t} - \frac{2\mu - 3K_t}{9\mu K_t} \xi_4 \operatorname{tr} \boldsymbol{\epsilon}^e, \quad \xi_7 = -\frac{\xi_4}{\mu}, \tag{3.31}$$

and

$$\xi_8 = -\frac{\xi_6}{1 + 3\xi_6 + \xi_7 \operatorname{tr} \boldsymbol{\epsilon}^e}, \quad \xi_9 = -\frac{\xi_7}{1 + 3\xi_6 + \xi_7 \operatorname{tr} \boldsymbol{\epsilon}^e}. \tag{3.32}$$

It should be noted that tensor $\mathbb{G}$ is assumed positive definite, which implies that

$$\dot{\boldsymbol{\epsilon}}^i \cdot \dot{\boldsymbol{\epsilon}}^p > 0, \tag{3.33}$$

a condition that we believe it is reasonable to assume (Mróz, 1963, 1966).

The irreversible deformation rate $\dot{\boldsymbol{\epsilon}}^i$ defined by eqn. (3.28) is the rate of deformation which is not recovered in an infinitesimal stress cycle. This should not be confused with the plastic deformation rate $\dot{\boldsymbol{\epsilon}}^p$ which can be only detected upon unloading at zero stress. This concept is illustrated in Fig. 3.5 with reference to a hypothetical volumetric stress/strain law, where the elastic rate deformation at unloading $\mathbb{E}^{-1}[\dot{\boldsymbol{\sigma}}]$ is also indicated. Due to the plastic

Figure 3.5: Irreversible, reversible, plastic, and elastic rate deformations, with reference to volumetric deformation.

increase in elastic stiffness, we note that (3.11) implies that the elastic rate at unloading is different for an increment involving plastic deformation.

A crucial point is now the definition of the flow rule, that following Hill and Rice (1973), Hill (1978) and Bigoni (2000) —and differently from Dougill (1976), Hueckel (1976), Hueckel and Maier (1977), Maier and Hueckel (1979), Capurso (1979)— is assumed to govern the irreversible strain rate, instead of the plastic:

$$\dot{\boldsymbol{\epsilon}}^i = \dot{\lambda}\boldsymbol{P}. \tag{3.34}$$

Experimental evidence for granular material referred to classical plasticity supports the adoption of a deviatoric associative flow rule. For simplicity, we adopt here also deviatoric associativity, so that tensor $\boldsymbol{P}$ is related to the yield function gradient $\boldsymbol{Q}$ through the rule

$$\boldsymbol{P} = \boldsymbol{Q} - \frac{\epsilon\,(1-\Phi)\,\mathrm{tr}\,\boldsymbol{Q}}{3}\,\boldsymbol{I}, \quad 0 \le \epsilon \le 1, \tag{3.35}$$

where ϵ is a parameter governing the entity of volumetric nonassociativity, so that $\epsilon = 0$ gives the associative flow rule.

The rate constitutive equations can now be obtained via Prager's consistency, so that $\dot{F} = 0$ during plastic deformation. Imposing this condition suggests the following definition of hardening modulus

$$h = -\frac{1}{\dot{\lambda}} \left(\frac{\partial F}{\partial p_c} \dot{p}_c + \frac{\partial F}{\partial c} \dot{c} \right),$$ (3.36)

which is positive in the case of hardening, negative for softening and null for ideally plastic behaviour. The derivatives of F with respect to the hardening parameters p_c and c appearing in eqn. (3.36) are given by

$$\frac{\partial F}{\partial p_c} = -M\sqrt{(\Phi - \Phi^m)\left[2(1-\alpha)\Phi + \alpha\right]}$$ (3.37)

$$+M\frac{p_c(p+c)}{(p_c+c)^2} \frac{\left(1 - m\Phi^{m-1}\right)\left[2(1-\alpha)\Phi + \alpha\right] + 2(1-\alpha)\left(\Phi - \Phi^m\right)}{2\sqrt{(\Phi - \Phi^m)\left[2(1-\alpha)\Phi + \alpha\right]}},$$

and

$$\frac{\partial F}{\partial c} = -M\frac{p_c(p_c - p)}{(p_c+c)^2} \cdot$$ (3.38)

$$\cdot \frac{\left(1 - m\Phi^{m-1}\right)\left[2(1-\alpha)\Phi + \alpha\right] + 2(1-\alpha)\left(\Phi - \Phi^m\right)}{2\sqrt{(\Phi - \Phi^m)\left[2(1-\alpha)\Phi + \alpha\right]}}.$$

Employing definition (3.36) into Prager's consistency yields the elastoplastic rate equations

$$\dot{\boldsymbol{\sigma}} = \begin{cases} \mathbb{E}[\dot{\boldsymbol{\epsilon}}] - \dfrac{1}{H} < \mathbf{Q} \cdot \mathbb{E}[\dot{\boldsymbol{\epsilon}}] > \mathbb{E}[\mathbf{P}] & \text{if } F(\boldsymbol{\sigma}, p_c, c) = 0, \\ \mathbb{E}[\dot{\boldsymbol{\epsilon}}] & \text{if } F(\boldsymbol{\sigma}, p_c, c) < 0, \end{cases}$$ (3.39)

where

$$H = h + \boldsymbol{Q} \cdot \mathbb{E}[\boldsymbol{P}].$$ (3.40)

It may be noted that the elastoplastic tangent operator becomes symmetric in the specific case of the associative flow rule, $\boldsymbol{P} = \boldsymbol{Q}$.

3.3 Calibration of parameters for densification of a ceramic powder

Calibration of the model has been performed on the basis of experiments carried out on alumina powder and available in the literature.

With regard to the yield surface, parameters m and α, which define the shape of the meridian section, have been calibrated according to experimental iso-density data in the (p, q) plane obtained from triaxial compression tests (Bonnefoy, 2001), assuming that iso-density curves correspond to yield surface sections (Kim et al., 2000; Kim et al., 2002). The values $m = 2$ and $\alpha = 0.1$ give the best fitting as shown in Fig. 3.6, where the data sets correspond to different levels of densification.
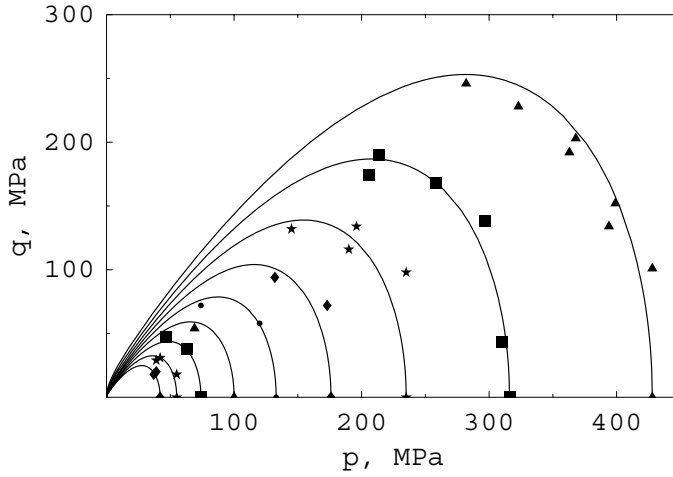
Figure 3.6: Meridian sections fitted to the iso-density data (Bonnefoy, 2001) for different levels of densification.

To our knowledge, in the literature there are no experimental data concerning the deviatoric section for alumina powder (and more in general for ceramic powders), which we could use to calibrate parameters β and γ and thus define the deviatoric function $g(\theta)$. Therefore these parameters have been calibrated on the basis of the angle of internal friction, $\phi = 32°$, obtained for alumina powder from direct shear tests (Piccolroaz et al., 2002; Piccolroaz et al., 2003).

Making recourse to the Coulomb-Mohr model, the ratio of the deviatoric section radius for triaxial extension, $g(0)$, to that for triaxial compression, $g(\pi/3)$, is related to the angle of internal friction through

$$\frac{g(0)}{g(\pi/3)} = \frac{3 - \sin\phi}{3 + \sin\phi}. \tag{3.41}$$

This is a single equation in two unknowns, β and γ, and is not enough to determine both of them. So we decided to fix $\gamma = 0.9$, which gives a deviatoric section fairly close to the piecewise linear deviatoric section, corresponding to $\gamma = 1$. This choice makes it easy to fit extremely distorted deviatoric sections even close to the convexity limits, as we showed in Chapter 2. Using this value of γ in eqn. (3.41) we get $\beta = 0.19$.

Parameter M, which defines the pressure-sensitivity, has been calibrated making recourse to the concept of critical state, a peculiar state in which the material deforms at constant stress and constant volume. From eqn. (3.20), the critical state occurs when $\mathrm{tr}\boldsymbol{\epsilon}^p = 0$, and therefore, from eqns. (3.28)-(3.30), when $\mathrm{tr}\boldsymbol{\epsilon}^i = 0$, which in turn is equivalent to $\mathrm{tr}\boldsymbol{Q} = 0$, as can be proved using eqns. (3.34) and (3.35). Finally the expression for the yield function gradient eqn. (2.14)-(2.16) provide the condition for the critical state in the form

$$2(m+1)(1-\alpha)\Phi^m + m\alpha\Phi^{m-1} - 4(1-\alpha)\Phi - \alpha = 0. \qquad (3.42)$$

This implicit relation can be solved numerically, as soon as values for m and α have been fixed, providing the value of Φ corresponding to the critical state,

$$\Phi^\star = \Phi^\star(m, \alpha),$$

in our case $\Phi^\star = 0.658$. The critical state point in the (p, q) plane is therefore

$$\begin{cases} p^\star = (p_c + c)\Phi^\star - c, \\[2ex] q^\star = g(\theta)Mp_c\sqrt{(\Phi^\star - \Phi^{\star m})\left[2(1-\alpha)\Phi^\star + \alpha\right]}, \end{cases} \qquad (3.43)$$

Eqns. (3.43) define the parametric representation of the critical state line in the (p, q) plane, with parameter p_c. Due to the fact that c is a nonlinear function of p_c, this line is not straight. Indeed the critical state line is straight in the first phase of densification, as long as $c = 0$, and then deflects from linearity in the subsequent phase when the material gains cohesion, approaching, after substantial plastic deformation and $c \sim c_\infty$, a straight line with the same slope as the initial line, namely

$$g(\theta)M\frac{\sqrt{(\Phi^\star - \Phi^{\star m})\left[2(1-\alpha)\Phi^\star + \alpha\right]}}{\Phi^\star}. \qquad (3.44)$$

However, since $c << p_c$ throughout the densification process, we can neglect the effect of c and take eqn. (3.44) as the slope of the critical state line for

the whole process. With reference to the triaxial compression state, $\theta = \pi/3$, this slope is related to the angle of internal friction through

$$\frac{6\sin\phi}{3 - \sin\phi},\tag{3.45}$$

which gives a value of M equal to 1.1.

The value of the logarithmic bulk modulus κ, which governs the elastic behaviour of the material in the first phase of densification, was deduced from the slope of curves obtained by loading and unloading the samples in uniaxial strain tests (Piccolroaz et al., 2002; Piccolroaz et al., 2003). For this evaluation, we have assumed a constant ratio between the horizontal σ_h and vertical σ_v stresses equal to 0.47, as deduced from the formulae

$$\frac{\sigma_h}{\sigma_v} = 1 - \sin\phi,\tag{3.46}$$

which is currently used for granular media (Jaky, 1944).

The hardening rule (3.19) is calibrated to describe uniaxial strain experiments (Piccolroaz et al., 2002; Piccolroaz et al., 2003). The values $\Lambda_1 = 1.8$ MPa, $\Lambda_2 = 40$ MPa, $\tilde{a}_1 = 0.37$, $\tilde{a}_2 = 0.12$ give the excellent interpolation presented in Fig. 3.7, where the volumetric plastic strain $\mathrm{tr}\epsilon^p$ is reported versus the hardening parameter p_c.
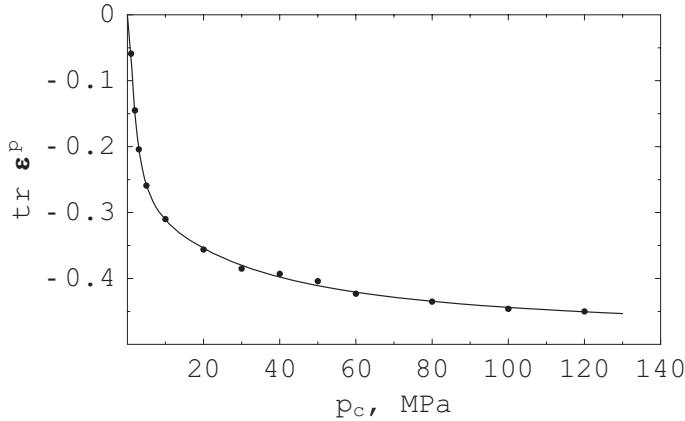
Figure 3.7: Fitting of parameter p_c.

The hardening law (3.14), representing the variation in cohesion c, as a function of the hardening parameter p_c is plotted in Fig. 3.8, together with the
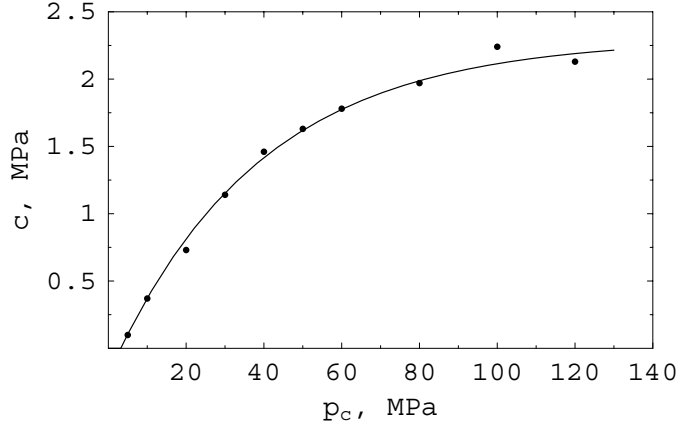
Figure 3.8: Fitting of parameter c.

experimental results. These refer to biaxial flexure strength tests on ceramic tablets produced through uniaxial strain (Piccolroaz et al., 2002; Piccolroaz et al., 2003). The material parameters $\Gamma = 0.026$ MPa^{-1}, $c_\infty = 2.3$ MPa, and $p_{cb} = 3.2$ MPa have been used, which provide a fair agreement.

3.4 Numerical simulations

The proposed constitutive model was implemented into the subroutine UMAT of the commercial finite element code ABAQUS (Hibbitt, Karlsson & Sorensen, 2001). The numerical integration scheme used was the so-called 'cutting-plane algorithm', proposed by Simo and Ortiz (1985), Ortiz and Simo (1986), Simo and Huges (1987). Numerical simulations were performed to simulate forming of the (axisymmetric) piece shown in Figs. 3.9 and 3.10.   Four pieces were formed at a final mean pressure of 100 MPa starting from 5 g of powder. The axisymmetric mesh used in the simulations is shown in Fig. 3.11. Axisymmetric 4-node elements (CAX4) have been used.

The following assumptions have been introduced:

- the die is undeformable;

- the contact between powder and die walls is smooth;

- the initial configuration is that shown in Fig. 3.11.

Figure 3.9: Photograph of the formed piece.
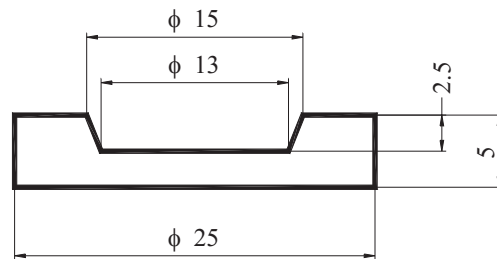
Figure 3.10: Geometry of the formed piece (dimensions in mm).

It may be worth noting that the above assumptions are not particularly strong in our specific analysis. In particular, we remark that, due to the large strains that will be reached during pressing, the assumption that the initial configuration shown in Fig. 3.11 is homogeneous does not affect much final results.

After the initial state – defined by initial values of void ratio and confining pressure – has been prescribed, the loading history is assigned, which is divided in the following three steps:

1. forming is prescribed by imposing the motion of the upper part of the boundary (3.78 mm, corresponding to the value measured during forming at the final load of 50 kN);
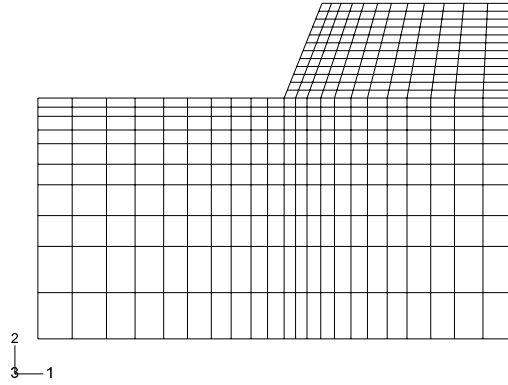
Figure 3.11: Initial mesh.
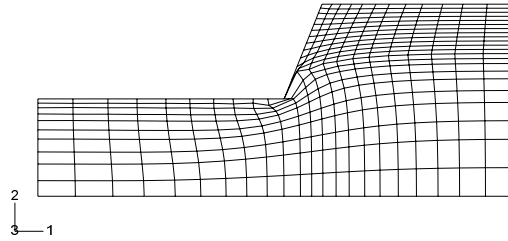
Figure 3.12: Deformed mesh at the end of step 1.
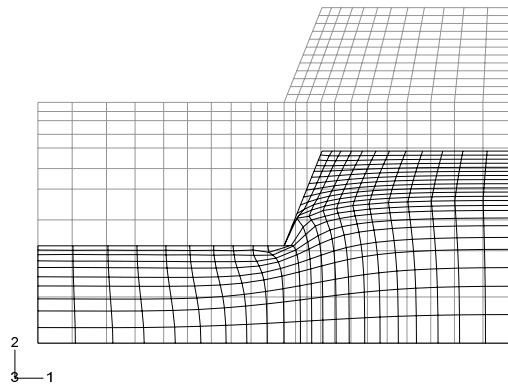
Figure 3.13: Initial and deformed (end of step 1) meshes.

2. unloading is simulated by prescribing null forces on the upper part of the boundary;

3. ejection is simulated by prescribing null forces on all the boundary.

The deformed mesh at the end of step 1 is shown in Fig. 3.12, whereas the same mesh superimposed on the initial mesh is shown in Fig. 3.13. It can be noted that the elements near the corner of the punch are unphysically distorted so that results in this zone should not be considered realistic. It is immediate to conclude from Figs. 3.12 and 3.13 that the deformation suffered by the piece is quite high.

The hydrostatic stress component p (taken positive when compressive), the Mises stress q and the void ratio e are reported in Figs. 3.14–3.16, respectively, at the end of step 1.

Excluding the small, unrepresentative zone near the corner of the punch, the hydrostatic stress p ranges from 42.3 MPa to 103 MPa and the Mises stress q from 25.1 MPa to 118 MPa. These values show that the stress is highly inhomogeneous.

Values of the hydrostatic and Mises stress components at the end of step 2 are reported in Figs. 3.17 and 3.18, whereas the map of void ratio is shown in Fig. 3.19.

It may be important to note that residual stress is quite high, due to the lateral constraint still present at the end of step 2. The knowledge of the lateral stress is important for practical purposes since the force needed for the ejection of the final piece can be estimated through Coulomb friction law, when the lateral stress at the end of step 2 is known. A rough, but simple evaluation can be immediately obtained from numerical output at the end of step 2 employing the formula

$$\textit{ejection force} = \alpha \tan \phi \, (\textit{mean lateral stress} \times \textit{lateral surface of the piece}),$$

where ϕ is the powder friction angle (equal to $32°$ in our case) and α is a coefficient dependent on the roughness of the die wall and ranging between 0 and 1, typically $\alpha = 0.6$.

The deformed mesh at the end of step 3 is shown in Figs. 3.20 and 3.21. In the latter figure, the deformed mesh is superimposed on the initial. It can be noted that the model correctly predicts that the springback effect and the shape distortion are very small. In particular, the final diameter of the piece is accurately estimated, 0.1 mm larger than the inner diameter of the die.
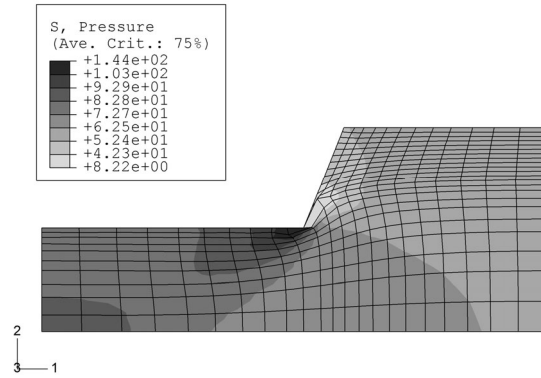
Figure 3.14: Distribution of hydrostatic stress p (MPa) at the end of step 1.
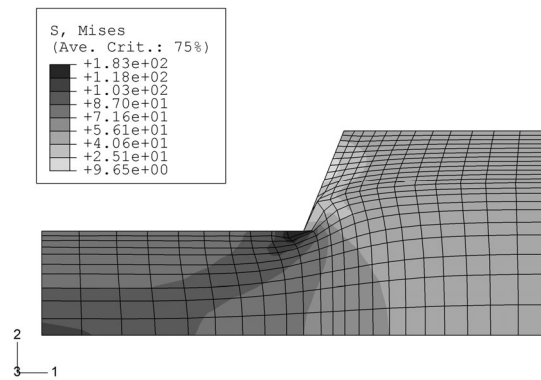
Figure 3.15: Distribution of Mises stress q (MPa) at the end of step 1.
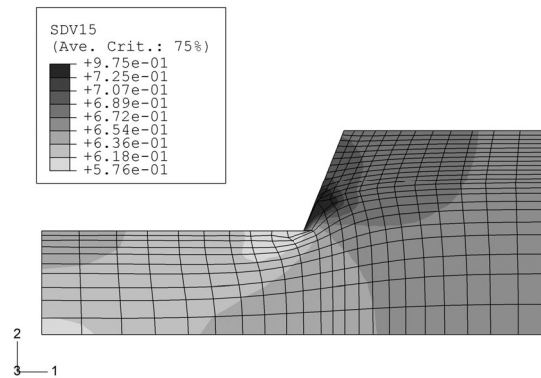
Figure 3.16: Void ratio distribution at the end of step 1.
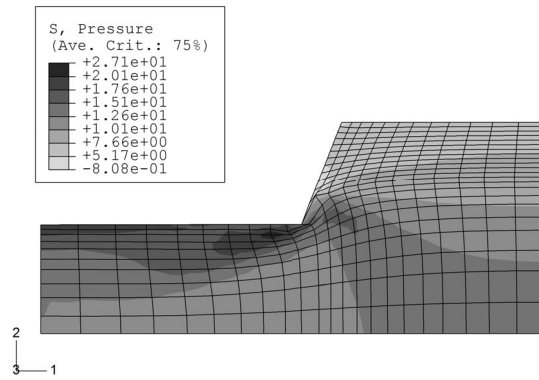
Figure 3.17: Distribution of hydrostatic stress p (MPa) at the end of step 2.
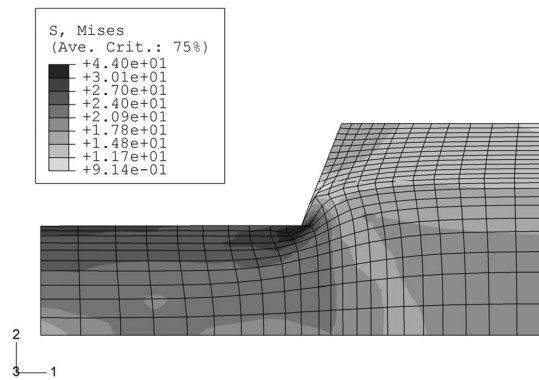
Figure 3.18: Distribution of Mises stress q (MPa) at the end of step 2.
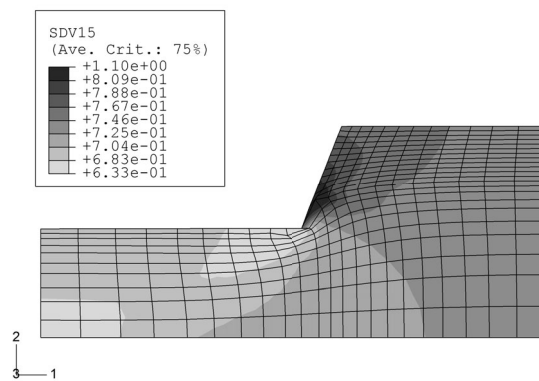
Figure 3.19: Void ratio distribution at the end of step 2.
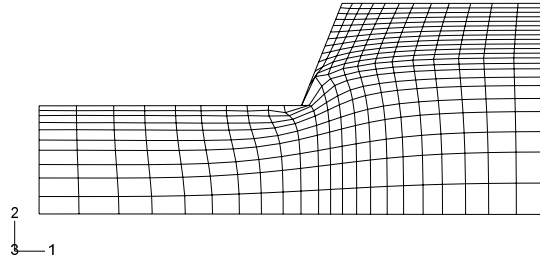
Figure 3.20: Deformed mesh at the end of step 3.
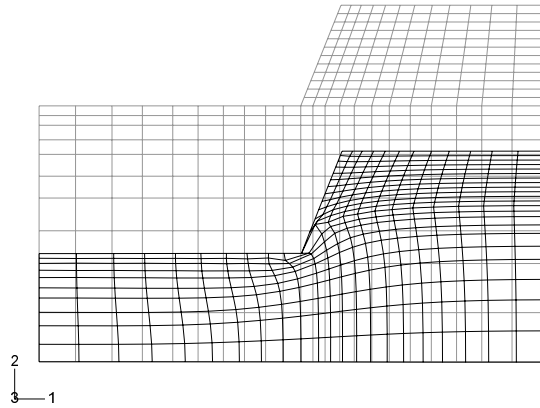
Figure 3.21: Initial and deformed (step 3) meshes.

The residual stress distribution at the end of forming is reported in Figs. 3.22 and 3.23, in terms of hydrostatic stress and Mises stress components. The void ratio distribution is finally shown in Fig. 3.24.

Excluding the small, unrepresentative zone near the corner of the punch, the hydrostatic stress p ranges now between -1.57 MPa and 5.64 MPa and the Mises stress q between 0.89 MPa and 5.87 MPa. Moreover, the void ratio varies between 0.68 and 0.84. It can be noted that the minimum void ratio is not associated with the maximum residual mean stress, it is rather associated with the maximum mean stress reached during loading (step 1). The results suggest that two oblique zones of material are formed, the outer of which
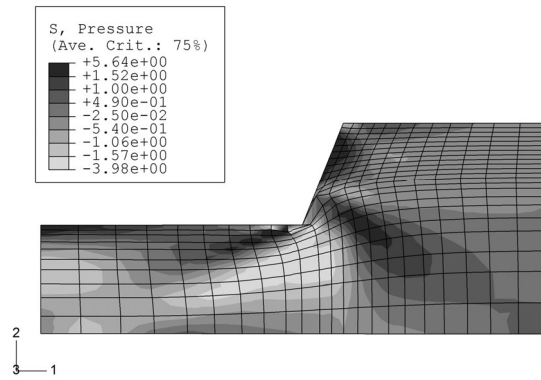
Figure 3.22: Distribution of hydrostatic stress p (MPa) at the end of step 3.
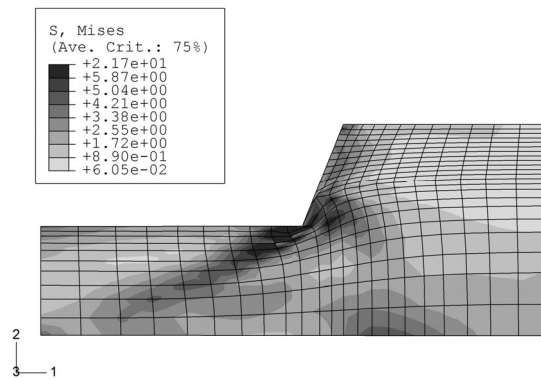
Figure 3.23: Distribution of Mises stress q (MPa) at the end of step 3.
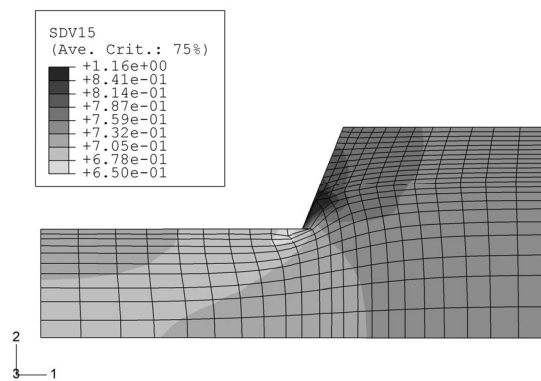
Figure 3.24: Void ratio distribution at the end of step 3.
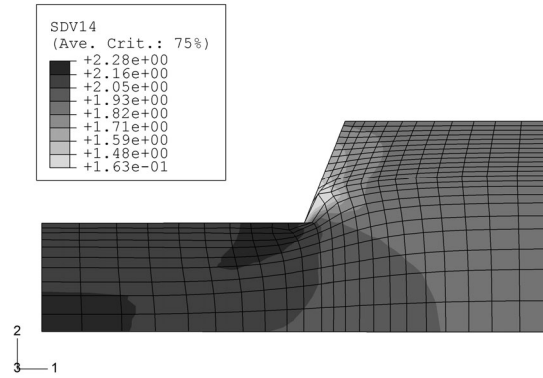
Figure 3.25: Distribution of cohesion c (MPa) at the end of step 3.
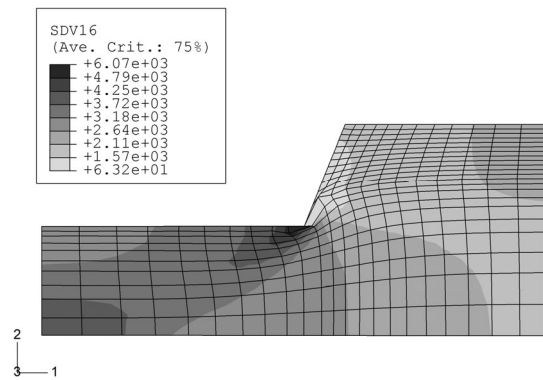
Figure 3.26: Distribution of bulk modulus K_t (MPa) at the end of step 3.
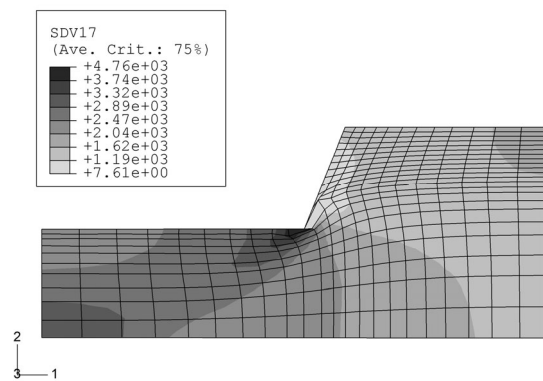
Figure 3.27: Distribution of shear modulus μ (MPa) at the end of step 3.

is subject to high compressive mean stresses, whereas the inner is subject to tensile stresses. This can represent a potentially dangerous situation, in which the tensile stresses tend to open possible microcracks, leading to serious defects formation in the green. However, even when the green is approximately free of macro defects, its mechanical behaviour and shrinkage during future sintering are deeply affected by the inhomogeneities in the residual stress and density distributions.

The cohesion c attained by the material at the end of the overall process is shown in Fig. 3.25, whereas the elastic properties of the final piece are reported in Figs. 3.26 and 3.27, in terms of tangent bulk modulus K_t and shear modulus μ. It can be concluded from the comparison of these maps with Fig. 3.14 that there is a strong relation between mechanical properties gained by the material in the final piece and the maximum mean stress reached during loading (step 1), which seems to be therefore the most important parameter in the forming process.

Experimental and simulated load displacement curves during forming of the piece shown in Fig. 3.9 are compared in Fig. 3.28 (natural and semilogarithmic representations are reported), where a satisfying agreement can be noted.

Results discussed in this section represent an important advance toward the development of a model capable of realistically describing forming processes of ceramic materials. Even if the experimental results are still incomplete and the employed elastoplastic model has been developed in a small strain framework, our results demonstrate that it is possible to realistically predict:

- the springback effect and related shape distortion,

- the force needed for mold ejection,

- the residual stress distribution,

- the gain in cohesion and the final elastic properties,

- the density distribution and the related presence of defects in the green body.

The final remark is related to the prediction of defects in the sintered piece and therefore its investigation has an important practical meaning.

In closure, we mention that the modelling presented in this Chapter can be extended in different directions. Referring to thermoplasticity, the sintering
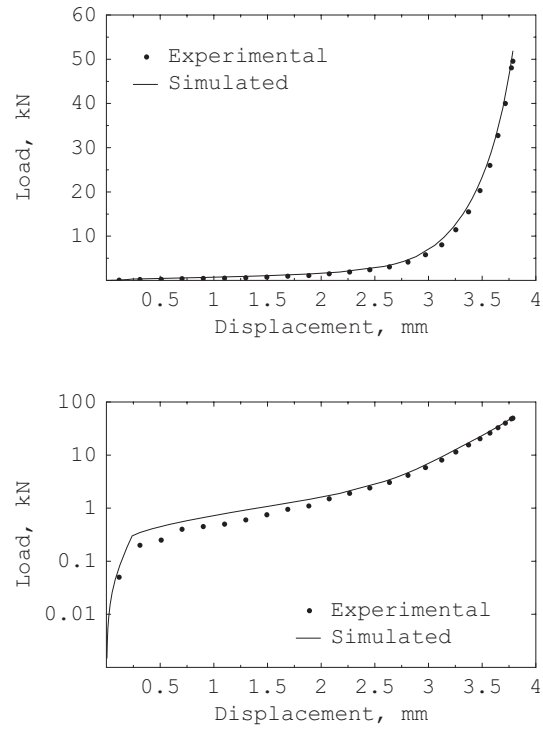
Figure 3.28: Experimental and simulated load vs. displacement curves, in a natural and semilog representation.

phase might be covered by modelling, so that simulation could be extended to the entire production process. Moreover, both sintering aids and powder characteristics might enter the elastic-plastic constitutive laws, so that the optimal powder composition and morphology could be predicted for different forming problems.

Chapter 4

Elastoplastic coupling at large strain

4.1 Introduction

Even if forming of ceramic powders may involve deformations up to 50%, we believe that the 'gross' material behaviour is dominated by nonlinearities already occurring when deformations are still small. Therefore, the infinitesimal theory can often be considered sufficient to describe forming of ceramics. There are however circumstances where a small strain formulation represents only a mere approximation and a large strain analysis is needed. Therefore, it has been considered appropriate to extend the model presented in Chapter 3 to a fully general large strain framework.

A large strain formulation of the model presented in Chapter 3 is given here, following concepts introduced by Hill and Rice (1973) (see also Hill, 1978 and Bigoni, 2000), which does not require any particular choiche of elastic and plastic strain decomposition, elastic law, yield function, flow and hardening rules, so that it naturally embodies the concept of elastoplastic coupling, fundamental in the small strain setting. After the general framework is provided, the multiplicative strain decomposition by Lee (1969) and Willis (1969) is employed together with the requirement that the elastic response is isotropic and all laws provided for the infinitesimal theory are consistently generalized to include large strains. It is shown that the constitutive framework, coupled with the generalized law of small strain formulation, 'spontaneously' leads to a setting involving the Biot stress and its work-conjugate strain measure.

4.2 A premise: the skeleton of large strain elastoplasticity

A broad constitutive framework for isothermal and time independent large elastoplastic deformations is presented, starting from recalling the concept of work coniugacy in the Hill sense (1968, 1978). In particular, employing Ogden's (1984) notation, a pair of symmetric, Lagrangean, stress $\boldsymbol{T}^{(m)}$ and strain $\boldsymbol{E}^{(m)}$ measures[1] are work-conjugate when their scalar product gives the stress power density per unit volume

$$\boldsymbol{T}^{(m)} \cdot \dot{\boldsymbol{E}}^{(m)} = \boldsymbol{S} \cdot \dot{\boldsymbol{F}}, \tag{4.1}$$

where $\boldsymbol{F}$ is the deformation gradient and $\boldsymbol{S}$ the first Piola-Kirchhoff stress tensor

$$\boldsymbol{S} = J\boldsymbol{T}\boldsymbol{F}^{-T} = \boldsymbol{K}\boldsymbol{F}^{-T}, \tag{4.2}$$

in which $J = \det \boldsymbol{F}$ and $\boldsymbol{T}$ and $\boldsymbol{K}$ are the Cauchy and Kirchhoff stresses, respectively.

For integer (poisitive, null or negative) exponent m, we introduce the following Lagrangean strain measures

$$\begin{cases} \boldsymbol{E}^{(m)} = \dfrac{1}{m}(\boldsymbol{U}^m - \boldsymbol{I}), & \text{if } m \neq 0, \\[2mm] \boldsymbol{E}^{(0)} = \log \boldsymbol{U}, & \text{if } m = 0, \end{cases} \tag{4.3}$$

where $\boldsymbol{U} = (\boldsymbol{F}^T \boldsymbol{F})^{1/2}$ is the right stretch tensor. For a given m, $\boldsymbol{E}^{(m)}$ is defined by (4.3) and the corresponding $\boldsymbol{T}^{(m)}$ can be defined imposing eqn. (4.1). For instance, for $m = 2$, the Green-Lagrange strain results from eqn. (4.3) and the eqn. (4.1) provides for $\boldsymbol{T}^{(2)}$ the second Piola-Kirchhoff stress tensors,

$$\boldsymbol{E}^{(2)} = \frac{1}{2}\left(\boldsymbol{U}^2 - \boldsymbol{I}\right), \quad \text{conjugate to} \quad \boldsymbol{T}^{(2)} = J\boldsymbol{F}^{-1}\boldsymbol{T}\boldsymbol{F}^{-T}. \tag{4.4}$$

A conjugate pair of stress and strain that will become useful later is formed by the Biot stress tensor $\boldsymbol{T}^{(1)}$ and the strain measure $\boldsymbol{E}^{(1)}$,

$$\boldsymbol{E}^{(1)} = \boldsymbol{U} - \boldsymbol{I}, \quad \text{conjugate to} \quad \boldsymbol{T}^{(1)} = \frac{1}{2}\left(\boldsymbol{T}^{(2)}\boldsymbol{U} + \boldsymbol{U}\boldsymbol{T}^{(2)}\right). \tag{4.5}$$

It is well-known however that it is not always the easy task of the two above examples to obtain the stress measure conjugated to a given strain of

---

[1] The notation $\boldsymbol{T}^m = \underbrace{\boldsymbol{T}\boldsymbol{T}...\boldsymbol{T}}_{m \text{ times}}$ (or $\boldsymbol{E}^m$) should not be confused with $\boldsymbol{T}^{(m)}$ (or $\boldsymbol{E}^{(m)}$).

the form (4.3). For instance, the conjugate of the logarithmic strain $\boldsymbol{E}^{(0)}$ has a very complex form (Hoger, 1987) which semplifies to the rotated stress only when the two measures itself are coaxial,

$$\boldsymbol{E}^{(0)} = \log \boldsymbol{U} \quad \text{conjugate to} \quad \boldsymbol{T}^{(0)} = \boldsymbol{R}^T \boldsymbol{K} \boldsymbol{R}, \tag{4.6}$$

if and only if

$$\boldsymbol{E}^{(0)} \boldsymbol{T}^{(0)} = \boldsymbol{T}^{(0)} \boldsymbol{E}^{(0)}. \tag{4.7}$$

The coaxiality condition (4.7) is satisfied for isotropic elasticity, but may be not in more general contexts, such as for instance elastoplasticity (Sansour, 2001).

Following Bigoni (2000), inelastic materials are considered that may at any stage of deformation exhibit a purely elastic response for appropriate loading. For these materials, elastic response is assumed to be a one-to-one relation between $\boldsymbol{T}^{(m)}$ and $\boldsymbol{E}^{(m)}$, though depending on the prior inelastic history, i.e.

$$\boldsymbol{T}^{(m)} = \hat{\boldsymbol{T}}^{(m)}(\boldsymbol{E}^{(m)}, \mathcal{K}), \quad \boldsymbol{E}^{(m)} = \hat{\boldsymbol{E}}^{(m)}(\boldsymbol{T}^{(m)}, \mathcal{K}), \tag{4.8}$$

where $\hat{\boldsymbol{T}}^{(m)}$ and $\hat{\boldsymbol{E}}^{(m)}$ are functionals of the prior history of inelastic deformation through the unspecified set $\mathcal{K}$ of variables of generic tensorial nature (thus embracing second-order tensors and scalars). For a purely elastic deformation rate (in other words, at fixed $\mathcal{K}$) we have

$$\dot{\boldsymbol{T}}^{(m)} = \mathbb{E}[\dot{\boldsymbol{E}}^{(m)}], \quad \dot{\boldsymbol{E}}^{(m)} = \mathbb{M}[\dot{\boldsymbol{T}}^{(m)}], \tag{4.9}$$

where

$$\mathbb{E}(\boldsymbol{E}^{(m)}, \mathcal{K}) = \frac{\partial \hat{\boldsymbol{T}}^{(m)}}{\partial \boldsymbol{E}^{(m)}}, \quad \mathbb{M}(\boldsymbol{T}^{(m)}, \mathcal{K}) = \frac{\partial \hat{\boldsymbol{E}}^{(m)}}{\partial \boldsymbol{T}^{(m)}}, \tag{4.10}$$

and obviously

$$\mathbb{E} = \mathbb{M}^{-1}. \tag{4.11}$$

For an increment involving elastic and inelastic strain rates, we may write

$$\dot{\boldsymbol{T}}^{(m)} = \mathbb{E}[\dot{\boldsymbol{E}}^{(m)}] - \dot{\Lambda}\mathbb{E}[\boldsymbol{P}], \quad \dot{\boldsymbol{E}}^{(m)} = \mathbb{M}[\dot{\boldsymbol{T}}^{(m)}] + \dot{\Lambda}\boldsymbol{P}, \tag{4.12}$$

where $\boldsymbol{P} \in \mathsf{Sym}$,

$$\dot{\Lambda}\boldsymbol{P} = -\mathbb{E}^{-1}\frac{\partial \hat{\boldsymbol{T}}^{(m)}}{\partial \mathcal{K}}[\dot{\mathcal{K}}] = \frac{\partial \hat{\boldsymbol{E}}^{(m)}}{\partial \mathcal{K}}[\dot{\mathcal{K}}] \tag{4.13}$$

and the scalar $\dot{\Lambda} \geq 0$, called the plastic multiplier, is null when $\dot{\mathcal{K}} = 0$. A yield surface is assumed at each $\mathcal{K}$. This may be alternatively expressed

as $f_{\boldsymbol{T}^{(m)}}(\boldsymbol{T}^{(m)},\mathcal{K}) \leq 0$ or as $f_{\boldsymbol{E}^{(m)}}(\boldsymbol{E}^{(m)},\mathcal{K}) \leq 0$, thus defining regions of the $\boldsymbol{T}^{(m)}$ or $\boldsymbol{E}^{(m)}$ space, respectively, within which the response is elastic. Prager's consistency condition requires $\dot{f}_{\boldsymbol{T}^{(m)}} = \dot{f}_{\boldsymbol{E}^{(m)}} = 0$, when inelastic strain rate is different from zero. As a consequence, employing the stress space representation, the elastoplastic incremental constitutive equations can be written as

$$\dot{\boldsymbol{T}}^{(m)} = \begin{cases} \mathbb{E}[\dot{\boldsymbol{E}}^{(m)}] - \dfrac{1}{g} < \boldsymbol{Q} \cdot \mathbb{E}[\dot{\boldsymbol{E}}^{(m)}] > \mathbb{E}[\boldsymbol{P}] & \text{if } f(\boldsymbol{T}^{(m)},\mathcal{K}) = 0, \\[2ex] \mathbb{E}[\dot{\boldsymbol{E}}^{(m)}] & \text{if } f(\boldsymbol{T}^{(m)},\mathcal{K}) < 0, \end{cases} \qquad (4.14)$$

where the operator $< \cdot >$ denotes the Macaulay brackets, i.e. $\forall \; \alpha \in \mathbf{R}$, $< \alpha > = (\alpha + |\alpha|)/2$. Moreover, $\boldsymbol{Q} = \partial f_{\boldsymbol{T}^{(m)}}/\partial \boldsymbol{T}^{(m)} \in \mathsf{Sym}$ is the yield function gradient and the plastic modulus

$$g = h + \boldsymbol{Q} \cdot \mathbb{E}[\boldsymbol{P}], \qquad (4.15)$$

is assumed to be strictly positive (a negative plastic modulus would correspond to a so-called locking material, not investigated here). In the Hill (1967b) notation, the hardening modulus h in (4.15) describes *hardening* when positive, *softening* when negative and *perfect plasticity* when null. It is defined as

$$\dot{\Lambda} h = -\frac{\partial f_{\boldsymbol{T}^{(m)}}}{\partial \mathcal{K}} \cdot \dot{\mathcal{K}}. \qquad (4.16)$$

As Hill (1967b) remarks, hardening and softening are not measure-invariant concepts, in the sense that h depends on the choice of $\boldsymbol{T}^{(m)}$ and $\boldsymbol{E}^{(m)}$. Therefore, the nomenclature is, to some extent, arbitrary. Moreover, we remark that, in addition to h, also $\boldsymbol{Q}$, $\boldsymbol{P}$ and $\mathbb{E}$ are measure-dependent. On the contrary, the plastic modulus g can be shown to be measure-independent (Hill, 1967b; Petryk, 2000). Note also that all quantities appearing in the rate equations (4.14) fully depend on the entire path of deformation reckoned from some ground state.

The scalar product of the first equation in (4.14) with $\boldsymbol{Q}$ gives

$$\boldsymbol{Q} \cdot \dot{\boldsymbol{T}}^{(m)} = \boldsymbol{Q} \cdot \mathbb{E}[\dot{\boldsymbol{E}}^{(m)}] - \frac{\boldsymbol{Q} \cdot \mathbb{E}[\boldsymbol{P}]}{g} < \boldsymbol{Q} \cdot \mathbb{E}[\dot{\boldsymbol{E}}^{(m)}] > . \qquad (4.17)$$

In the case when $h > 0$, we note that

$$\mathrm{sgn}(\boldsymbol{Q} \cdot \mathbb{E}[\dot{\boldsymbol{E}}^{(m)}]) = \mathrm{sgn}(\boldsymbol{Q} \cdot \dot{\boldsymbol{T}}^{(m)}).$$

Therefore, assuming $h > 0$ and using (4.17), we obtain the inverse constitutive equations

$$
\dot{\boldsymbol{E}}^{(m)} = \begin{cases} \mathbb{M}[\dot{\boldsymbol{T}}^{(m)}] + \dfrac{1}{h} < \boldsymbol{Q} \cdot \dot{\boldsymbol{T}}^{(m)} > \boldsymbol{P} & \text{if } f(\boldsymbol{T}^{(m)}, \mathcal{K}) = 0, \\[2ex] \mathbb{M}[\dot{\boldsymbol{T}}^{(m)}] & \text{if } f(\boldsymbol{T}^{(m)}, \mathcal{K}) < 0, \end{cases} \tag{4.18}
$$

It may be important to remark that all possible choices of $\boldsymbol{T}^{(m)}$ and $\boldsymbol{E}^{(m)}$ in (4.14) or (4.18) are equivalent and that all resulting constitutive equations respect the requirement of material frame indifference (Truesdell and Noll, 1965).

The above-presented constitutive framework is very general and does not imply a particular choice of

- elastic and plastic strain decomposition,

- hypo- or hyper- elastic law,

- flow and hardening rules.

It is however clear that in order to set up the constitutive modelling of a particular material, we need to introduce specific laws. This objective will be pursued in two steps of deceasing generality: first, we will introduce the specific elastic and plastic decomposition (the multiplicative decomposition will be selected) and requirement of isotropy of the elastic constitutive law, second, a form of elastic constitutive equation capable of describing the elastic range of granular materials will be introduced.

4.3   The multiplicative decomposition and the elastic law

The multiplicative decomposition of deformation gradient $\boldsymbol{F}$ into elastic $\boldsymbol{F}_e$ and plastic $\boldsymbol{F}_p$ components introduced by Lee (1969) and Willis (1969) is adopted (Fig. 4.1)

$$
\boldsymbol{F} = \boldsymbol{F}_e \boldsymbol{F}_p. \tag{4.19}
$$

According to eqn. (4.19), using the left polar decomposition $\boldsymbol{F} = \boldsymbol{V}\boldsymbol{R}$, we introduce the elastic and plastic left stretch and rotation tensors $\boldsymbol{V}_e$, $\boldsymbol{V}_p$, $\boldsymbol{R}_e$ and $\boldsymbol{R}_p$, satisfying

$$
\boldsymbol{F}_e = \boldsymbol{V}_e \boldsymbol{R}_e, \quad \boldsymbol{F}_p = \boldsymbol{V}_p \boldsymbol{R}_p, \tag{4.20}
$$
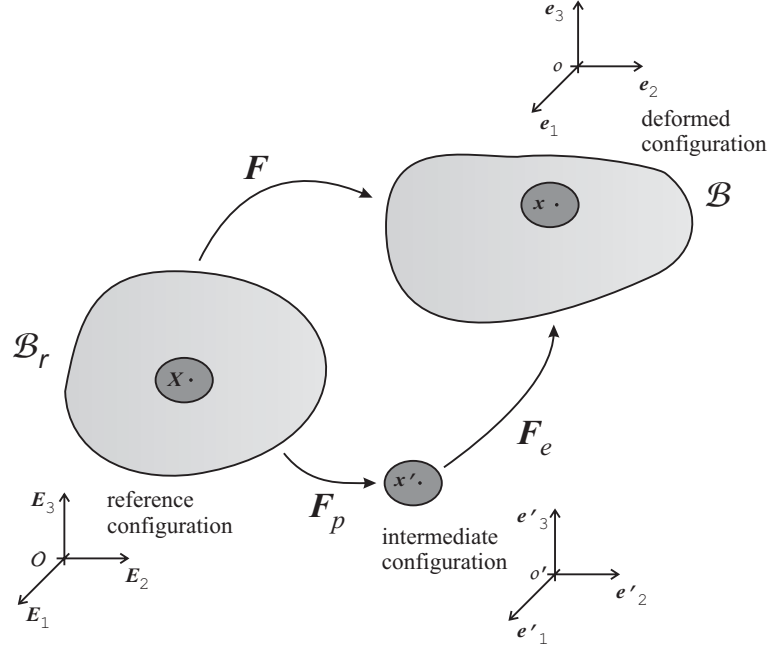
Figure 4.1: Reference, deformed and intermediate configurations.

while using the right polar decomposition $\boldsymbol{F} = \boldsymbol{R}\boldsymbol{U}$, the right elastic and plastic stretch tensors $\boldsymbol{U}_e$ and $\boldsymbol{U}_p$ are defined so that they satisfy

$$\boldsymbol{F}_e = \boldsymbol{R}_e\boldsymbol{U}_e, \quad \boldsymbol{F}_p = \boldsymbol{R}_p\boldsymbol{U}_p. \tag{4.21}$$

An expedient crucial to describe the behaviour of granular materials is to refer to the logarithmic strains defined as

$$\boldsymbol{\epsilon} = \log \boldsymbol{V}, \quad \boldsymbol{\epsilon}_e = \log \boldsymbol{V}_e, \quad \boldsymbol{\epsilon}_p = \log \boldsymbol{V}_p, \tag{4.22}$$

and

$$\boldsymbol{E}^{(0)} = \log \boldsymbol{U}, \quad \boldsymbol{E}_e^{(0)} = \log \boldsymbol{U}_e, \quad \boldsymbol{E}_p^{(0)} = \log \boldsymbol{U}_p. \tag{4.23}$$

The interest in employing the definitions (4.22) and (4.23) is that these allow a decoupling between the volumetric logarithmic elastic and plastic deformations, namely

$$\operatorname{tr} \boldsymbol{\epsilon} = \operatorname{tr} \boldsymbol{\epsilon}_e + \operatorname{tr} \boldsymbol{\epsilon}_p = \operatorname{tr} \boldsymbol{E}^{(0)} = \operatorname{tr} \boldsymbol{E}_e^{(0)} + \operatorname{tr} \boldsymbol{E}_p^{(0)}, \tag{4.24}$$

or, employing the usual definition $J = \det \boldsymbol{F}$ [noting that for every symmetric tensor $\boldsymbol{A}$ the following property holds $\operatorname{tr}(\log \boldsymbol{A}) = \log(\det \boldsymbol{A})$]

$$\log J = \log J_e + \log J_p. \tag{4.25}$$

Let us refer now to an isotropic elastic law relating the Kirchhoff stress $\boldsymbol{K}$ to the elastic deformation gradient $\boldsymbol{F}_e$ in the generic form

$$\boldsymbol{K} = \hat{\boldsymbol{K}}(\boldsymbol{F}_e, k_i), \tag{4.26}$$

where *function $\hat{\boldsymbol{K}}$ may depend also on generic plastic scalar variables k_i, assumed invariant with respect to every symmetry group of the material and change in observer.* Function $\hat{\boldsymbol{K}}$ must satisfy

P1. the isotropy requirement

$$\hat{\boldsymbol{K}}(\boldsymbol{F}_e, k_i) = \hat{\boldsymbol{K}}(\boldsymbol{F}_e \boldsymbol{P}, k_i), \quad \forall \boldsymbol{P} \in \mathsf{Orth}^+, \tag{4.27}$$

P2. the objectivity requirement

$$\hat{\boldsymbol{K}}(\boldsymbol{F}_e, k_i) = \boldsymbol{Q}^T \hat{\boldsymbol{K}}(\boldsymbol{Q}\boldsymbol{F}_e, k_i)\boldsymbol{Q}, \quad \forall \boldsymbol{Q} \in \mathsf{Orth}^+. \tag{4.28}$$

As a consequence of property (**P1**), the rotation in the left polar decomposition does not alter the values of function $\hat{\boldsymbol{K}}$,

$$\hat{\boldsymbol{K}}(\boldsymbol{F}_e, k_i) = \hat{\boldsymbol{K}}(\boldsymbol{V}_e, k_i), \tag{4.29}$$

so that function $\hat{\boldsymbol{K}}$ depends only on the elastic left stretch tensor. If we consider that

$$\boldsymbol{F}_e = \boldsymbol{R}\boldsymbol{U}\boldsymbol{U}_p^{-1}\boldsymbol{R}_p^T, \tag{4.30}$$

isotropy and objectivity allow us to introduce the following transformations

$$\boldsymbol{K} = \hat{\boldsymbol{K}}(\boldsymbol{R}\boldsymbol{U}\boldsymbol{U}_p^{-1}\boldsymbol{R}_p^T, k_i) = \hat{\boldsymbol{K}}(\boldsymbol{R}\boldsymbol{U}\boldsymbol{U}_p^{-1}, k_i) = \boldsymbol{R}\hat{\boldsymbol{K}}(\boldsymbol{U}\boldsymbol{U}_p^{-1}, k_i)\boldsymbol{R}^T, \tag{4.31}$$

so that we get

$$\boldsymbol{K} = \hat{\boldsymbol{K}}(\boldsymbol{F}_e, k_i) = \boldsymbol{R}\hat{\boldsymbol{K}}(\boldsymbol{U}\boldsymbol{U}_p^{-1}, k_i)\boldsymbol{R}^T. \tag{4.32}$$

If now we employ the rotated stress $\boldsymbol{R}^T \boldsymbol{K} \boldsymbol{R}$, we conclude that the following constitutive law can be written

$$\boldsymbol{R}^T \boldsymbol{K} \boldsymbol{R} = \hat{\boldsymbol{K}}(\boldsymbol{U}\boldsymbol{U}_p^{-1}, k_i). \tag{4.33}$$

Now, the rotated stress is related to the Biot stress through (Ogden, 1984)

$$\boldsymbol{T}^{(1)} = \frac{1}{2} \left(\boldsymbol{U}^{-1} \boldsymbol{R}^T \boldsymbol{K} \boldsymbol{R} + \boldsymbol{R}^T \boldsymbol{K} \boldsymbol{R} \boldsymbol{U}^{-1} \right), \tag{4.34}$$

so that in conclusion we obtain

$$\boldsymbol{T}^{(1)} = \frac{1}{2} \left(\boldsymbol{U}^{-1} \hat{\boldsymbol{K}}(\boldsymbol{U}\boldsymbol{U}_p^{-1}, k_i) + \hat{\boldsymbol{K}}(\boldsymbol{U}\boldsymbol{U}_p^{-1}, k_i)\boldsymbol{U}^{-1} \right). \tag{4.35}$$

Since $\boldsymbol{U} = \boldsymbol{E}^{(1)} + \boldsymbol{I}$, eqn. (4.35) expresses a relation between the two work-conjugate measures $\boldsymbol{T}^{(1)}$ and $\boldsymbol{E}^{(1)}$ of the type (4.8), with set $\mathcal{K}$ including now $\boldsymbol{U}_p^{-1}$ and k_i.

It is instructive to see how eqn. (4.35) reduces in the specific case of the infinitesima theory. This is developed in Section 4.6.

4.4   Elastoplastic coupling

The elastic properties of granular materials can be described by a nonlinear elastic law providing a generalization to finite strains of the equation thoroughly discussed in Chapter 3 and admitting the following potential

$$\phi(\boldsymbol{\epsilon}_e, \boldsymbol{\epsilon}_p) = -\frac{\mu}{3}(\operatorname{tr} \boldsymbol{\epsilon}_e)^2 + c \operatorname{tr} \boldsymbol{\epsilon}_e \tag{4.36}$$

$$+ (p_0 + c) \left[\left(d - \frac{1}{d} \right) \frac{(\operatorname{tr} \boldsymbol{\epsilon}_e)^2}{2\tilde{\kappa}} + d^{1/n}\tilde{\kappa} \exp\left(-\frac{\operatorname{tr} \boldsymbol{\epsilon}_e}{d^{1/n}\tilde{\kappa}} \right) \right] + \mu \, \boldsymbol{\epsilon}_e \cdot \boldsymbol{\epsilon}_e,$$

where p_0 is the initial confining pressure, c, d, and μ are scalar parameters depending on the volumetric plastic strain $\operatorname{tr} \boldsymbol{\epsilon}_p = \operatorname{tr} \boldsymbol{E}_p^{(0)}$ and inducing the elastoplastic coupling, $\tilde{\kappa}$ is the elastic logarithmic bulk modulus. The Kirchhoff stress results in the form

$$\boldsymbol{K} = \frac{\partial \phi}{\partial \boldsymbol{\epsilon}_e} = \left\{ -\frac{2}{3}\mu \operatorname{tr} \boldsymbol{\epsilon}_e + c \right. \tag{4.37}$$

$$\left. + (p_0 + c) \left[\left(d - \frac{1}{d} \right) \frac{\operatorname{tr} \boldsymbol{\epsilon}_e}{\tilde{\kappa}} - \exp\left(-\frac{\operatorname{tr} \boldsymbol{\epsilon}_e}{d^{1/n}\tilde{\kappa}} \right) \right] \right\} \boldsymbol{I} + 2\mu \, \boldsymbol{\epsilon}_e.$$

The elastic constitutive law (4.37) can be written in the form (4.26) with

$$\hat{\boldsymbol{K}}(\boldsymbol{F}_e, k_i) = \left\{ -\frac{1}{3}\mu \operatorname{tr} \log \boldsymbol{F}_e \boldsymbol{F}_e^T + c \right. \tag{4.38}$$

$$\left. + (p_0 + c) \left[\left(d - \frac{1}{d} \right) \frac{\operatorname{tr} \log \boldsymbol{F}_e \boldsymbol{F}_e^T}{2\tilde{\kappa}} - \exp\left(-\frac{\operatorname{tr} \log \boldsymbol{F}_e \boldsymbol{F}_e^T}{2d^{1/n}\tilde{\kappa}} \right) \right] \right\} \boldsymbol{I}$$

$$+ \mu \log \boldsymbol{F}_e \boldsymbol{F}_e^T.$$

where the set k_i includes c, d, and μ. It is obvious that eqn. (4.38) can be written in the form (4.35), not reported for conciseness. We are now in a position to explicitly write the fourth-order elastic tensor $\mathbb{E}$ appearing in eqn. (4.10)$_1$. This takes the form

$$\mathbb{E} = -\frac{1}{2}\left(\boldsymbol{U}^{-1}\,\overline{\underline{\otimes}}\,\hat{\boldsymbol{K}}\boldsymbol{U}^{-1} + \hat{\boldsymbol{K}}\boldsymbol{U}^{-1}\,\overline{\underline{\otimes}}\,\boldsymbol{U}^{-1}\right) \tag{4.39}$$
$$+\frac{1}{2}\left(\frac{\partial\boldsymbol{U}^{-1}\hat{\boldsymbol{K}}(\boldsymbol{X},k_i)}{\partial\boldsymbol{X}} + \frac{\partial\hat{\boldsymbol{K}}(\boldsymbol{X},k_i)\boldsymbol{U}^{-1}}{\partial\boldsymbol{X}}\right)_{\boldsymbol{X}=\boldsymbol{U}\boldsymbol{U}_p^{-1}}\left(\boldsymbol{I}\,\overline{\underline{\otimes}}\,\boldsymbol{U}_p^{-1}\right),$$

so that, employing eqn. (4.38), we obtain

$$\frac{\partial\hat{\boldsymbol{K}}(\boldsymbol{X},k_i)}{\partial\boldsymbol{X}} = \tag{4.40}$$
$$\left\{\left[-\frac{\mu}{3} + K_t(\boldsymbol{X})\right]\boldsymbol{I}\otimes\boldsymbol{I} + \mu\boldsymbol{I}\,\overline{\underline{\otimes}}\,\boldsymbol{I}\right\}\left(\frac{\partial\log\boldsymbol{Y}}{\partial\boldsymbol{Y}}\right)_{\boldsymbol{Y}=\boldsymbol{X}\boldsymbol{X}^T}\left(\boldsymbol{I}\,\underline{\otimes}\,\boldsymbol{X} + \boldsymbol{X}\,\overline{\otimes}\,\boldsymbol{I}\right),$$

in which

$$K_t(\boldsymbol{X}) = \frac{p_0 + c}{2\tilde{\kappa}}\left[d - \frac{1}{d} + d^{-1/n}\exp\left(-\frac{\operatorname{tr}\log\boldsymbol{X}\boldsymbol{X}^T}{2d^{1/n}\tilde{\kappa}}\right)\right]. \tag{4.41}$$

and

$$\frac{\partial\log\boldsymbol{Y}}{\partial\boldsymbol{Y}} = \sum_{n=1}^{\infty}\frac{(-1)^{n+1}}{n}\sum_{r=0}^{n-1}(\boldsymbol{Y}-\boldsymbol{I})^r\,\overline{\underline{\otimes}}\,(\boldsymbol{Y}-\boldsymbol{I})^{n-1-r}. \tag{4.42}$$

Note that four tensorial products between second-order tensors $\boldsymbol{A}$ and $\boldsymbol{B}$ have been employed, which can be defined just specifying the way they act on every tensor $\boldsymbol{C}$

$$(\boldsymbol{A}\otimes\boldsymbol{B})[\boldsymbol{C}] = (\boldsymbol{C}\cdot\boldsymbol{B}^T)\boldsymbol{A}, \qquad (\boldsymbol{A}\,\overline{\underline{\otimes}}\,\boldsymbol{B})[\boldsymbol{C}] = \frac{1}{2}\boldsymbol{A}\left(\boldsymbol{C}+\boldsymbol{C}^T\right)\boldsymbol{B}^T,$$
$$(\boldsymbol{A}\,\underline{\otimes}\,\boldsymbol{B})[\boldsymbol{C}] = \boldsymbol{A}\boldsymbol{C}\boldsymbol{B}^T, \qquad (\boldsymbol{A}\,\overline{\otimes}\,\boldsymbol{B})[\boldsymbol{C}] = \boldsymbol{A}\boldsymbol{C}^T\boldsymbol{B}^T, \tag{4.43}$$

so that the following property holds

$$\overline{\underline{\otimes}} = \frac{1}{2}\left(\underline{\otimes} + \overline{\otimes}\right). \tag{4.44}$$

Finally, we remark that truncation of the series expansion (4.42) yields approximations of the derivative of the logarithm of a tensor, which may be

not particularly complicated and often sufficient to practical purposes. For instance, a truncation at third order gives

$$\frac{\partial \log \boldsymbol{Y}}{\partial \boldsymbol{Y}} \doteq \boldsymbol{I} \,\overline{\underline{\otimes}}\, \boldsymbol{I} - \frac{1}{2} \left[\boldsymbol{I} \,\overline{\underline{\otimes}}\, (\boldsymbol{Y} - \boldsymbol{I}) + (\boldsymbol{Y} - \boldsymbol{I}) \,\overline{\underline{\otimes}}\, \boldsymbol{I} \right] \tag{4.45}$$
$$+ \frac{1}{3} \left[\boldsymbol{I} \,\overline{\underline{\otimes}}\, (\boldsymbol{Y} - \boldsymbol{I})^2 + (\boldsymbol{Y} - \boldsymbol{I}) \,\overline{\underline{\otimes}}\, (\boldsymbol{Y} - \boldsymbol{I}) + (\boldsymbol{Y} - \boldsymbol{I})^2 \,\overline{\underline{\otimes}}\, \boldsymbol{I} \right].$$

In the absence of *ad hoc* experimental results, we employ for simplicity a yield function with same form adopted for the infinitesimal theory (see Chapter 3), where the Cauchy stress is replaced by the Biot stress $\boldsymbol{T}^{(1)}$. This can be pursued redefining the invariants p, q and θ in terms of Biot stress

$$p = -\frac{\operatorname{tr} \boldsymbol{T}^{(1)}}{3}, \quad q = \sqrt{3J_2}, \quad \theta = \frac{1}{3} \cos^{-1} \left(\frac{3\sqrt{3}}{2} \frac{J_3}{J_2^{3/2}} \right), \tag{4.46}$$

where $\theta \in [0, \pi/3]$ and

$$J_2 = \frac{1}{2} \operatorname{dev} \boldsymbol{T}^{(1)} \cdot \operatorname{dev} \boldsymbol{T}^{(1)}, \quad J_3 = \frac{1}{3} \operatorname{tr} \left(\operatorname{dev} \boldsymbol{T}^{(1)} \right)^3,$$
$$\operatorname{dev} \boldsymbol{T}^{(1)} = \boldsymbol{T}^{(1)} - \frac{\operatorname{tr} \boldsymbol{T}^{(1)}}{3} \boldsymbol{I} \tag{4.47}$$

and taking the yield function from Chapter 2 (where it has also been motivated from mechanical point of view)

$$F(\boldsymbol{T}^{(1)}, p_c, c) = f(p, p_c, c) + \frac{q}{g(\theta)}, \tag{4.48}$$

where p_c and c are the parameters governing hardening, and

$$f(p, p_c, c) = \begin{cases} -Mp_c\sqrt{(\Phi - \Phi^m)\left[2(1 - \alpha)\Phi + \alpha\right]} & \text{if } \Phi \in [0, 1], \\ +\infty & \text{if } \Phi \notin [0, 1], \end{cases} \tag{4.49}$$

in which

$$\Phi = \frac{p + c(\operatorname{tr} \boldsymbol{E}_p^{(0)})}{p_c(\operatorname{tr} \boldsymbol{E}_p^{(0)}) + c(\operatorname{tr} \boldsymbol{E}_p^{(0)})} \tag{4.50}$$

and

$$g(\theta) = \frac{1}{\cos\left[\beta\dfrac{\pi}{6} - \dfrac{1}{3}\cos^{-1}\left(\gamma\cos 3\theta\right)\right]}. \tag{4.51}$$

Note that M, m, α, β, and γ are material parameters already described in Chapter 2.

The model is now written in the form (4.8) with a properly defined yield function of the type $f_{\boldsymbol{T}^{(1)}}(\boldsymbol{T}^{(1)}, \mathcal{K}) \leq 0$, so that we can jump to the incremental form (4.14), where the elastic fourth-order tensor $\mathbb{E}$ is given by eqns. (4.39)—(4.42) and the flow mode tensor $\boldsymbol{P}$ and yield function gradient $\boldsymbol{Q}$ are given by

$$\boldsymbol{P} = \boldsymbol{Q} - \frac{1}{3}\epsilon\,\mathrm{tr}\,\boldsymbol{Q}\,(1-\Phi)\,\boldsymbol{I}, \quad \boldsymbol{Q} = \frac{\partial F(\boldsymbol{T}^{(1)}, p_c, c)}{\partial \boldsymbol{T}^{(1)}}, \qquad (4.52)$$

where $0 < \epsilon < 1$ and the form of $\boldsymbol{Q}$ can be obtained from eqns. (2.14)—(2.16) of Chapter 2, replacing $\boldsymbol{\sigma}$ with $\boldsymbol{T}^{(1)}$.

The hardening law eqn. (4.16) is similar to the analogous equation introduced in Chapter 3. In particular, we have

$$\dot{\Lambda} h = -\left(\frac{\partial F}{\partial p_c}\dot{p}_c + \frac{\partial F}{\partial c}\dot{c}\right), \qquad (4.53)$$

where

$$\frac{\partial F}{\partial p_c} = -M\sqrt{(\Phi - \Phi^m)\,[2(1-\alpha)\Phi + \alpha]} \qquad (4.54)$$

$$+ M\frac{p_c(p+c)}{(p_c+c)^2}\frac{\left(1 - m\Phi^{m-1}\right)[2(1-\alpha)\Phi + \alpha] + 2(1-\alpha)\,(\Phi - \Phi^m)}{2\sqrt{(\Phi - \Phi^m)\,[2(1-\alpha)\Phi + \alpha]}},$$

and

$$\frac{\partial F}{\partial c} = -M\frac{p_c(p_c - p)}{(p_c+c)^2}\cdot \qquad (4.55)$$

$$\cdot\frac{\left(1 - m\Phi^{m-1}\right)[2(1-\alpha)\Phi + \alpha] + 2(1-\alpha)\,(\Phi - \Phi^m)}{2\sqrt{(\Phi - \Phi^m)\,[2(1-\alpha)\Phi + \alpha]}},$$

in which

$$\dot{p}_c = -\frac{p_c^2\exp(\mathrm{tr}\,\boldsymbol{E}_p^{(0)})}{\tilde{a}_1\Lambda_1\exp\left(-\dfrac{\Lambda_1}{p_c}\right) + \tilde{a}_2\Lambda_2\exp\left(-\dfrac{\Lambda_2}{p_c}\right)}\,\mathrm{tr}\,\dot{\boldsymbol{E}}_p^{(0)}, \qquad (4.56)$$

and

$$\dot{c} = c_\infty\Gamma\,H(p_c - p_{cb})\exp\left[-\Gamma(p_c - p_{cb})\right]\dot{p}_c. \qquad (4.57)$$

Parameters Λ_1, Λ_2, $\tilde{a}_1$, $\tilde{a}_2$, c_∞, Γ, and p_{cb} have been introduced and motivated in Chapter 3.

Since the hardening is governed by the accumulated plastic deformation, $\mathrm{tr}\boldsymbol{E}_p^{(0)}$, the knowledge of the evolution law for this variable is needed to complete the formulation. In particular eqn. $(4.13)_1$ can be develped to yield

$$\dot{\Lambda}\boldsymbol{P} = \mathbb{G}\left[\dot{\boldsymbol{E}}_p^{(0)}\right], \tag{4.58}$$

where tensor $\mathbb{G}$, assumed positive definite, is given by

$$
\begin{aligned}
\mathbb{G} \;=\; & -\frac{1}{2}\xi_2\,\mathbb{E}^{-1}\left[\left(\boldsymbol{U}^{-1}\frac{\partial\hat{\boldsymbol{K}}}{\partial c} + \frac{\partial\hat{\boldsymbol{K}}}{\partial c}\boldsymbol{U}^{-1}\right)\otimes\boldsymbol{I}\right] \\
& -\frac{1}{2}\xi_3\,\mathbb{E}^{-1}\left[\left(\boldsymbol{U}^{-1}\frac{\partial\hat{\boldsymbol{K}}}{\partial d} + \frac{\partial\hat{\boldsymbol{K}}}{\partial d}\boldsymbol{U}^{-1}\right)\otimes\boldsymbol{I}\right] \\
& -\frac{1}{2}\xi_4\,\mathbb{E}^{-1}\left[\left(\boldsymbol{U}^{-1}\frac{\partial\hat{\boldsymbol{K}}}{\partial\mu} + \frac{\partial\hat{\boldsymbol{K}}}{\partial\mu}\boldsymbol{U}^{-1}\right)\otimes\boldsymbol{I}\right] \\
& +\frac{1}{2}\,\mathbb{E}^{-1}\left(\frac{\partial\boldsymbol{U}^{-1}\hat{\boldsymbol{K}}(\boldsymbol{X})}{\partial\boldsymbol{X}} + \frac{\partial\hat{\boldsymbol{K}}(\boldsymbol{X})\boldsymbol{U}^{-1}}{\partial\boldsymbol{X}}\right)_{\boldsymbol{X}=\boldsymbol{U}\boldsymbol{U}_p^{-1}} \\
& \cdot\left(\boldsymbol{U}\boldsymbol{U}_p^{-1}\,\overline{\underline{\otimes}}\,\boldsymbol{U}_p^{-1}\right)\frac{\partial\exp\boldsymbol{E}_p^{(0)}}{\partial\boldsymbol{E}_p^{(0)}},
\end{aligned}
\tag{4.59}
$$

in which

$$
\frac{\partial\hat{\boldsymbol{K}}}{\partial c} = \tag{4.60}
$$
$$
\left\{1 + \left[\left(d - \frac{1}{d}\right)\frac{\mathrm{tr}\log\boldsymbol{U}\boldsymbol{U}_p^{-2}\boldsymbol{U}}{2\tilde{\kappa}} - \exp\left(-\frac{\mathrm{tr}\log\boldsymbol{U}\boldsymbol{U}_p^{-2}\boldsymbol{U}}{2d^{1/n}\tilde{\kappa}}\right)\right]\right\}\boldsymbol{I},
$$

$$
\frac{\partial\hat{\boldsymbol{K}}}{\partial d} = \left\{\frac{(p_0 + c)\,\mathrm{tr}\log\boldsymbol{U}\boldsymbol{U}_p^{-2}\boldsymbol{U}}{2\tilde{\kappa}}\left[1 + \frac{1}{d^2}\right.\right. \tag{4.61}
$$
$$
\left.\left.-\frac{1}{2nd^{1+1/n}}\exp\left(-\frac{\mathrm{tr}\log\boldsymbol{U}\boldsymbol{U}_p^{-2}\boldsymbol{U}}{2d^{1/n}\tilde{\kappa}}\right)\right]\right\}\boldsymbol{I},
$$

$$
\frac{\partial\hat{\boldsymbol{K}}}{\partial\mu} = \left(-\frac{1}{3}\,\mathrm{tr}\log\boldsymbol{U}\boldsymbol{U}_p^{-2}\boldsymbol{U}\right)\boldsymbol{I} + \log\boldsymbol{U}\boldsymbol{U}_p^{-2}\boldsymbol{U}, \tag{4.62}
$$

and

$$\xi_2 = -\frac{c_\infty \Gamma \, H(p_c - p_{cb}) \exp\left[-\Gamma(p_c - p_{cb})\right] p_c^2 \exp(\operatorname{tr} \boldsymbol{E}_p^{(0)})}{\tilde{a}_1 \Lambda_1 \exp\left(-\dfrac{\Lambda_1}{p_c}\right) + \tilde{a}_2 \Lambda_2 \exp\left(-\dfrac{\Lambda_2}{p_c}\right)}, \tag{4.63}$$

$$\xi_3 = -\frac{B \, H(p_c - p_{cb}) \, p_c^2 \exp(\operatorname{tr} \boldsymbol{E}_p^{(0)})}{\tilde{a}_1 \Lambda_1 \exp\left(-\dfrac{\Lambda_1}{p_c}\right) + \tilde{a}_2 \Lambda_2 \exp\left(-\dfrac{\Lambda_2}{p_c}\right)}, \tag{4.64}$$

$$\xi_4 = \left(d - \frac{1}{d}\right) \mu_1 \xi_2 + c\left(1 + \frac{1}{d^2}\right) \mu_1 \xi_3. \tag{4.65}$$

Note that the exponential of a tensor has been introduced in eqn. (4.59), defined as

$$\frac{\partial \exp \boldsymbol{E}_p^{(0)}}{\partial \boldsymbol{E}_p^{(0)}} = \sum_{n=1}^{\infty} \frac{1}{n!} \sum_{r=0}^{n-1} \left(\boldsymbol{E}_p^{(0)}\right)^r \underline{\overline{\otimes}} \left(\boldsymbol{E}_p^{(0)}\right)^{n-1-r}, \tag{4.66}$$

which, truncated at the third order becomes

$$\frac{\partial \exp \boldsymbol{E}_p^{(0)}}{\partial \boldsymbol{E}_p^{(0)}} \doteq \boldsymbol{I} \, \underline{\overline{\otimes}} \, \boldsymbol{I} + \frac{1}{2} \left(\boldsymbol{I} \, \underline{\overline{\otimes}} \, \boldsymbol{E}_p^{(0)} + \boldsymbol{E}_p^{(0)} \, \underline{\overline{\otimes}} \, \boldsymbol{I}\right) \tag{4.67}$$
$$+ \frac{1}{6} \left[\boldsymbol{I} \, \underline{\overline{\otimes}} \, (\boldsymbol{E}_p^{(0)})^2 + \boldsymbol{E}_p^{(0)} \, \underline{\overline{\otimes}} \, \boldsymbol{E}_p^{(0)} + (\boldsymbol{E}_p^{(0)})^2 \, \underline{\overline{\otimes}} \, \boldsymbol{I}\right].$$

4.5 A summary of the equations governing the finite strain model

In this section we provide a brief summary of the equations that compose the constitutive model in the large strain framework. The elastoplastic incremental constitutive equations take the form

$$\dot{\boldsymbol{T}}^{(1)} = \begin{cases} \mathbb{E}[\dot{\boldsymbol{E}}^{(1)}] - \dfrac{1}{g} < \boldsymbol{Q} \cdot \mathbb{E}[\dot{\boldsymbol{E}}^{(1)}] > \mathbb{E}[\boldsymbol{P}] & \text{if } f(\boldsymbol{T}^{(1)}, p_c, c) = 0, \\[2ex] \mathbb{E}[\dot{\boldsymbol{E}}^{(1)}] & \text{if } f(\boldsymbol{T}^{(1)}, p_c, c) < 0, \end{cases} \tag{4.68}$$

where $\boldsymbol{T}^{(1)}$ is the Biot stress and $\boldsymbol{E}^{(1)} = \boldsymbol{U} - \boldsymbol{I}$ is the corresponding work conjugate strain measure. The elastic tensor $\mathbb{E}$ is given in eqns. (4.39)–(4.42). The yield fuction $f(\boldsymbol{T}^{(1)}, p_c, c)$ and its gradient $\boldsymbol{Q} = \partial f / \partial \boldsymbol{T}^{(1)}$ are obtained

from those defined in Chapter 2, replacing the Cauchy stress with the Biot stress $\boldsymbol{T}^{(1)}$, eqns. (4.46)–(4.51). The flow mode tensor $\boldsymbol{P}$ is defined by the following flow rule

$$\boldsymbol{P} = \boldsymbol{Q} - \frac{1}{3}\epsilon \operatorname{tr}\boldsymbol{Q}\,(1 - \Phi)\,\boldsymbol{I}, \qquad (4.69)$$

where ϵ is a material parameter and $\Phi = (p+c)/(p_c+c)$. The plastic modulus g, assumed to be strictly positive, is given by

$$g = h + \boldsymbol{Q} \cdot \mathbb{E}[\boldsymbol{P}],$$

where h is the hardening modulus. The hardening modulus is obtained substituting eqn. (4.58) in eqns. (4.56)–(4.57) and eqn. (4.53), yielding

$$h = - \left(\frac{\partial F}{\partial p_c}\bar{p}_c + \frac{\partial F}{\partial c}\bar{c} \right), \qquad (4.70)$$

where $\partial F/\partial p_c$ and $\partial F/\partial c$ are given in eqns. (4.54)–(4.55) and

$$\bar{p}_c = -\frac{p_c^2 \exp(\operatorname{tr}\boldsymbol{E}_p^{(0)})}{\tilde{a}_1\Lambda_1 \exp\left(-\dfrac{\Lambda_1}{p_c}\right) + \tilde{a}_2\Lambda_2 \exp\left(-\dfrac{\Lambda_2}{p_c}\right)} \operatorname{tr}\mathbb{G}^{-1}[\boldsymbol{P}],$$
$$\qquad (4.71)$$

$$\bar{c} = c_\infty \Gamma\, H(p_c - p_{cb}) \exp\left[-\Gamma(p_c - p_{cb})\right] \bar{p}_c,$$

Finally, the tensor $\mathbb{G}$ is given in eqns. (4.59)–(4.66).

4.6 Reduction to the case of infinitesimal theory

If the gradient of displacement vector $\boldsymbol{u}$ is assumed to represent a small parameter,

$$\boldsymbol{U}^2 = \boldsymbol{I} + 2\boldsymbol{\epsilon} + o(\boldsymbol{\epsilon}^2) \doteq \boldsymbol{I} + 2\boldsymbol{\epsilon}, \qquad (4.72)$$

where $\boldsymbol{\epsilon} = (\nabla\boldsymbol{u} + \nabla\boldsymbol{u}^T)/2$ is the infinitesimal strain and the symbol $\doteq$ is used with obvious meaning, we readily obtain

$$\boldsymbol{U} \doteq \boldsymbol{I} + \boldsymbol{\epsilon}, \quad \boldsymbol{U}^{-1} \doteq \boldsymbol{I} - \boldsymbol{\epsilon}, \quad \boldsymbol{R} \doteq \boldsymbol{I} + \boldsymbol{W}, \quad \boldsymbol{R}^T \doteq \boldsymbol{I} - \boldsymbol{W}, \qquad (4.73)$$

where $\boldsymbol{W} = (\nabla\boldsymbol{u} - \nabla\boldsymbol{u}^T)/2$ is the infinitesimal rotation. It follows from (4.73) and the definitions (4.4) and (4.5) that

$$\boldsymbol{E}^{(1)} \doteq \boldsymbol{E}^{(2)} \doteq \boldsymbol{\epsilon}. \qquad (4.74)$$

Assuming small both the elastic and the plastic contributes to the displacement gradient, we see that (4.33) reduces to

$$\hat{\boldsymbol{K}}(\boldsymbol{U}\boldsymbol{U}_p^{-1}, k_i) \doteq \hat{\boldsymbol{K}}(\boldsymbol{I} + \boldsymbol{\epsilon} - \boldsymbol{\epsilon}_p, k_i), \tag{4.75}$$

from which the infinitesimal additive decomposition of elastic and plastic deformations becomes transparent.

Considering now eqn. (4.35), this approximates to

$$\boldsymbol{T}^{(1)} \doteq \frac{1}{2}\left((\boldsymbol{I} - \boldsymbol{\epsilon})\hat{\boldsymbol{K}}(\boldsymbol{I} + \boldsymbol{\epsilon} - \boldsymbol{\epsilon}_p, k_i) + \hat{\boldsymbol{K}}(\boldsymbol{I} + \boldsymbol{\epsilon} - \boldsymbol{\epsilon}_p, k_i)(\boldsymbol{I} - \boldsymbol{\epsilon})\right). \tag{4.76}$$

Taking the Taylor series expansion of function $\hat{\boldsymbol{K}}$ yields

$$\hat{\boldsymbol{K}}(\boldsymbol{I} + \boldsymbol{\epsilon} - \boldsymbol{\epsilon}_p, k_i) \doteq \hat{\boldsymbol{K}}(\boldsymbol{I}, k_i) + \left(\frac{\partial \hat{\boldsymbol{K}}(\boldsymbol{I} + \boldsymbol{X}, k_i)}{\partial \boldsymbol{X}}\right)_{\boldsymbol{X}=\boldsymbol{0}}[\boldsymbol{\epsilon} - \boldsymbol{\epsilon}_p]. \tag{4.77}$$

The term $\hat{\boldsymbol{K}}(\boldsymbol{I})$ represents a pre-stress that is usually neglected in the infinitesimal theory, continuing with this approximation and using (4.77) into (4.76), gives

$$\boldsymbol{T}^{(1)} \doteq \left(\frac{\partial \hat{\boldsymbol{K}}(\boldsymbol{I} + \boldsymbol{X}, k_i)}{\partial \boldsymbol{X}}\right)_{\boldsymbol{X}=\boldsymbol{0}}[\boldsymbol{\epsilon} - \boldsymbol{\epsilon}_p]. \tag{4.78}$$

Finally, taking into account that the infinitesimal theory is recovered when terms differentiating $\boldsymbol{T}^{(1)}$ from $\boldsymbol{\sigma}$ are neglected and identifying the fourth-order tensor in eqn. (4.78) with the elasticity tensor, the well-known setting of the infinitesimal theory is fully recovered. Note that if this elasticity tensor depends on the plastic deformation, the elastoplastic coupling is also recovered.

Chapter 5

Flutter instability in granular materials

5.1 Introduction

Flutter instability is a form of material instability corresponding to the occurrence of complex conjugate eigenvalues of the acoustic tensor (Rice, 1977). As related to Coulomb friction at the microscale, this instability is believed to represent a key feature in the deformation of granular materials. While the possibility of occurrence of flutter instability has been thoroughly investigated (see, among others, An and Schaeffer, 1990; Loret, 1992; Bigoni and Zaccaria, 1994; Bigoni, 1995; Bigoni and Loret, 1999; Loret et al. 2000), its mechanical consequences are almost unexplored. These are of fundamental importance, since they serve to identify flutter as a phenomenon occurring in real problems.

To shed light on this problem, a perturbative approach is developed in this section, following and generalizing an idea by Bigoni and Capuani (2002) for strain localization. In particular, limiting the analysis to the loading branch of the constitutive elastoplastic operator (see Bigoni and Petryk, 2002 for a discussion on this delicate point), we consider an infinite body, homogeneously and quasi-statically deformed in plane strain. This configuration is dynamically perturbed by superposition of a pulsating dipole (two equal and opposite forces having a magnitude sinusoidally changing with time) and the resulting effects are investigated. To this purpose, a dynamic, infinite body Green's function is obtained for the loading branch of a constitutive equation exhibiting flutter instability (taken from Bigoni and Petryk, 2002). The result is new and is obtained employing the Willis (1973; 1980; 1991) formalism. It is however limited to the case in which the eigenvalues of the acoustic tensor are still real, but the solution can be employed until the limit of flutter (thus

following Bigoni and Capuani, where shear bands have been explored using perturbations still within the elliptic range). It is shown that flutter instability is essentially different from shear bands, in the sense that the latter instability becomes already evident when the boundary of loss of ellipticity is approached, while the former remains undetected until the eigenvalues lies in the real range.

5.2 The constitutive model

Assuming an objective symmetric flux of the Kirchhoff stress $\overset{\circ}{\boldsymbol{K}}$ and the stretching (or Eulerian strain rate) $\boldsymbol{D}$ as measures of stress and strain rates, respectively, we consider an elastoplastic constitutive model of the form

$$
\overset{\circ}{\boldsymbol{K}} =
\begin{cases}
\mathbb{E}[\boldsymbol{D}] - \dfrac{1}{H} \langle \boldsymbol{Q} \cdot \mathbb{E}[\boldsymbol{D}] \rangle \, \mathbb{E}[\boldsymbol{P}] & \text{if } f(\boldsymbol{K}, \mathcal{K}) = 0, \\[2ex]
\mathbb{E}[\boldsymbol{D}] & \text{if } f(\boldsymbol{K}, \mathcal{K}) < 0,
\end{cases}
\tag{5.1}
$$

where the symbol $\langle \cdot \rangle$ denotes the Macaulay brackets operator (defined for every scalar α as $\langle \alpha \rangle = (\alpha + |\alpha|)/2$), $\mathbb{E}$ is the elastic fourth-order tensor, f is the yield function in stress space depending on a collection $\mathcal{K}$ of internal variables (of arbitrary scalar or tensorial nature); moreover, $\boldsymbol{P}$ and $\boldsymbol{Q}$ are the normals to the plastic potential and yield surface, respectively, and the plastic modulus H is related to the hardening modulus h through

$$
H = h + \boldsymbol{Q} \cdot \mathbb{E}[\boldsymbol{P}].
\tag{5.2}
$$

We can identify $\overset{\circ}{\boldsymbol{K}}$ with the Oldroyd derivative,

$$
\overset{\circ}{\boldsymbol{K}} = \dot{\boldsymbol{K}} - \boldsymbol{L}\boldsymbol{K} - \boldsymbol{K}\boldsymbol{L}^T,
\tag{5.3}
$$

where $\boldsymbol{L} = \dot{\boldsymbol{F}}\boldsymbol{F}^{-1}$ is the spatial velocity gradient, and $\boldsymbol{F}$ the deformation gradient. Considering now the loading branch, $\boldsymbol{Q} \cdot \mathbb{E}[\boldsymbol{D}] > 0$, we get

$$
\dot{\boldsymbol{K}} = \mathbb{E}[\boldsymbol{L}] + \boldsymbol{L}\boldsymbol{K} + \boldsymbol{K}\boldsymbol{L}^T - \dfrac{1}{H}(\mathbb{E}[\boldsymbol{P}] \otimes \mathbb{E}[\boldsymbol{Q}])[\boldsymbol{L}],
\tag{5.4}
$$

in which we have made use of the minor symmetries of $\mathbb{E}$. Finally, the relation $\boldsymbol{K} = \boldsymbol{S}\boldsymbol{F}^T$, between the Kirchhoff stress $\boldsymbol{K}$ and the first Piola-Kirchhoff stress $\boldsymbol{S}$, leads to the explicit relation

$$
\dot{\boldsymbol{S}} = \mathbb{C}[\dot{\boldsymbol{F}}],
\tag{5.5}
$$

with

$$\mathbb{C} = (\boldsymbol{I} \boxtimes \boldsymbol{F}^{-1})\mathbb{E}(\boldsymbol{I} \boxtimes \boldsymbol{F}^{-T}) + \boldsymbol{I} \boxtimes \boldsymbol{F}^{-1}\boldsymbol{S} \tag{5.6}$$
$$- \frac{1}{H}(\boldsymbol{I} \boxtimes \boldsymbol{F}^{-1})(\mathbb{E}[\boldsymbol{P}] \otimes \mathbb{E}[\boldsymbol{Q}])(\boldsymbol{I} \boxtimes \boldsymbol{F}^{-T}),$$

where the simbol $\boxtimes$ denotes the tensorial product defined as

$$(\boldsymbol{A} \boxtimes \boldsymbol{B})\,[\boldsymbol{C}] = \boldsymbol{A}\boldsymbol{C}\boldsymbol{B}^{T}. \tag{5.7}$$

5.2.1 Anisotropic elasticity

We assume an anisotropic elastic law of the form

$$\mathbb{E} = \lambda\boldsymbol{B} \otimes \boldsymbol{B} + 2\mu\boldsymbol{B}\,\overline{\underline{\otimes}}\,\boldsymbol{B}, \tag{5.8}$$

where λ and μ are material constants subject to the restrictions $\mu > 0$ and $3\lambda + 2\mu > 0$, $\boldsymbol{B}$ is a symmetric and positive definite second-order tensor, namely

$$\boldsymbol{B} = b_1\boldsymbol{b} \otimes \boldsymbol{b} + b_2(\boldsymbol{I} - \boldsymbol{b} \otimes \boldsymbol{b}), \tag{5.9}$$

which is simply the spectral representation of $\boldsymbol{B}$, so that b_1 and b_2 are the eigenvalues of $\boldsymbol{B}$, while the line spanned by $\boldsymbol{b}$ and the plane (through $\boldsymbol{0}$) perpendicular to $\boldsymbol{b}$ are the corresponding eigenspaces. Moreover the material constants b_1 and b_2 are assumed to depend on a single angular parameter $\hat{b}$, restricted to the range $]0°, 90°[$ for the positive definiteness of $\boldsymbol{B}$,

$$b_1 = \sqrt{3}\cos\hat{b}, \quad b_2 = \sqrt{\frac{3}{2}}\sin\hat{b}, \tag{5.10}$$

so that the isotropic behaviour is recovered when $b_1 = b_2 = 1$, or $\hat{b} \approx 54.74°$. Note that the tangent constitutive operator $\mathbb{C}$ in eqn. (5.6) coupled with the anisotropic elastic tensor $\mathbb{E}$ defined by eqns. (5.8)–(5.10) does not have in general the major symmetry.

5.2.2 Acoustic tensor

The acoustic tensor $\boldsymbol{A}^{ep}(\boldsymbol{n})$ associated with the tangent constitutive operator $\mathbb{C}$ is defined by the identity $\boldsymbol{A}^{ep}(\boldsymbol{n})\boldsymbol{g} = \mathbb{C}[\boldsymbol{g} \otimes \boldsymbol{n}]\boldsymbol{n}$, where $\boldsymbol{n}$ and $\boldsymbol{g}$ are the direction and amplitude of wave propagation, respectively. Thus the acoustic tensor corresponding to $\mathbb{C}$ in eqn. (5.6) is

$$\boldsymbol{A}^{ep}(\boldsymbol{n}) = \boldsymbol{A}^{e}(\boldsymbol{n}) - \frac{1}{H}\left(\mathbb{E}[\boldsymbol{P}]\boldsymbol{F}^{-T}\boldsymbol{n} \otimes \mathbb{E}[\boldsymbol{Q}]\boldsymbol{F}^{-T}\boldsymbol{n}\right), \tag{5.11}$$

where $\boldsymbol{A}^e(\boldsymbol{n})$ is the elastic acoustic tensor, defined as

$$\begin{aligned}
\boldsymbol{A}^e(\boldsymbol{n}) = (\lambda + \mu)(\boldsymbol{B}\boldsymbol{F}^{-T}\boldsymbol{n}) \otimes (\boldsymbol{B}\boldsymbol{F}^{-T}\boldsymbol{n}) \\
+ \mu\left[(\boldsymbol{F}^{-T}\boldsymbol{n}) \cdot (\boldsymbol{B}\boldsymbol{F}^{-T}\boldsymbol{n})\right]\boldsymbol{B} + \left[\boldsymbol{n} \cdot (\boldsymbol{F}^{-1}\boldsymbol{S}\boldsymbol{n})\right]\boldsymbol{I}
\end{aligned} \tag{5.12}$$

Due to the fact that $\mathbb{C}$ does not have the major symmetry, the acoustic tensor (5.11)–(5.12) is not symmetric.

5.3   Plane problem

From now on we take the current configuration as reference, so that $\boldsymbol{F} = \boldsymbol{I}$ and $\boldsymbol{S} = \boldsymbol{K}$ momentarily. Let us turn our attention to the plane problem in which it is assumed that the vector $\boldsymbol{b}$ lies in the plane spanned by $\boldsymbol{k}_1$ and $\boldsymbol{k}_2$, which are two of unit eigenvectors $\boldsymbol{k}_i$ ($i = 1, 2, 3$) of $\boldsymbol{K}$. We are interested in analysing the propagation direction $\boldsymbol{n}$ also lying in the plane spanned by $\boldsymbol{k}_1$ and $\boldsymbol{k}_2$. Assuming the Drucker-Prager yield criterion, the tensors $\boldsymbol{P}$ and $\boldsymbol{Q}$ take the forms

$$\boldsymbol{P} = \cos\chi\, \frac{\mathrm{dev}(\boldsymbol{T})}{|\mathrm{dev}(\boldsymbol{T})|} + \frac{\sin\chi}{\sqrt{3}}\,\boldsymbol{I}, \quad \boldsymbol{Q} = \cos\psi\, \frac{\mathrm{dev}(\boldsymbol{T})}{|\mathrm{dev}(\boldsymbol{T})|} + \frac{\sin\psi}{\sqrt{3}}\,\boldsymbol{I}, \tag{5.13}$$

respectively, where $\boldsymbol{T}$ is the Cauchy stress and $\mathrm{dev}(\cdot)$ is the linear operator giving the deviatoric part of a second-order tensor. The angular parameters χ and ψ represent the dilatancy and the pressure sensitivity of the material, respectively.

It is convenient now to choose $\{\boldsymbol{n}, \boldsymbol{s}, \boldsymbol{k}_3\}$, where $\boldsymbol{s} = \boldsymbol{k}_3 \times \boldsymbol{n}$, as the reference basis. Thus, we can easily obtain the components of the acoustic tensor $\boldsymbol{A}^{ep}(\boldsymbol{n})$, and get it in matrix form

$$\begin{pmatrix}
A^e_{nn} - \dfrac{1}{H}(\boldsymbol{n} \cdot \boldsymbol{q})(\boldsymbol{n} \cdot \boldsymbol{p}) & A^e_{ns} - \dfrac{1}{H}(\boldsymbol{n} \cdot \boldsymbol{q})(\boldsymbol{s} \cdot \boldsymbol{p}) & 0 \\[2ex]
A^e_{ns} - \dfrac{1}{H}(\boldsymbol{s} \cdot \boldsymbol{q})(\boldsymbol{n} \cdot \boldsymbol{p}) & A^e_{ss} - \dfrac{1}{H}(\boldsymbol{s} \cdot \boldsymbol{q})(\boldsymbol{s} \cdot \boldsymbol{p}) & 0 \\[2ex]
0 & 0 & \mu b_2(\boldsymbol{n} \cdot \boldsymbol{B}\boldsymbol{n}) + \boldsymbol{n} \cdot \boldsymbol{K}\boldsymbol{n}
\end{pmatrix} \tag{5.14}$$

where

$$\boldsymbol{q} \equiv \mathbb{E}[\boldsymbol{Q}]\boldsymbol{n} = \lambda(\boldsymbol{B} \cdot \boldsymbol{Q})\boldsymbol{B}\boldsymbol{n} + 2\mu\boldsymbol{B}\boldsymbol{Q}\boldsymbol{B}\boldsymbol{n},$$

$$\boldsymbol{p} \equiv \mathbb{E}[\boldsymbol{P}]\boldsymbol{n} = \lambda(\boldsymbol{B} \cdot \boldsymbol{P})\boldsymbol{B}\boldsymbol{n} + 2\mu\boldsymbol{B}\boldsymbol{P}\boldsymbol{B}\boldsymbol{n}, \tag{5.15}$$

and A_{nn}^e, A_{ss}^e, A_{ns}^e are the in-plane components of the elastic acoustic tensor $\boldsymbol{A}^e(\boldsymbol{n})$, namely

$$A_{nn}^e = (\lambda + 2\mu)(\boldsymbol{n} \cdot \boldsymbol{Bn})^2 + (\boldsymbol{n} \cdot \boldsymbol{Kn}),$$

$$A_{ss}^e = (\lambda + \mu)(\boldsymbol{s} \cdot \boldsymbol{Bn})^2 + \mu(\boldsymbol{n} \cdot \boldsymbol{Bn})(\boldsymbol{s} \cdot \boldsymbol{Bs}) + (\boldsymbol{n} \cdot \boldsymbol{Kn}), \qquad (5.16)$$

$$A_{ns}^e = (\lambda + 2\mu)(\boldsymbol{n} \cdot \boldsymbol{Bn})(\boldsymbol{s} \cdot \boldsymbol{Bn}),$$

It is evident from the matrix representation (5.14) that

$$A_{33}^{ep} = \mu b_2(\boldsymbol{n} \cdot \boldsymbol{Bn}) + \boldsymbol{n} \cdot \boldsymbol{Kn}, \qquad (5.17)$$

a quantity which we assume to be strictly positive, is the out-of-plane eigenvalue corresponding to a wave with out-of-plane amplitude ($\boldsymbol{g}$ proportional to $\boldsymbol{k}_3$).

Taking the trace and the determinant of the matrix obtained by deleting the third row and the third column in (5.14), we get the sum and the product of the two in-plane eigenvalues a_1^{ep} and a_2^{ep} corresponding to waves with in-plane amplitude ($\boldsymbol{g}$ lying in the plane spanned by $\boldsymbol{k}_1$ and $\boldsymbol{k}_2$),

$$a_1^{ep} + a_2^{ep} = A_{nn}^e + A_{ss}^e - \frac{1}{H}(f_1 - f_2),$$

$$a_1^{ep} a_2^{ep} = A_{nn}^e A_{ss}^e - (A_{ns}^e)^2 + \frac{1}{H}(A_{ns}^e f_3 - A_{ss}^e f_1 + A_{nn}^e f_2), \qquad (5.18)$$

where

$$f_1 = (\boldsymbol{n} \cdot \boldsymbol{q})(\boldsymbol{n} \cdot \boldsymbol{p}), \quad f_2 = -(\boldsymbol{s} \cdot \boldsymbol{q})(\boldsymbol{s} \cdot \boldsymbol{p}),$$
$$f_3 = (\boldsymbol{n} \cdot \boldsymbol{q})(\boldsymbol{s} \cdot \boldsymbol{p}) + (\boldsymbol{s} \cdot \boldsymbol{q})(\boldsymbol{n} \cdot \boldsymbol{p}). \qquad (5.19)$$

Thus, a necessary and sufficient condition for the existence of complex conjugate eigenvalues a_1^{ep} and a_2^{ep} is that the discriminant of the corresponding quadratic equation is not positive. It can be shown that this condition is equivalent to the three conditions

$$f_4 = (A_{nn}^e - A_{ss}^e)^2 \left[(f_1 + f_2 + 2ef_3)^2 - (1 + 4e^2)(f_1 - f_2)^2 \right] > 0,$$

$$f_5 = (A_{nn}^e - A_{ss}^e)(f_1 + f_2 + 2ef_3) > 0, \qquad (5.20)$$

$$\frac{f_5 - \sqrt{f_4}}{(A_{nn}^e - A_{ss}^e)^2 + 4(A_{ns}^e)^2} < H < \frac{f_5 + \sqrt{f_4}}{(A_{nn}^e - A_{ss}^e)^2 + 4(A_{ns}^e)^2},$$

where

$$e = \frac{A_{ns}^e}{A_{nn}^e - A_{ss}^e}. \tag{5.21}$$

With reference to Fig. 5.1, let θ_σ and θ_n be the angles of inclination of $\boldsymbol{b}$ and $\boldsymbol{n}$, respectively, with respect to the stress principal axes $\boldsymbol{k}_1$.
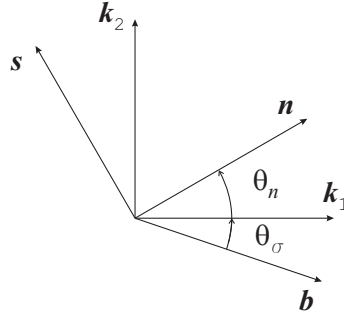
Figure 5.1: Principal stress axes $\boldsymbol{k}_1$ and $\boldsymbol{k}_2$, axis of elastic symmetry $\boldsymbol{b}$ and propagation direction $\boldsymbol{n}$.

We are now in a position to analyse the conditions to get complex conjugate in-plane eigenvalues of the acoustic tensor in terms of material parameters, stress, and orientation of the axis of elastic symmetry. The number of parameters in play can be reduced by one, normalizing all the quantities which have the dimension of stress in eqns. (5.14)-(5.20) through division by μ.

We summarize all these conditions as follows:

- Material parameters: elastic modulus λ/μ, anisotropy $\hat{b}$, pressure sensitivity ψ, and dilatancy χ.

- Principal stress values: σ_1/μ, σ_2/μ, σ_3/μ.

- Orientation of the axis of elastic symmetry: θ_σ.

For every set of values of all the above parameters, it is possible to study flutter for all the propagation directions $\boldsymbol{n}$ while varying the plastic modulus H/μ, by use of inequalities (5.20). Then we can visualise the ranges in which flutter occurs in the plane H/μ vs. θ_n. Restricting the analysis to the infinitesimal theory, that corresponds to identifying the flux (5.3) with the material time derivative $\dot{\boldsymbol{K}}$, the acoustic tensor $\boldsymbol{A}^{ep}(\boldsymbol{n})$ depends on the stress $\boldsymbol{K}$ only through $\boldsymbol{P}$ and $\boldsymbol{Q}$ and therefore it depends on the direction of $\boldsymbol{K}$ in

stress space, but not on its norm. The analysis has been performed for six plane stress states ($\sigma_3 = 0$), whose directions in the (σ_1/μ, σ_2/μ) plane are shown in Fig. 5.2.
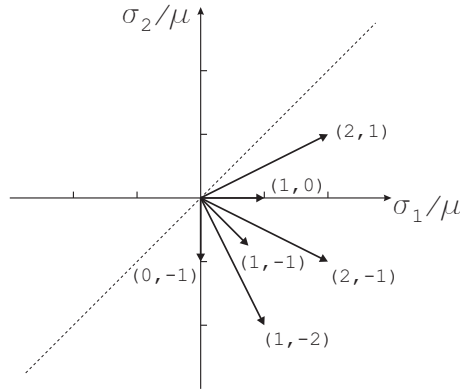
Figure 5.2: Stress directions in the σ_1/μ vs. σ_2/μ plane, for which the analysis has been performed.

The results are reported in Figs. 5.3–5.8. The ranges of flutter instability are shown in Figs. 5.3 and 5.4, in which parameters λ/μ, $\hat{b}$, ψ, and χ are kept constant and equal to 1, 80°, 30°, and 0°, respectively, while parameter θ_σ ranges between 0° and 90°. Flutter occurs for the points inside the closed curves. Figures 5.5 and 5.6 show the same analysis as before, except that now parameter $\hat{b}$ is equal to 10°. Figures 5.7 and 5.8 refer again to $\hat{b} = 80°$, but in this case the material has dilatancy different from zero, namely $\chi = 15°$.

From the above analysis it can be deduced that this model permits one to approach flutter starting from a well-behaved state. For instance, let us consider the case shown in Fig. 5.9, in which the material is subject to uniaxial traction, $\sigma_1/\mu = 1$, $\sigma_2/\mu = 0$, and the direction of the axis of elastic symmetry is inclined at $\theta_\sigma = 15°$ with respect to the stress principal direction $\boldsymbol{k}_1$. The material parameters are $\lambda/\mu = 1$, $\hat{b} = 80°$, $\psi = 30°$, and $\chi = 0°$. It is clear that we can start from a condition in which, say, $H/\mu = 2$ and therefore flutter is excluded for all directions of propagation, and then approach flutter decreasing the plastic modulus H/μ until we get the apex of the curve at $H/\mu \approx 1.229$ and the onset of flutter occur for a particular direction of propagation, namely $\theta_n \approx -14.56°$.
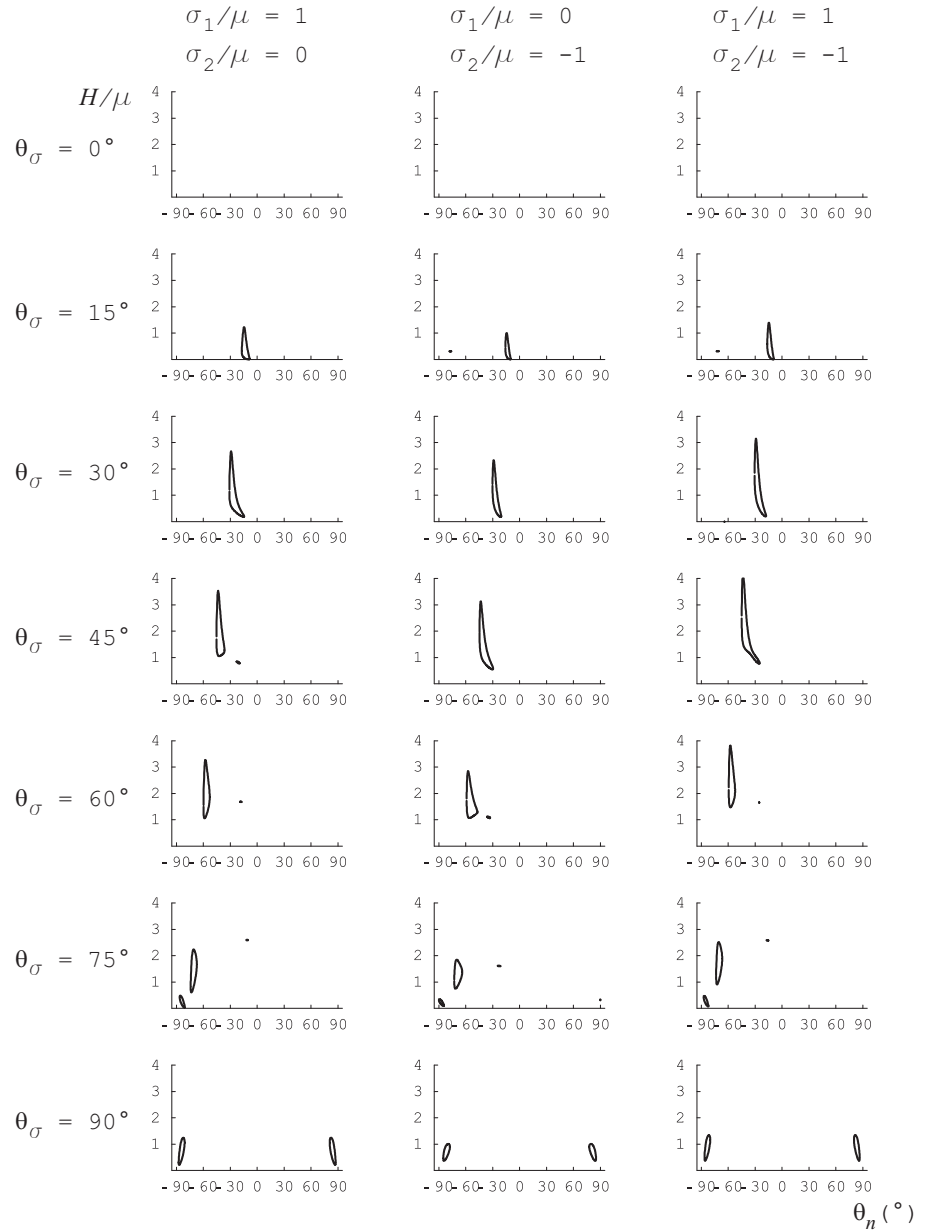
Figure 5.3: Ranges of flutter instability in the H/μ vs. θ_n plane, for some plane stress states and orientations of the axis of elastic symmetry. Flutter occurs for the points inside the closed curves. Material parameters: $\lambda/\mu = 1$, $\hat{b} = 80°$, $\psi = 30°$, and $\chi = 0°$.
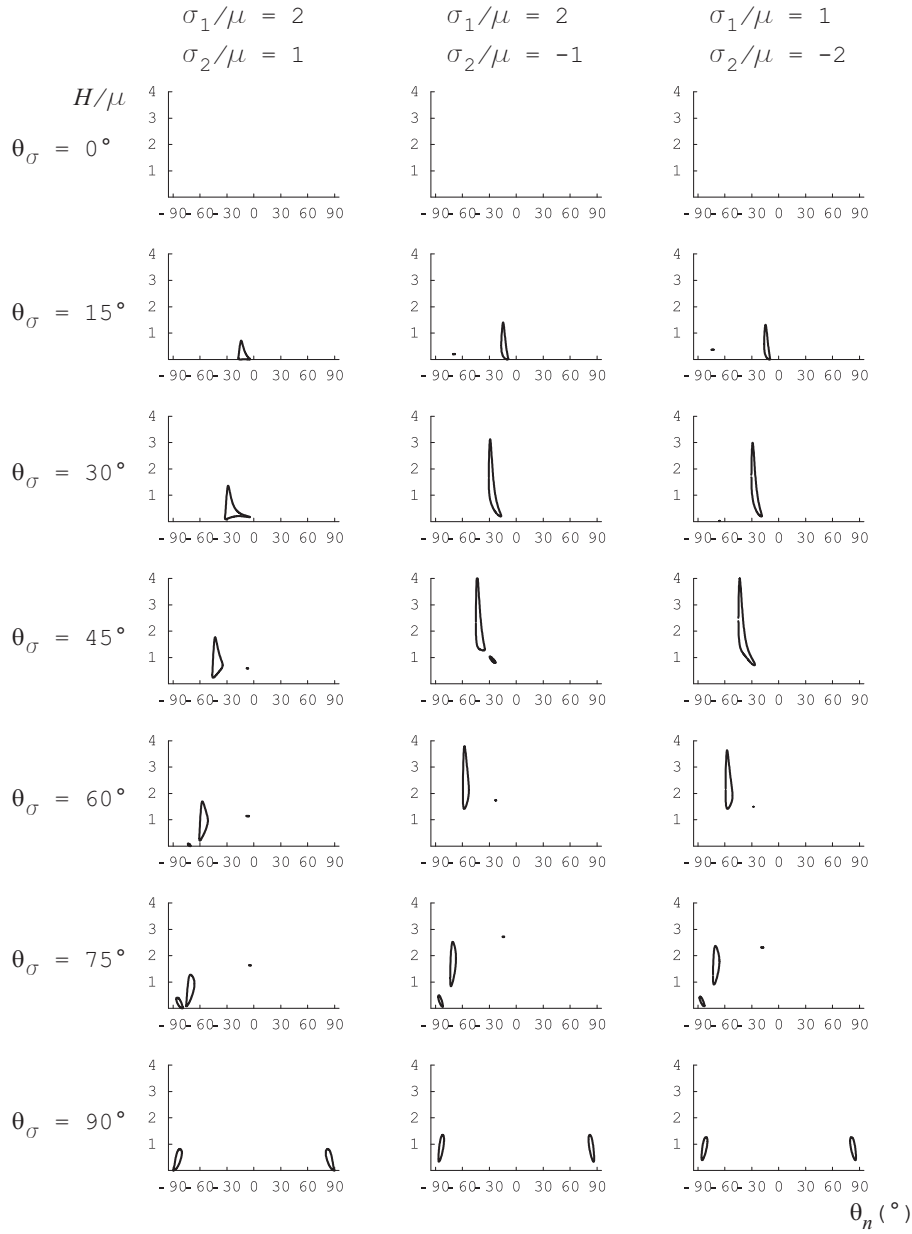
Figure 5.4: Ranges of flutter instability in the H/μ vs. θ_n plane, for some plane stress states and orientations of the axis of elastic symmetry. Flutter occurs for the points inside the closed curves. Material parameters: $\lambda/\mu = 1$, $\hat{b} = 80°$, $\psi = 30°$, and $\chi = 0°$.
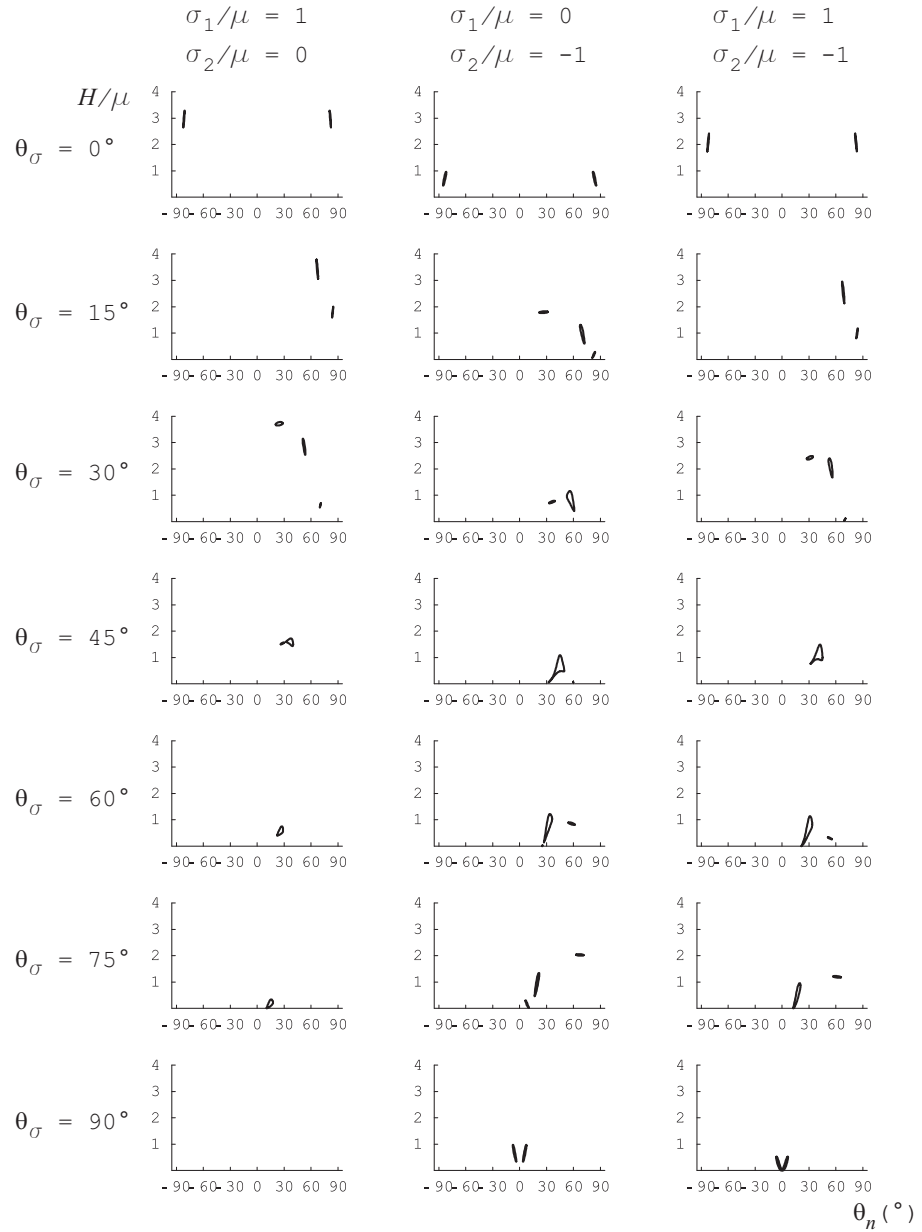
Figure 5.5: Ranges of flutter instability in the H/μ vs. θ_n plane, for some plane stress states and orientations of the axis of elastic symmetry. Flutter occurs for the points inside the closed curves. Material parameters: $\lambda/\mu = 1$, $\hat{b} = 10°$, $\psi = 30°$, and $\chi = 0°$.
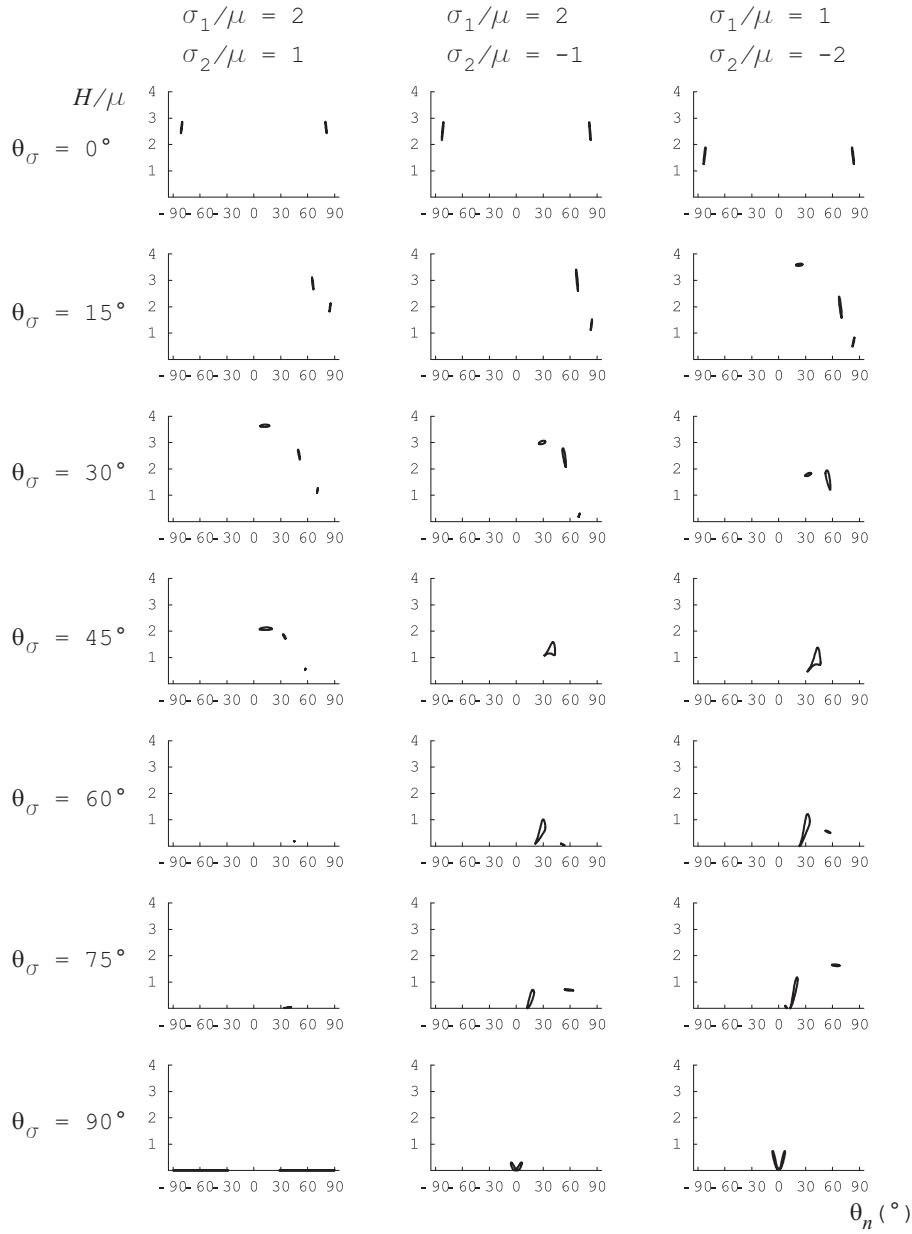
Figure 5.6: Ranges of flutter instability in the H/μ vs. θ_n plane, for some plane stress states and orientations of the axis of elastic symmetry. Flutter occurs for the points inside the closed curves. Material parameters: $\lambda/\mu = 1$, $\hat{b} = 10°$, $\psi = 30°$, and $\chi = 0°$.
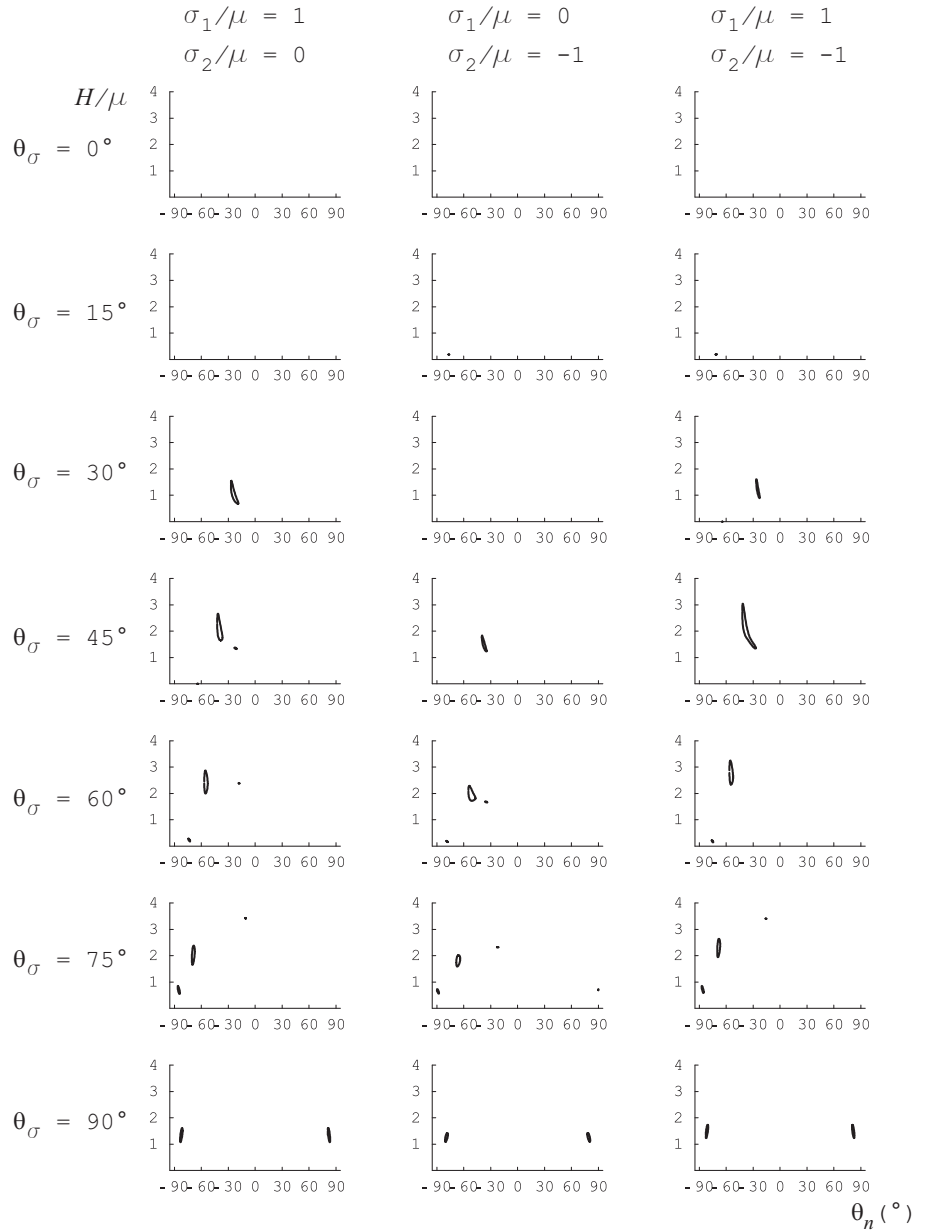
Figure 5.7: Ranges of flutter instability in the H/μ vs. θ_n plane, for some plane stress states and orientations of the axis of elastic symmetry. Flutter occurs for the points inside the closed curves. Material parameters: $\lambda/\mu = 1$, $\hat{b} = 80°$, $\psi = 30°$, and $\chi = 15°$.
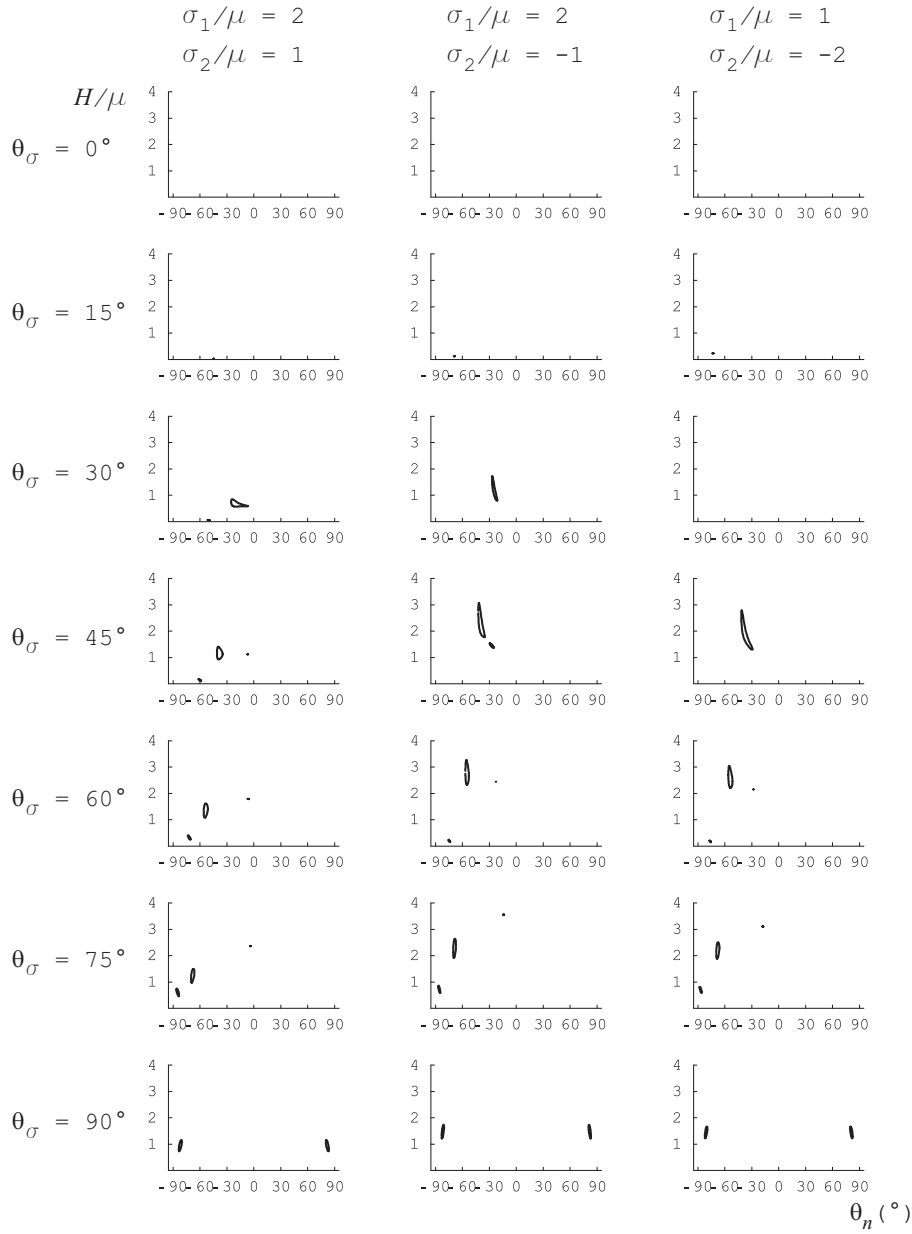
Figure 5.8: Ranges of flutter instability in the H/μ vs. θ_n plane, for some plane stress states and orientations of the axis of elastic symmetry. Flutter occurs for the points inside the closed curves. Material parameters: $\lambda/\mu = 1$, $\hat{b} = 80°$, $\psi = 30°$, and $\chi = 15°$.
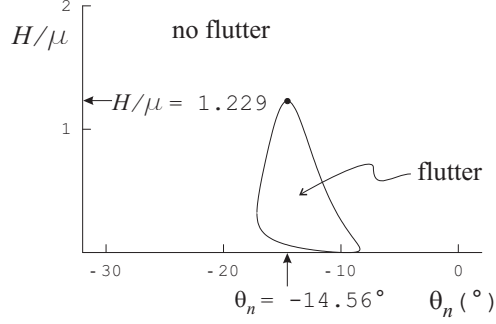
Figure 5.9: Range of flutter instability in the H/μ vs. θ_n plane, for uniaxial tension $\sigma_1/\mu = 1$, $\sigma_2/\mu = 0$ and $\theta_\sigma = 15°$. Flutter occurs for the points inside the closed curves. Material parameters: $\lambda/\mu = 1$, $\hat{b} = 80°$, $\psi = 30°$, and $\chi = 0°$.

5.3.1   Spectral analysis of the acoustic tensor

Let us now turn our attention to the eigenvectors of the acoustic tensor $\boldsymbol{A}^{ep}$ in order to obtain the spectral representation. It can be noted that A_{33}^{ep} and $\boldsymbol{k}_3$ are the out-of-plane eigenvalue and unit eigenvector, respectively, so that we can focus our attention only on the in-plane eigenvalues and eigenvectors, and the problem is reduced to the study of the eigensystem of the tensor

$$\boldsymbol{A} = A_{11}^{ep}(\boldsymbol{k}_1 \otimes \boldsymbol{k}_1) + A_{12}^{ep}(\boldsymbol{k}_1 \otimes \boldsymbol{k}_2) + A_{21}^{ep}(\boldsymbol{k}_2 \otimes \boldsymbol{k}_1) + A_{22}^{ep}(\boldsymbol{k}_2 \otimes \boldsymbol{k}_2), \quad (5.22)$$

where, without loss of generality, we can take $\boldsymbol{k}_1, \boldsymbol{k}_2 \in \mathbf{R}^2$. The eigenvalues are

$$a_{1,2}^{ep} = \frac{A_{11}^{ep} + A_{22}^{ep} \pm \Delta}{2}, \qquad (5.23)$$

where

$$\Delta = \left[(A_{11}^{ep} - A_{22}^{ep})^2 + 4A_{12}^{ep}A_{21}^{ep}\right]^{1/2}. \qquad (5.24)$$

Assuming that the eigenvalues are real and distinct the spectral representation of $\boldsymbol{A}$ is

$$\boldsymbol{A} = a_1^{ep}(\boldsymbol{v}_1 \otimes \boldsymbol{w}_1) + a_2^{ep}(\boldsymbol{v}_2 \otimes \boldsymbol{w}_2), \qquad (5.25)$$

where $\{\boldsymbol{v}_1, \boldsymbol{v}_2\}$ and $\{\boldsymbol{w}_1, \boldsymbol{w}_2\}$ are dual bases, i.e. satisfying $\boldsymbol{v}_i \cdot \boldsymbol{w}_j = \delta_{ij}$ (i,j = 1,2), composed of right eigenvectors and left eigenvectors, respectively. This

basis may be calculated from

$$
\begin{aligned}
\boldsymbol{v}_1 &= \boldsymbol{k}_1 + \frac{\Delta - (A_{11}^{ep} - A_{22}^{ep})}{2A_{12}^{ep}} \boldsymbol{k}_2, \\[2mm]
\boldsymbol{v}_2 &= \boldsymbol{k}_1 + \frac{-\Delta - (A_{11}^{ep} - A_{22}^{ep})}{2A_{12}^{ep}} \boldsymbol{k}_2, \\[2mm]
\boldsymbol{w}_1 &= \frac{\Delta + (A_{11}^{ep} - A_{22}^{ep})}{2\Delta} \boldsymbol{k}_1 + \frac{A_{12}^{ep}}{\Delta} \boldsymbol{k}_2, \\[2mm]
\boldsymbol{w}_2 &= \frac{\Delta - (A_{11}^{ep} - A_{22}^{ep})}{2\Delta} \boldsymbol{k}_1 - \frac{A_{12}^{ep}}{\Delta} \boldsymbol{k}_2,
\end{aligned}
\tag{5.26}
$$

which hold for $A_{12}^{ep} \neq 0$, or from

$$
\begin{aligned}
\boldsymbol{v}_1 &= \frac{\Delta + (A_{11}^{ep} - A_{22}^{ep})}{2A_{21}^{ep}} \boldsymbol{k}_1 + \boldsymbol{k}_2, \\[2mm]
\boldsymbol{v}_2 &= \frac{-\Delta + (A_{11}^{ep} - A_{22}^{ep})}{2A_{21}^{ep}} \boldsymbol{k}_1 + \boldsymbol{k}_2, \\[2mm]
\boldsymbol{w}_1 &= \frac{A_{21}^{ep}}{\Delta} \boldsymbol{k}_1 + \frac{\Delta - (A_{11}^{ep} - A_{22}^{ep})}{2\Delta} \boldsymbol{k}_2, \\[2mm]
\boldsymbol{w}_2 &= -\frac{A_{21}^{ep}}{\Delta} \boldsymbol{k}_1 + \frac{\Delta + (A_{11}^{ep} - A_{22}^{ep})}{2\Delta} \boldsymbol{k}_2,
\end{aligned}
\tag{5.27}
$$

which hold for $A_{21}^{ep} \neq 0$, or from

$$
\begin{aligned}
\boldsymbol{v}_1 &= \boldsymbol{k}_1 + \frac{\Delta - (A_{11}^{ep} - A_{22}^{ep})}{2A_{12}^{ep}} \boldsymbol{k}_2, \\[2mm]
\boldsymbol{v}_2 &= \frac{-\Delta + (A_{11}^{ep} - A_{22}^{ep})}{2A_{21}^{ep}} \boldsymbol{k}_1 + \boldsymbol{k}_2, \\[2mm]
\boldsymbol{w}_1 &= \frac{\Delta + (A_{11}^{ep} - A_{22}^{ep})}{2\Delta} \boldsymbol{k}_1 + \frac{A_{12}^{ep}}{\Delta} \boldsymbol{k}_2, \\[2mm]
\boldsymbol{w}_2 &= -\frac{A_{21}^{ep}}{\Delta} \boldsymbol{k}_1 + \frac{\Delta + (A_{11}^{ep} - A_{22}^{ep})}{2\Delta} \boldsymbol{k}_2,
\end{aligned}
\tag{5.28}
$$

which hold for $A_{12}^{ep} \neq 0$ and $A_{21}^{ep} \neq 0$.

Therefore, assuming $a_1^{ep} \neq 0$ and $a_2^{ep} \neq 0$, the inverse of $\boldsymbol{A}$ is

$$
\boldsymbol{A}^{-1} = \frac{1}{a_1^{ep}}(\boldsymbol{v}_1 \otimes \boldsymbol{w}_1) + \frac{1}{a_2^{ep}}(\boldsymbol{v}_2 \otimes \boldsymbol{w}_2).
\tag{5.29}
$$

For $\Delta \to 0$ (coalescence of the eigenvalues), the tensor $\boldsymbol{A}$ becomes defective (apart from the trivial case where $\boldsymbol{A}$ is isotropic) and each term in the spectral representation of $\boldsymbol{A}$, and also of $\boldsymbol{A}^{-1}$, blows up but $\boldsymbol{A}^{-1}$ continues to exist and to be defined correctly. Indeed a substitution of eqns. (5.23) and (5.26) (or (5.27), or (5.28)) into eqn. (5.29) leads to

$$\boldsymbol{A}^{-1} = \frac{1}{A_{11}^{ep}A_{22}^{ep} - A_{12}^{ep}A_{12}^{ep}} \left[A_{22}^{ep}(\boldsymbol{k}_1 \otimes \boldsymbol{k}_1) - A_{12}^{ep}(\boldsymbol{k}_1 \otimes \boldsymbol{k}_2) \right. \tag{5.30}$$
$$\left. - A_{21}^{ep}(\boldsymbol{k}_2 \otimes \boldsymbol{k}_1) + A_{11}^{ep}(\boldsymbol{k}_2 \otimes \boldsymbol{k}_2) \right].$$

5.4 Dynamic Green's function for the time-harmonic case

We consider an initial static deformation, $\boldsymbol{x} = \chi(\boldsymbol{\xi})$, of a homogeneous body Ω_0, which satisfies:

$$S_{ij,j} = 0, \quad \boldsymbol{\xi} \in \Omega_0. \tag{5.31}$$

(in fact we will take S_{ij} to be uniform, that is constant over Ω_0), and then we perform a dynamic perturbation of the form:

$$S_{ij} \to S_{ij} + \delta S_{ij}(\boldsymbol{\xi}, t),$$
$$\tag{5.32}$$
$$x_i(\boldsymbol{\xi}) \to x_i(\boldsymbol{\xi}) + \delta x_i(\boldsymbol{\xi}, t),$$

Now we can write the incremental constitutive equations (5.5)–(5.6) in the form:

$$\delta S_{ij} = \mathbb{C}_{ijkl}\delta x_{k,l}, \quad \boldsymbol{\xi} \in \Omega_0, \ t \in I, \tag{5.33}$$

where the operator δ is used to denote an incremental quantity, instead of the superscript dot. The equations of motion for the considered dynamic perturbation are:

$$(S_{ij} + \delta S_{ij})_{,j} + f_i = \rho_0(\ddot{x}_i + \delta\ddot{x}_i), \quad \boldsymbol{\xi} \in \Omega_0, \ t \in I, \tag{5.34}$$

which, in view of the fact that S_{ij} is uniform and the initial deformation x_i is static, simplify to:

$$\delta S_{ij,j} + f_i = \rho_0\delta\ddot{x}_i, \quad \boldsymbol{\xi} \in \Omega_0, \ t \in I. \tag{5.35}$$

Combining (5.33) and (5.34) we get the equation of motion in the form:

$$(\mathbb{C}_{ijkl}\delta x_{k,l})_{,j} + f_i = \rho_0\delta\ddot{x}_i, \quad \boldsymbol{\xi} \in \Omega_0, \ t \in I. \tag{5.36}$$

For a homogeneus body $\mathbb{C}_{ijkl}$ are constant, then (5.36) reduces to:

$$\mathbb{C}_{ijkl}u_{k,lj} + f_i = \rho_0\ddot{u}_i, \quad \boldsymbol{\xi} \in \Omega_0, \ t \in I, \tag{5.37}$$

writing u_i for δx_i.

Equations (5.36) and (5.37) look like ordinary elastodynamics, except that $\mathbb{C}_{ijkl}$ does not have the symmetries usually assumed. The basic question now is to investigate the properties of eqn. (5.37), close to the flutter condition. The approach adopted here is to find the dynamic Green's function. Limiting the analysis to the time-harmonic case,

$$u_i = \hat{u}_i(\boldsymbol{\xi})e^{-i\omega t}, \quad f_i = \hat{f}_i(\boldsymbol{\xi})e^{-i\omega t},$$

we can remove the time dependence from eqn. (5.37) and get it in the form:

$$\mathbb{C}_{ijkl}\hat{u}_{k,lj} + \rho_0\omega^2\hat{u}_i + \hat{f}_i = 0, \quad \boldsymbol{\xi} \in \Omega_0. \tag{5.38}$$

The Green's tensor $\hat{u}_i = G_{ip}(\boldsymbol{\xi})$ corresponds to choosing $\hat{f}_i = \delta_{ip}\delta(\boldsymbol{\xi})$, thus we obtain

$$\mathbb{C}_{ijkl}G_{kp,lj}(\boldsymbol{\xi}) + \rho_0\omega^2 G_{ip}(\boldsymbol{\xi}) + \delta_{ip}\delta(\boldsymbol{\xi}) = 0, \quad \boldsymbol{\xi} \in \Omega_0. \tag{5.39}$$

It is possible now to employ an updated Lagrangian formulation so that the reference state is the deformed state. Then writing $\boldsymbol{x}$ instead of $\boldsymbol{\xi}$:

$$\mathbb{C}_{ijkl}G_{kp,lj}(\boldsymbol{x}) + \rho_0\omega^2 G_{ip}(\boldsymbol{x}) + \delta_{ip}\delta(\boldsymbol{x}) = 0, \quad \boldsymbol{x} \in \Omega. \tag{5.40}$$

5.4.1 Plane wave expansion of the delta function

In order to approach the flutter condition, we exploit the analysis of the acoustic tensor developed for the planar problem in Section 5.3, considering an infinite medium subject to plane strain conditions,

$$\begin{cases} G_{1p} = G_{1p}(x_1, x_2), \\ G_{2p} = G_{2p}(x_1, x_2), \\ G_{3p} = 0, \end{cases} \tag{5.41}$$

so that i, j, k, l, p in eqn. (5.40) range now between 1 and 2, and $\boldsymbol{x} \in \mathbf{R}^2$.

The plane wave expansion of the δ function is:

$$\delta(\boldsymbol{x}) = -\frac{1}{4\pi^2}\int_{|\boldsymbol{n}|=1}\frac{1}{(\boldsymbol{n}\cdot\boldsymbol{x})^2}ds, \tag{5.42}$$

where $\boldsymbol{n}$ is the unit vector, so that defining the analogous transform $\tilde{\boldsymbol{G}}(\boldsymbol{n} \cdot \boldsymbol{x})$ of the Green tensor $\boldsymbol{G}(\boldsymbol{x})$ as

$$\boldsymbol{G}(\boldsymbol{x}) = -\frac{1}{4\pi^2} \int_{|\boldsymbol{n}|=1} \tilde{\boldsymbol{G}}(\boldsymbol{n} \cdot \boldsymbol{x}) ds, \qquad (5.43)$$

the transform of eqn. (5.40) leads to

$$\mathbb{C}_{ijkl} n_j n_l \tilde{G}''_{kp}(\xi) + \rho_0 \omega^2 \tilde{G}_{ip}(\xi) + \frac{\delta_{ip}}{\xi^2} = 0, \qquad (5.44)$$

where $\xi = \boldsymbol{n} \cdot \boldsymbol{x}$. In this equation the acoustic tensor can be easily recognized, $A_{ik} = \mathbb{C}_{ijkl} n_j n_l$, so that we get

$$\boldsymbol{A}(\boldsymbol{n}) \tilde{\boldsymbol{G}}''(\xi) + \rho_0 \omega^2 \tilde{\boldsymbol{G}}(\xi) + \frac{1}{\xi^2} \boldsymbol{I} = 0. \qquad (5.45)$$

Let us assume that $\boldsymbol{A}(\boldsymbol{n})$ has two real, distinct, positive eigenvalues $\rho_0 c_N^2$ and left and right eigenvectors $\boldsymbol{w}_N$, $\boldsymbol{v}_N$, $(N = 1, 2)$. We can choose the vectors $\boldsymbol{w}_N$, $\boldsymbol{v}_N$ as dual basis vectors, i.e. $\boldsymbol{v}_N \cdot \boldsymbol{w}_M = \delta_{NM}$, $(N, M = 1, 2)$. The spectral representations of $\boldsymbol{A}(\boldsymbol{n})$ and $\boldsymbol{I}$ are therefore

$$\boldsymbol{A}(\boldsymbol{n}) = \sum_{N=1}^{2} \rho_0 c_N^2 \boldsymbol{v}_N \otimes \boldsymbol{w}_N \quad \text{and} \quad \boldsymbol{I} = \sum_{N=1}^{2} \boldsymbol{v}_N \otimes \boldsymbol{w}_N, \qquad (5.46)$$

respectively. Writing now

$$\tilde{\boldsymbol{G}}(\xi) = \sum_{N=1}^{2} \phi_N(\xi) \boldsymbol{v}_N \otimes \boldsymbol{w}_N, \qquad (5.47)$$

we get eqn. (5.45) in the form

$$\sum_{N=1}^{2} \left(\rho_0 c_N^2 \phi_N'' + \rho_0 \omega^2 \phi_N + \frac{1}{\xi^2} \right) \boldsymbol{v}_N \otimes \boldsymbol{w}_N = 0, \qquad (5.48)$$

which is equivalent to the following uncoupled system of two equations,

$$\phi_N'' + k_N^2 \phi_N + \frac{1}{\rho_0 c_N^2} \frac{1}{\xi^2} = 0, \quad N = 1, 2 \qquad (5.49)$$

where $k_N = \omega / c_N$.

The sole phisically meaningful solution of the ordinary differential equation (5.49) is obtained by imposing the radiation condition, which states that the solution should consist only of waves propagating away from the source, the so-called outgoing waves. Since we have chosen the harmonic time dependence to be of the form $e^{-i\omega t}$, the outgoing wave solution of (5.49) in the ξ coordinate is:

$$\phi_N(\xi) = \frac{1}{2\rho_0 c_N^2} \left[2 \operatorname{Ci}(k_N |\xi|) \cos(k_N \xi) \right. \tag{5.50}$$

$$\left. + 2 \operatorname{Si}(k_N \xi) \sin(k_N \xi) - i\pi \cos(k_N \xi) \right],$$

where

$$\operatorname{Ci}(x) = -\int_x^{+\infty} \frac{\cos t}{t} dt, \quad x > 0 \quad \text{and} \quad \operatorname{Si}(x) = \int_0^x \frac{\sin t}{t} dt$$

are the cosine and sine integral functions, respectively. Finally, the antitransform of eqn. (5.47) coupled with eqn. (5.50) leads to

$$\boldsymbol{G}(\boldsymbol{x}) = -\frac{1}{8\pi^2} \sum_{N=1}^{2} \int_{|\boldsymbol{n}|=1} \left[2 \cos(k_N \boldsymbol{n} \cdot \boldsymbol{x}) \operatorname{Ci}(k_N |\boldsymbol{n} \cdot \boldsymbol{x}|) \right. \tag{5.51}$$

$$\left. + 2 \sin(k_N \boldsymbol{n} \cdot \boldsymbol{x}) \operatorname{Si}(k_N \boldsymbol{n} \cdot \boldsymbol{x}) - i\pi \cos(k_N \boldsymbol{n} \cdot \boldsymbol{x}) \right] \frac{\boldsymbol{v}_N \otimes \boldsymbol{w}_N}{\rho_0 c_N^2} ds.$$

5.4.2 Radon transform

In this section we obtain the Green's function following a different approach, namely the Radon transform technique. The Radon transform of a function $f(\boldsymbol{x})$, $\boldsymbol{x} \in \mathbf{R}^2$ is defined as

$$\mathcal{R}\left[f(\boldsymbol{x})\right] = \hat{f}(p, \boldsymbol{n}) = \int_{\mathbf{R}^2} f(\boldsymbol{x})\delta(p - \boldsymbol{n} \cdot \boldsymbol{x}) \, d\boldsymbol{x}, \quad p \in \mathbf{R}, \ \boldsymbol{n} \in \mathbf{R}^2 \tag{5.52}$$

with the inverse

$$f(\boldsymbol{x}) = \frac{1}{4\pi^2} \int_{|\boldsymbol{n}|=1} \text{P.V.} \int_{-\infty}^{+\infty} \frac{\hat{f}_p(p, \boldsymbol{n})}{(\boldsymbol{n} \cdot \boldsymbol{x} - p)} \, dp \, ds, \tag{5.53}$$

where the notation with a subscript variable denotes partial differentiation with respect to that variable:

$$\hat{f}_p(p, \boldsymbol{n}) = \frac{\partial \hat{f}(p, \boldsymbol{n})}{\partial p}. \tag{5.54}$$

We will make use of the following properties of the Radon transform:

- linearity

$$\mathcal{R}\left[c_1 f_1(\boldsymbol{x}) + c_2 f_2(\boldsymbol{x})\right] = c_1 \mathcal{R}\left[f_1(\boldsymbol{x})\right] + c_2 \mathcal{R}\left[f_2(\boldsymbol{x})\right], \tag{5.55}$$

- derivative transform

$$\begin{aligned}
\mathcal{R}\left[f_{,j}(\boldsymbol{x})\right] &= n_j \hat{f}_p(p, \boldsymbol{n}), \\
\mathcal{R}\left[f_{,lj}(\boldsymbol{x})\right] &= n_l n_j \hat{f}_{pp}(p, \boldsymbol{n}),
\end{aligned} \tag{5.56}$$

- transform of the two-dimensional Dirac delta function

$$\mathcal{R}\left[\delta(\boldsymbol{x})\right] = \delta(p). \tag{5.57}$$

The Radon transform of eqn. (5.40) is therefore

$$\mathbb{C}_{ijkl} n_l n_j \hat{G}''_{kp}(p, \boldsymbol{n}) + \rho_0 \omega^2 \hat{G}_{ip}(p, \boldsymbol{n}) + \delta_{ip}\delta(p) = 0, \tag{5.58}$$

where

$$\hat{G}''_{kp}(p, \boldsymbol{n}) = \frac{\partial^2}{\partial p^2} \hat{G}_{kp}(p, \boldsymbol{n}). \tag{5.59}$$

Eqn. (5.58) can be rewrite in matrix form as

$$\boldsymbol{A}(\boldsymbol{n})\hat{\boldsymbol{G}}''(p, \boldsymbol{n}) + \rho_0 \omega^2 \hat{\boldsymbol{G}}(p, \boldsymbol{n}) + \delta(p)\boldsymbol{I} = 0. \tag{5.60}$$

Now, using the spectral representations of $\boldsymbol{A}(\boldsymbol{n})$ and $\boldsymbol{I}$ in eqns. (5.46) and writing

$$\hat{\boldsymbol{G}}(p, \boldsymbol{n}) = \sum_{N=1}^{2} \phi_N(p, \boldsymbol{n}) \boldsymbol{v}_N \otimes \boldsymbol{w}_N, \tag{5.61}$$

we get

$$\sum_{N=1}^{2} \left[\rho_0 c_N^2 \phi''_N + \rho_0 \omega^2 \phi_N + \delta(p)\right] \boldsymbol{v}_N \otimes \boldsymbol{w}_N = 0, \tag{5.62}$$

which is equivalent to the following uncoupled system of two equations,

$$\phi''_N + k_N^2 \phi_N + \frac{1}{\rho_0 c_N^2}\delta(p) = 0, \quad N = 1, 2. \tag{5.63}$$

Since we have chosen the harmonic time dependence to be of the form $e^{-i\omega t}$, the outgoing wave solution of (5.63) in the p coordinate is:

$$\phi_N(p, \boldsymbol{n}) = -\frac{e^{ik_N|p|}}{2\rho_0 i k_N c_N^2}, \tag{5.64}$$

so that

$$\hat{\boldsymbol{G}}(p, \boldsymbol{n}) = -\sum_{N=1}^{2} \frac{e^{ik_N|p|}}{2\rho_0 ik_N c_N^2} \boldsymbol{v}_N \otimes \boldsymbol{w}_N. \tag{5.65}$$

and

$$\hat{\boldsymbol{G}}_p(p, \boldsymbol{n}) = -\sum_{N=1}^{2} \frac{\text{sgn}(p)e^{ik_N|p|}}{2\rho_0 c_N^2} \boldsymbol{v}_N \otimes \boldsymbol{w}_N. \tag{5.66}$$

The antitransform of equation (5.65) leads to

$$\boldsymbol{G}(\boldsymbol{x}) = -\frac{1}{4\pi^2} \sum_{N=1}^{2} \int_{|\boldsymbol{n}|=1} \int_{-\infty}^{+\infty} \frac{\text{sgn}(p)e^{ik_N|p|}}{2\rho_0 c_N^2 (\boldsymbol{n} \cdot \boldsymbol{x} - p)} \boldsymbol{v}_N \otimes \boldsymbol{w}_N \, dp \, ds. \tag{5.67}$$

The integral in the variable p can be evaluated splitting the domain as follows

$$\int_{-\infty}^{+\infty} \frac{\text{sgn}(p)e^{ik_N|p|}}{\xi - p} \, dp = -\int_{-\infty}^{0} \frac{e^{-ik_N p}}{\xi - p} \, dp + \int_{0}^{+\infty} \frac{e^{ik_N p}}{\xi - p} \, dp, \tag{5.68}$$

so that we can treat the two integrals separately, namely

$$-\int_{-\infty}^{0} \frac{e^{-ik_N p}}{\xi - p} \, dp = -e^{-ik_N \xi} \int_{k_N \xi}^{+\infty} \frac{e^{iq}}{q} \, dq, \tag{5.69}$$

where we have made the substitution $q = k_N(\xi - p)$, and

$$\int_{0}^{+\infty} \frac{e^{ik_N p}}{\xi - p} \, dp = -e^{ik_N \xi} \int_{-k_N \xi}^{+\infty} \frac{e^{iq}}{q} \, dq, \tag{5.70}$$

where we have made the substitution $q = k_N(p - \xi)$. Finally, the expansion of the exponential function,

$$e^{iq} = \cos q + i \sin q,$$

allows us to conclude and get the Green's function in the form

$$\boldsymbol{G}(\boldsymbol{x}) = -\frac{1}{8\pi^2} \sum_{N=1}^{2} \int_{|\boldsymbol{n}|=1} [2 \cos(k_N \boldsymbol{n} \cdot \boldsymbol{x}) \, \text{Ci}(k_N |\boldsymbol{n} \cdot \boldsymbol{x}|) \tag{5.71}$$

$$+ 2 \sin(k_N \boldsymbol{n} \cdot \boldsymbol{x}) \, \text{Si}(k_N \boldsymbol{n} \cdot \boldsymbol{x}) - i\pi \cos(k_N \boldsymbol{n} \cdot \boldsymbol{x})] \frac{\boldsymbol{v}_N \otimes \boldsymbol{w}_N}{\rho_0 c_N^2} ds.$$

5.4.3 Convergence of the Green's function

It can be noted that $\cos(\cdot)$ and $\sin(\cdot)\,\mathrm{Si}(\cdot)$ are even functions, so that we can write

$$\boldsymbol{G}(\boldsymbol{x}) = -\frac{1}{8\pi^2} \sum_{N=1}^{2} \int_{|\boldsymbol{n}|=1} [2\cos(k_N|\boldsymbol{n}\cdot\boldsymbol{x}|)\,\mathrm{Ci}(k_N|\boldsymbol{n}\cdot\boldsymbol{x}|) \tag{5.72}$$

$$+\, 2\sin(k_N|\boldsymbol{n}\cdot\boldsymbol{x}|)\,\mathrm{Si}(k_N|\boldsymbol{n}\cdot\boldsymbol{x}|) - i\,\pi\cos(k_N|\boldsymbol{n}\cdot\boldsymbol{x}|)] \frac{\boldsymbol{v}_N \otimes \boldsymbol{w}_N}{\rho_0 c_N^2} ds.$$

which may be expanded to yield

$$\boldsymbol{G}(\boldsymbol{x}) = -\frac{1}{8\pi^2} \sum_{N=1}^{2} \int_0^{2\pi} [2\cos(rk_N|\cos\alpha|)\,\mathrm{Ci}(rk_N|\cos\alpha|) \tag{5.73}$$

$$+\, 2\sin(rk_N|\cos\alpha|)\,\mathrm{Si}(rk_N|\cos\alpha|) - i\,\pi\cos(rk_N|\cos\alpha|)] \frac{\boldsymbol{v}_N \otimes \boldsymbol{w}_N}{\rho_0 c_N^2} d\alpha,$$

where the distance $r = |\boldsymbol{x}|$ and the angle θ are polar coordinates, α is the angle between the two vectors $\boldsymbol{x}$ and $\boldsymbol{n}$. It is easy to show that the integrand is a periodic function with period π. The function $|\cos\alpha|$ is a periodic function with period π,

$$|\cos(\alpha + n\pi)| = |(-1)^n\cos\alpha| = |\cos\alpha|. \tag{5.74}$$

The functions $c_N(\alpha)$, $k_N(\alpha)$, $\boldsymbol{v}_N(\alpha)$, and $\boldsymbol{w}_N(\alpha)$ are periodic functions with period π, since the acoustic tensor itself is a periodic function with period π,

$$A_{ik} = \mathbb{C}_{ijkl}n_j n_l \tag{5.75}$$

$$= \phi_{ik}(n_1^2, n_2^2, n_1 n_2) \tag{5.76}$$

$$= \phi_{ik}(\cos^2(\alpha + \theta), \sin^2(\alpha + \theta), \cos(\alpha + \theta)\sin(\alpha + \theta)) \tag{5.77}$$

$$= \tilde{\phi}_{ik}(\cos[2(\alpha + \theta)], \sin[2(\alpha + \theta)]). \tag{5.78}$$

So that

$$\boldsymbol{G}(\boldsymbol{x}) = -\frac{1}{4\pi^2} \sum_{N=1}^{2} \int_0^{\pi} [2\cos(rk_N|\cos\alpha|)\,\mathrm{Ci}(rk_N|\cos\alpha|) \tag{5.79}$$

$$+\, 2\sin(rk_N|\cos\alpha|)\,\mathrm{Si}(rk_N|\cos\alpha|) - i\,\pi\cos(rk_N|\cos\alpha|)] \frac{\boldsymbol{v}_N \otimes \boldsymbol{w}_N}{\rho_0 c_N^2} d\alpha.$$

It can be noted that the integrand has a singularity at $\alpha = \pi/2$, in fact

$$\text{Ci}(0+) = -\infty. \tag{5.80}$$

Since all the other quantities in the integrand are limited, we can restrict our attention to

$$\int_0^\pi \text{Ci}(rk_N|\cos\alpha|)\,d\alpha. \tag{5.81}$$

The singularity can be analyzed using the formula

$$\text{Ci}(x) = \gamma + \log x - \int_0^x \frac{1-\cos t}{t}\,dt, \tag{5.82}$$

where γ is the Euler's constant. This formula leads us to the study of

$$\int_0^\pi \log|\cos\alpha|\,d\alpha, \tag{5.83}$$

which may easily be shown to converge, indeed

$$\int_0^\pi \log|\cos\alpha|\,d\alpha = 2\int_0^{\pi/2} \log(\cos\alpha)\,d\alpha = -\pi\log 2. \tag{5.84}$$

5.4.4 The solution for a generic point load

Since the perturbation problem is linear, the solution pertaining to a generic point load can be obtained as the superposition of the solutions for two forces, one acting along axis 1 and the other along axis 2,

$$\begin{cases} u_1(\boldsymbol{x}) = f_1 G_{11}(\boldsymbol{x} - \boldsymbol{x}_0) + f_2 G_{12}(\boldsymbol{x} - \boldsymbol{x}_0), \\[2mm] u_2(\boldsymbol{x}) = f_1 G_{21}(\boldsymbol{x} - \boldsymbol{x}_0) + f_2 G_{22}(\boldsymbol{x} - \boldsymbol{x}_0), \end{cases} \tag{5.85}$$

where $\boldsymbol{x}_0$ is the application point and f_1, f_2 the components of the load. Using polar coordinates

$$\begin{cases} u_1(r,\theta) = f_1 G_{11}(\hat{r}, \hat{\theta}) + f_2 G_{12}(\hat{r}, \hat{\theta}), \\[2mm] u_2(r,\theta) = f_1 G_{21}(\hat{r}, \hat{\theta}) + f_2 G_{22}(\hat{r}, \hat{\theta}), \end{cases} \tag{5.86}$$

where

$$\begin{cases} \hat{r} = \sqrt{r^2 + r_0^2 - 2rr_0\cos(\theta - \theta_0)}, \\[3mm] \hat{\theta} = \tan^{-1}\dfrac{r\cos\theta - r_0\cos\theta_0}{r\sin\theta - r_0\sin\theta_0}, \end{cases} \tag{5.87}$$

in which r,θ and r_0,θ_0 are the polar coordinates of $\boldsymbol{x}$ and $\boldsymbol{x}_0$ respectively.

5.5   Results

5.5.1   Normalization

Introducing any characteristic length a, we can normalize the following equation

$$\mathbb{C}_{ijkl}\frac{\partial^2 G_{kp}(\boldsymbol{x})}{\partial x_j \partial x_l} + \rho_0\omega^2 G_{ip}(\boldsymbol{x}) + \delta_{ip}\delta(\boldsymbol{x}) = 0, \quad \boldsymbol{x} \in \mathbf{R}^2 \qquad (5.88)$$

by writing it in terms of the dimensionless quantities $\bar{\boldsymbol{x}} = \boldsymbol{x}/a$ and $\bar{\boldsymbol{G}}(\bar{\boldsymbol{x}}) = \mu\boldsymbol{G}(a\bar{\boldsymbol{x}})$ as follows

$$\bar{\mathbb{C}}_{ijkl}\frac{\partial^2 \bar{G}_{kp}(\bar{\boldsymbol{x}})}{\partial \bar{x}_j \partial \bar{x}_l} + \bar{\omega}^2 \bar{G}_{ip}(\bar{\boldsymbol{x}}) + \delta_{ip}\delta(\bar{\boldsymbol{x}}) = 0, \quad \bar{\boldsymbol{x}} \in \mathbf{R}^2 \qquad (5.89)$$

where

$$\bar{\mathbb{C}}_{ijkl} = \frac{\mathbb{C}_{ijkl}}{\mu}, \quad \bar{\omega} = a\sqrt{\frac{\rho_0}{\mu}}\omega, \qquad (5.90)$$

and we have made use of the property

$$\delta(a\bar{\boldsymbol{x}}) = \frac{1}{a^2}\delta(\bar{\boldsymbol{x}}), \quad \bar{\boldsymbol{x}} \in \mathbf{R}^2. \qquad (5.91)$$

Thus, the dimensionless Green tensor reads

$$\bar{\boldsymbol{G}}(\bar{\boldsymbol{x}}) = -\frac{1}{8\pi^2}\sum_{N=1}^{2}\int_{|\boldsymbol{n}|=1}\Big[2\cos(\bar{k}_N\boldsymbol{n}\cdot\bar{\boldsymbol{x}})\,\mathrm{Ci}(\bar{k}_N|\boldsymbol{n}\cdot\bar{\boldsymbol{x}}|) \qquad (5.92)$$

$$+ 2\sin(\bar{k}_N\boldsymbol{n}\cdot\bar{\boldsymbol{x}})\,\mathrm{Si}(\bar{k}_N\boldsymbol{n}\cdot\bar{\boldsymbol{x}}) - i\,\pi\cos(\bar{k}_N\boldsymbol{n}\cdot\bar{\boldsymbol{x}})\Big]\frac{\boldsymbol{v}_N\otimes\boldsymbol{w}_N}{\bar{c}_N^2}\,ds,$$

where

$$\bar{k}_N = ak_N = \frac{\bar{\omega}}{\bar{c}_N}, \quad \bar{c}_N = \sqrt{\frac{\rho_0}{\mu}}c_N, \qquad (5.93)$$

so that $\bar{c}_N^2$ are the eigenvalues of the dimensionless acoustic tensor $\bar{\boldsymbol{A}} = \boldsymbol{A}/\mu$.

5.5.2   Green's tensor

In this section we analyze the singular solution previously obtained.

As a reference we consider the case shown in Fig. 5.9, in which the material is subject to uniaxial traction, $\sigma_1/\mu = 1$, $\sigma_2 = \sigma_3 = 0$, and the direction of the axis of elastic symmetry is inclined at $\theta_\sigma = 15°$ with respect to the stress principal direction $\boldsymbol{k}_1$. The material parameters are $\lambda/\mu = 1$, $\hat{b} = 80°$,

$\psi = 30°$, and $\chi = 0°$. The Green's tensor components have been computed for $\bar{\omega} = a\sqrt{\rho_0/\mu}\,\omega = 1$ and for three values of the plastic modulus H/μ, namely 3, 2, and 1.23, in order to approach the onset of flutter.

The results are plotted along radial lines inclined at $\theta = 0, 45, 90, -14.56°$ with respect to the axis x_1, in Figs. 5.11, 5.12, 5.13, 5.14, respectively.

5.5.3   Dipole

The singular solution previously obtained can be used to analyze the effects of a perturbation superimposed upon a given homogeneus deformation of an infinite body. The simplest self-equilibrated perturbation is a dipole, corresponding to two equal and opposite forces. In particular we consider two equal and opposite unit forces acting at a distance $2a$ and inclined at $\beta = 45°$ with respect to axis x_1, as shown in Fig. 5.10. For this loading system, the
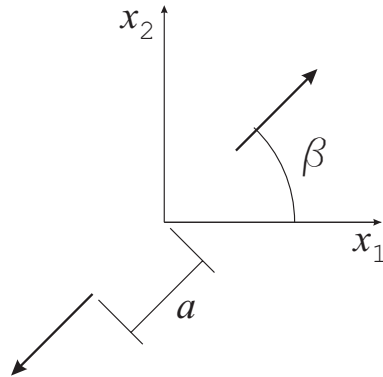
Figure 5.10: Geometry of the dipole.

displacements components u_1 and u_2 have been computed.

Once again we refer to the case shown in Fig. 5.9. Solutions have been calculated for $\bar{\omega} = a\sqrt{\rho_0/\mu}\,\omega = 1$ and for three values of the plastic modulus H/μ, namely 3, 2, and 1.23, in order to approach the onset of flutter. The results are plotted along radial lines inclined at $\theta = 0, 45, 90, -14.56°$ with respect to the axis x_1, in Figs. 5.15 and 5.16.

These figures clearly show that the response of the infinite body to the dynamic perturbation remains bounded and the flutter instability remains undetected until the eigenvalues lie in the real range. Figures 5.17 and 5.18

show the level sets of displacement component u_1 and u_2, respectively.

5.5.4   An evidence of flutter instability in the complex range

So far flutter instability has been investigated restricting the analysis to the situation in which the eigenvalues of the acoustic tensor are still real and approaching the onset of the instability, which corresponds to the coalescence of two eigenvalues. It has been shown that the response of an infinite body to a dynamic perturbation remains bounded and the flutter instability remains undetected until the eigenvalues lie in the real range, while a blow-up of the solution is expected within the complex range.

In order to gain some insight and substantiate this claim, a study of flutter instability in the complex range has been carried out, employing the solution obtained in the real range.

We refer again to the case shown in Fig. 5.9. Solutions have been calculated for $\bar{\omega} = a\sqrt{\rho_0/\mu}\,\omega = 1$ and for three values of the plastic modulus H/μ, namely 1.23, 0.4, and 0.32, the first of which corresponds to a situation close to the onset of flutter, but still in the real range, whereas the other two values have been selected in order to have two complex conjugate eigenvalues of the acoustic tensor. In particular, two eigenvalues are complex conjugate in the range of directions $-17.16° < \theta_n < -10.34°$ for $H/\mu = 0.4$, and $-17.10° < \theta_n < -10.79°$ for $H/\mu = 0.32$. The results are plotted along radial lines inclined at $\theta = 0, 45, 90, -14.56°$ with respect to the axis x_1, in Figs. 5.19 and 5.20.

It can be noted that the solutions corresponding to $H/\mu = 0.4$ and $H/\mu = 0.32$ blow up with distance along the radial lines inclined at $\theta = 0°$ and $\theta = -14.56°$, whereas they seem to remain bounded along the radial lines inclined at $\theta = 45°$ and $\theta = 90°$, at least for the range of distance analyzed, which is $0 < r/a < 25$. This suggest that flutter phenomena present well-defined directional properties, that will be important to investigate. The knowledge of the directionality of flutter will in fact shed light on its mechanical interpretation.

real part   imaginary part
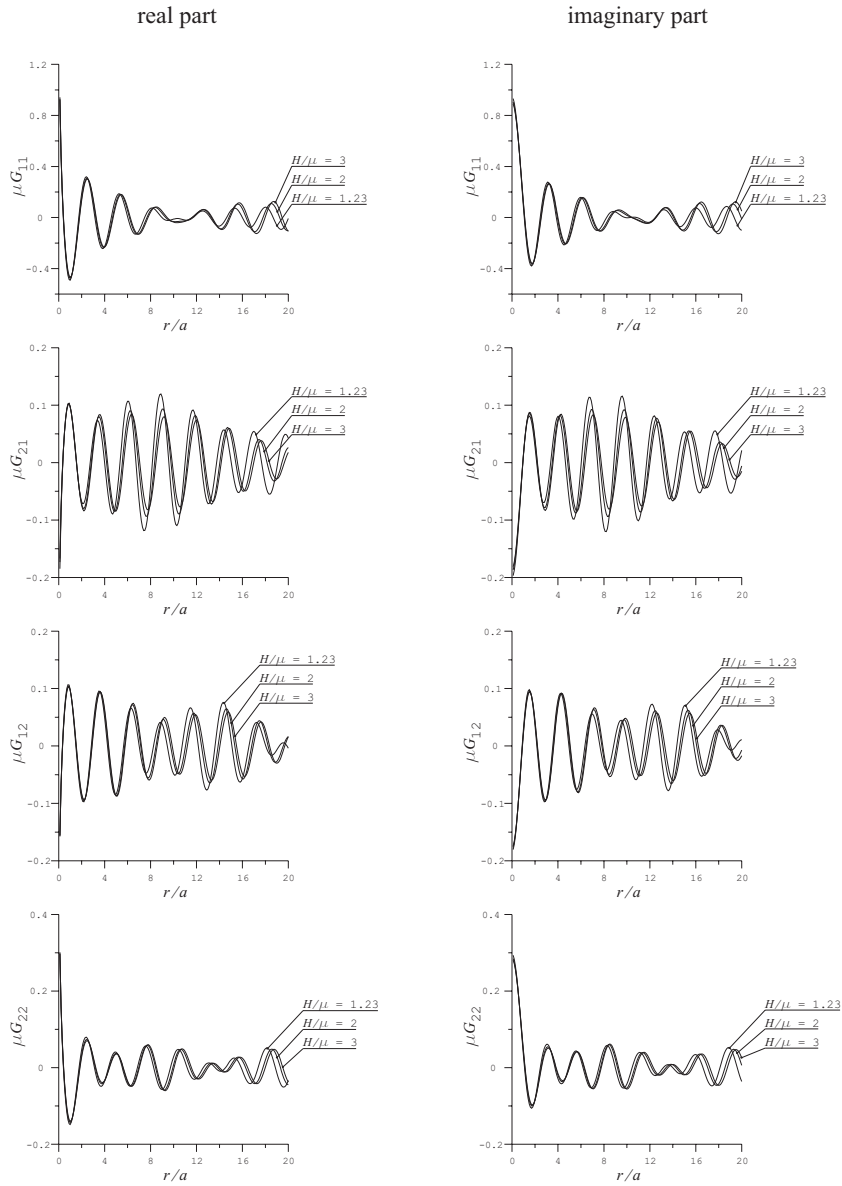
Figure 5.11: Dimensionless Green's tensor components along axis x_1, $\theta = 0°$. The onset of flutter is approached as the plastic modulus H/μ decreases.
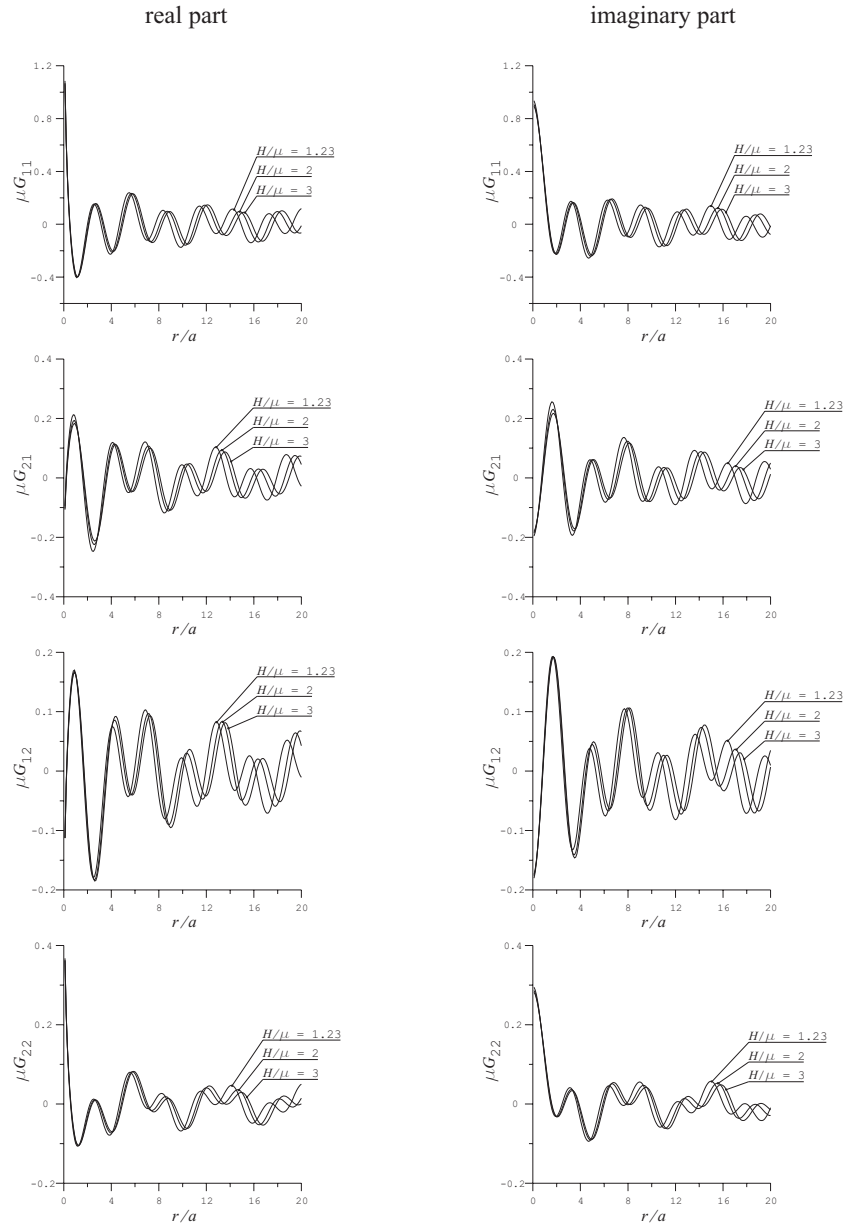
Figure 5.12: Dimensionless Green's tensor components along a radial line inclined at $\theta = 45°$. The onset of flutter is approached as the plastic modulus H/μ decreases.

real part imaginary part
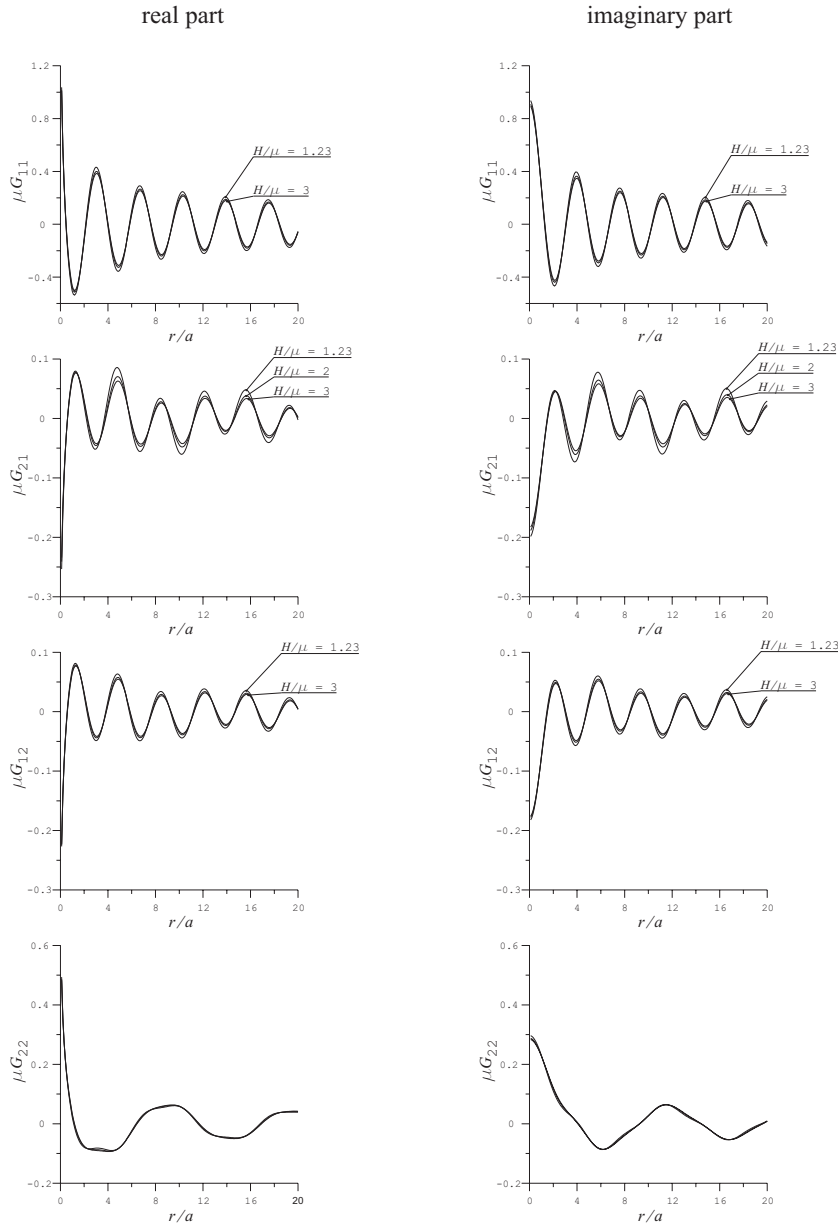
Figure 5.13: Dimensionless Green's tensor components along axis x_2, $\theta = 90°$. The onset of flutter is approached as the plastic modulus H/μ decreases.

real part   imaginary part
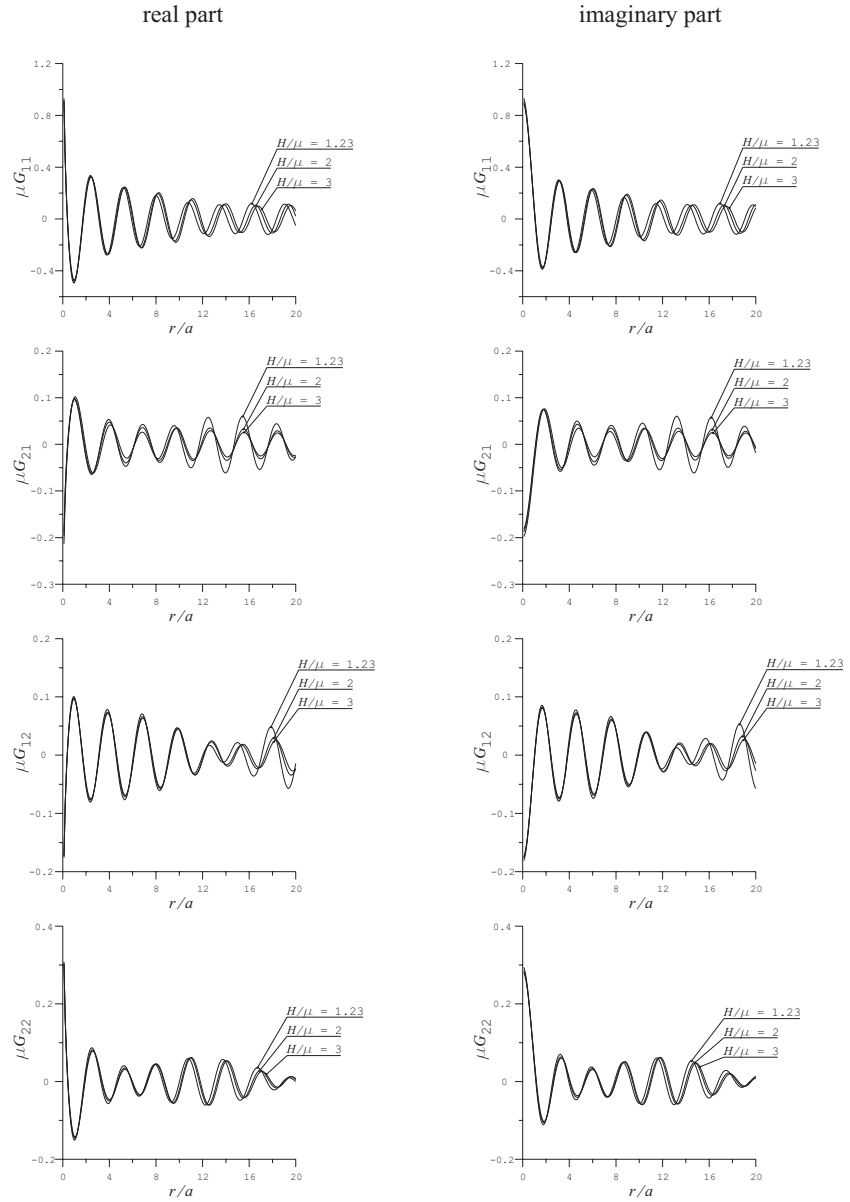
Figure 5.14: Dimensionless Green's tensor components along a radial line inclined at $\theta = -14.56°$. The onset of flutter is approached as the plastic modulus H/μ decreases.
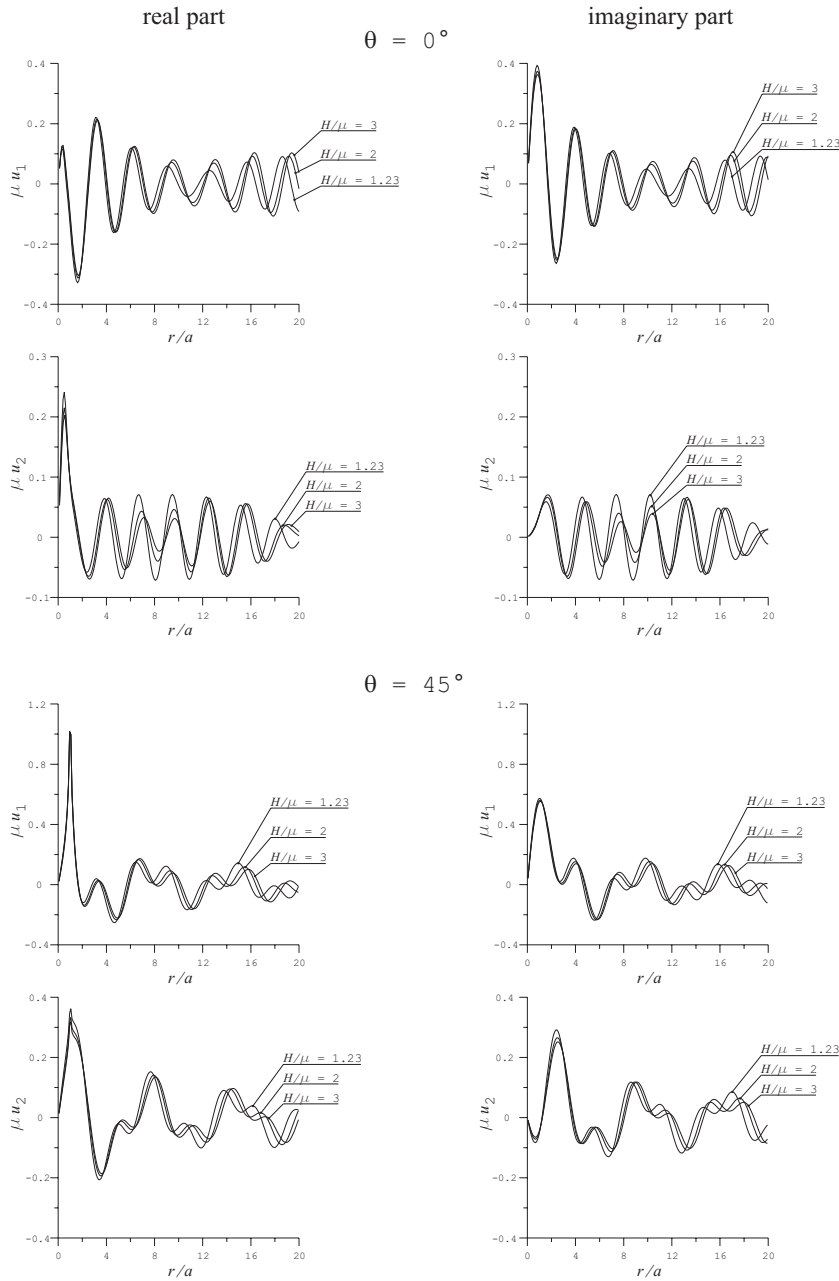
Figure 5.15: Dimensionless displacement components along axis x_1, $\theta = 0°$, and along a radial line inclined at $\theta = 45°$, for a dipole inclined at $\beta = 45°$. The onset of flutter is approached as the plastic modulus H/μ decreases.
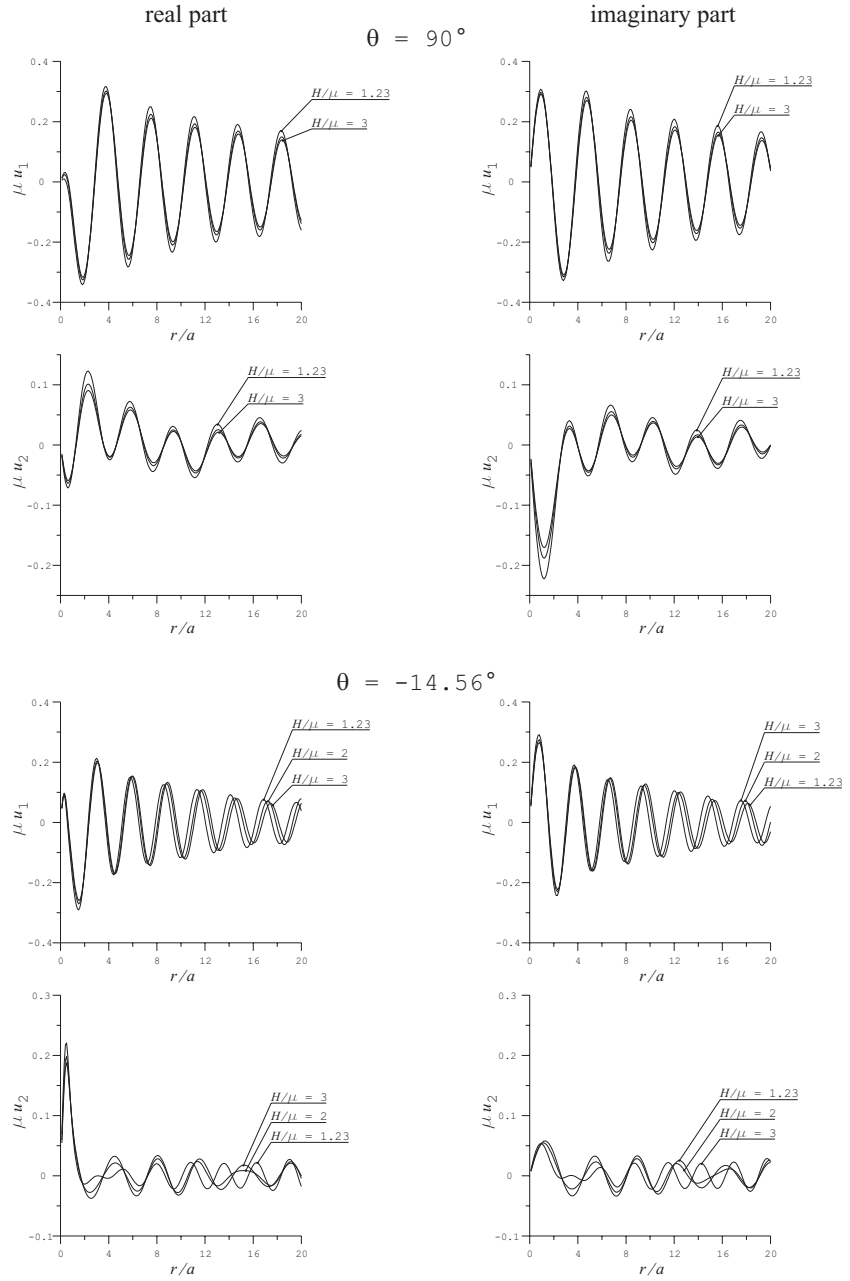
Figure 5.16: Dimensionless displacement components along axis x_2, $\theta = 90°$, and along a radial line inclined at $\theta = -14.56°$, for a dipole inclined at $\beta = 45°$. The onset of flutter is approached as the plastic modulus H/μ decreases.

real part u_1 imaginary part
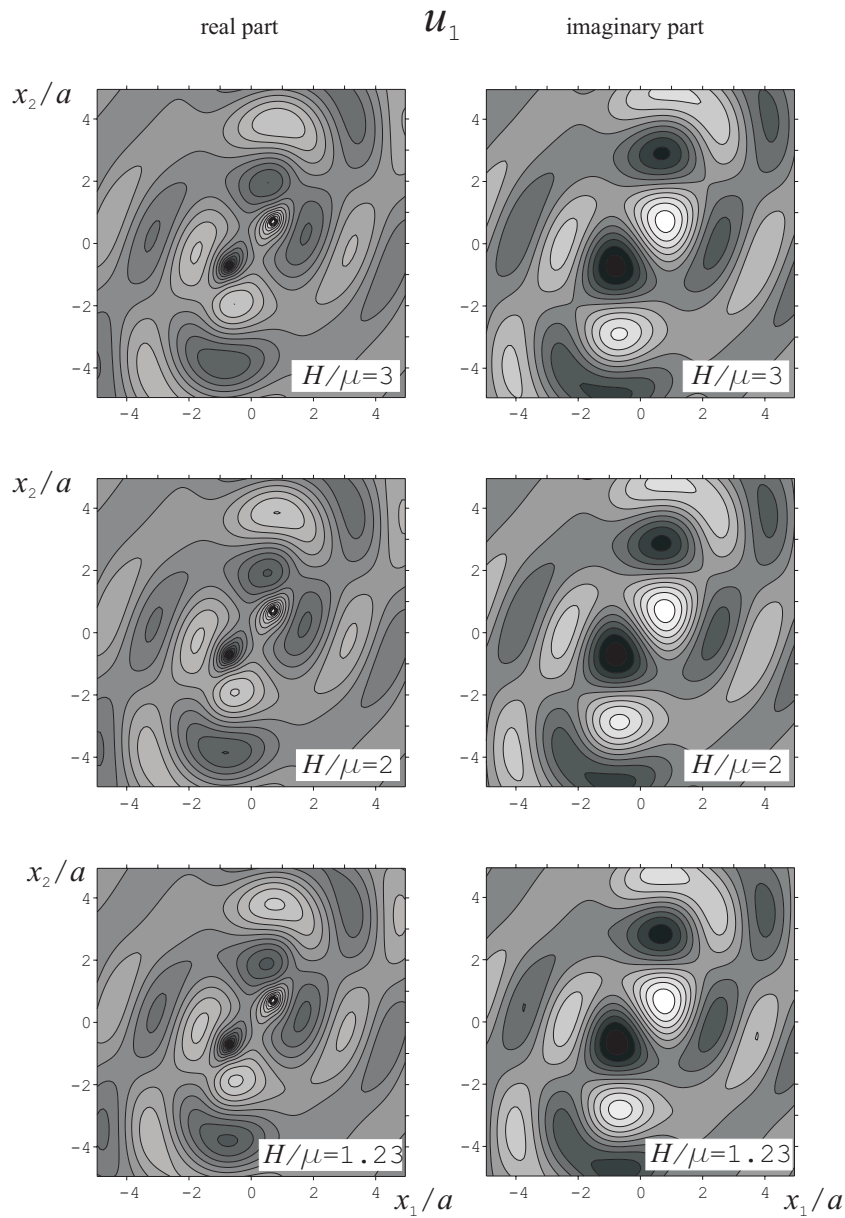
Figure 5.17: Level sets of displacement component u_1, for a dipole inclined at $\beta = 45°$. The onset of flutter is approached as the plastic modulus H/μ decreases.

real part u_2 imaginary part
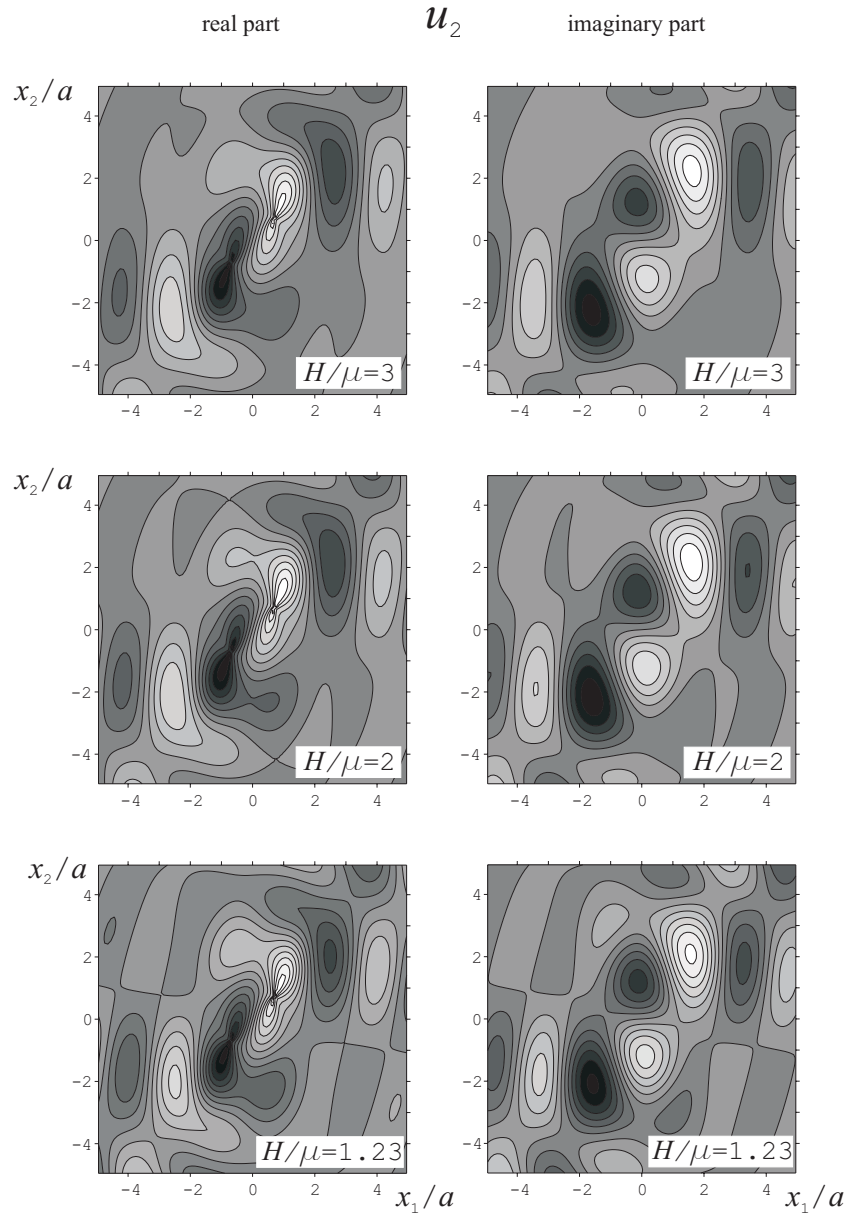
Figure 5.18: Level sets of displacement component u_2, for a dipole inclined at $\beta = 45°$. The onset of flutter is approached as the plastic modulus H/μ decreases.

real part   imaginary part

$\theta = 0°$

$\theta = 45°$
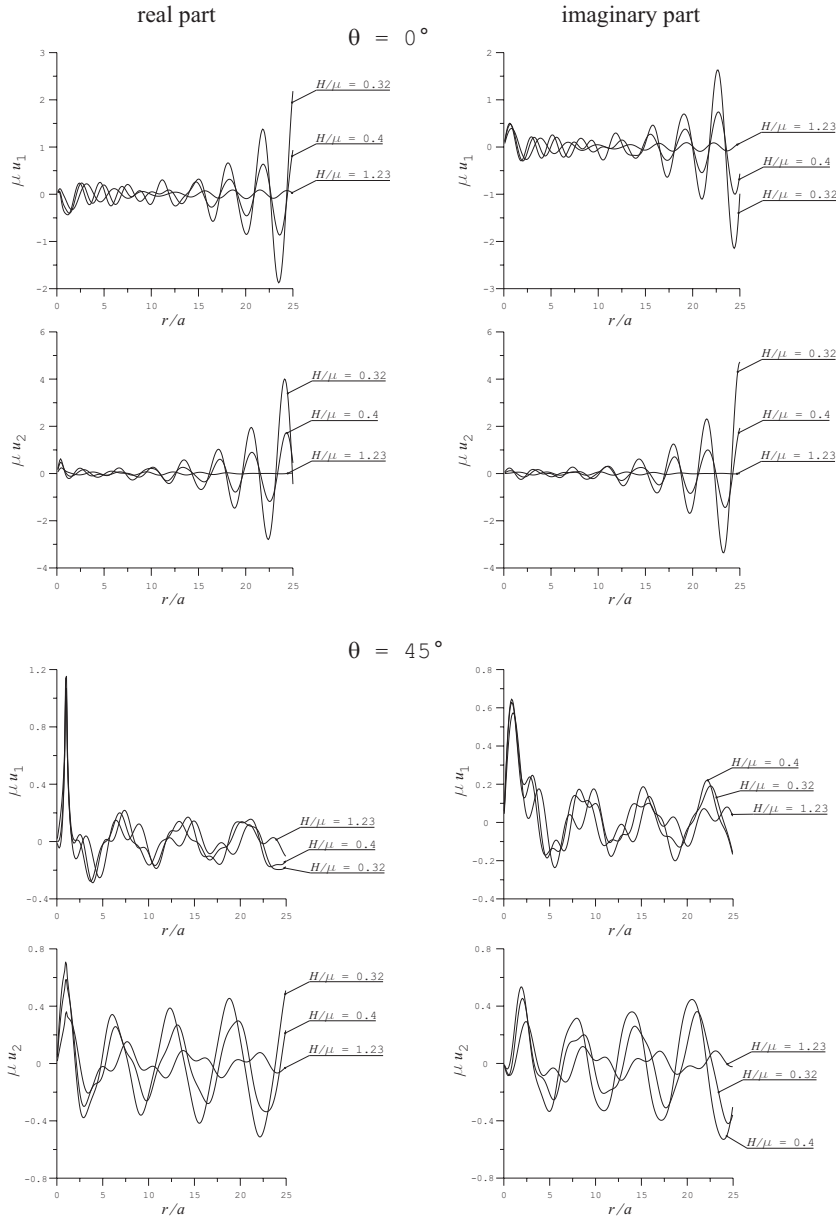
Figure 5.19: Dimensionless displacement components along axis x_1, $\theta = 0°$, and along a radial line inclined at $\theta = 45°$, for a dipole inclined at $\beta = 45°$.

real part   imaginary part

$\theta = 90°$
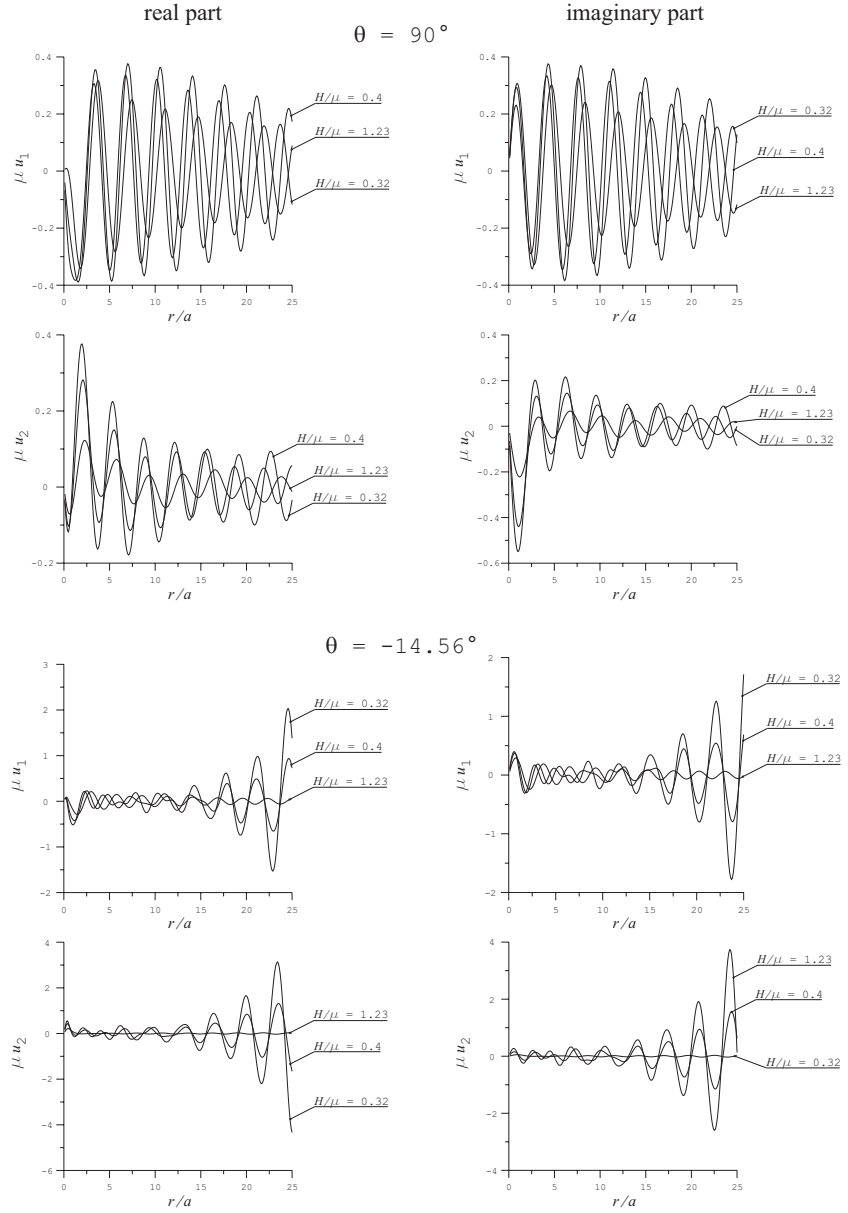
$\theta = -14.56°$

Figure 5.20: Dimensionless displacement components along axis x_2, $\theta = 90°$, and along a radial line inclined at $\theta = -14.56°$, for a dipole inclined at $\beta = 45°$.

References

Altenbach, H. and Tushtev, K. (2001) A new static failure criterion for isotropic polymers. *Mech. Compos. Mater.* **37**, 475-482.

An, L. and Schaeffer, D. (1990) The flutter instability in granular flow. *J. Mech. Phys. Solids* **40**, 683-698.

Argyris, J.H., Faust, G., Szimmat, J., Warnke, P. and Willam, K. (1974) Recent developments in the finite element analysis of prestressed concrete reactor vessels. *Nucl. Eng. Des.* **28**, 42-75.

Bardet, J.P. (1990) Lode dependences for isotropic pressure-sensitive elastoplastic materials. *J. Appl. Mech.* **57**, 498-506.

Bigoni, D. (1995) On flutter instability in elastoplastic constitutive models. *Int. J. Solids Struct.* **32**, 3167-3189.

Bigoni, D. (2000) Bifurcation and instability of non-associative elasticplastic solids. In *CISM Lecture Notes No. 414, Material instabilities in elastic and plastic solids*, Petryk, H. Ed., pp.1-52, Springer-Verlag, WienNew York.

Bigoni, D. and Capuani, D. (2002) Green's function for incremental nonlinear elasticity: shear bands and boundary integral formulation. *J. Mech. Phys. Solids* **50**, 471-500.

Bigoni, D. and Hueckel, T. (1991) Uniqueness and localization — I. Associative and non-associative elastoplasticity. *Int. J. Solids Struct.* **28**, 197-213.

Bigoni, D. and Loret, B. (1999) Effects of elastic anisotropy on strain localization and flutter instability in plastic solids. *J. Mech. Phys. Solids* **47**, 1409-1436.

Bigoni, D. and Petryk, H. (2002) A note on divergence and flutter instabilities in elastic-plastic materials. *Int. J. Solids Struct.* **39**, 911-926.

Bigoni, D. and Piccolroaz, A. (2004) Yield criteria for quasibrittle and frictional materials. *Int. J. Solids Struct.* , in press.

Bigoni, D. and Zaccaria, D. (1994) On eigenvalues of the acoustic tensor in elastoplasticity. *Eur. J. Mech. A-Solid.* **13**, 621-638.

Bishop, J.F.W. and Hill, R. (1951) A theory of the plastic distorsion of a polycrystalline aggregate under combined stresses. *Phil. Mag.* **42**, 414-427.

Bonnefoy, V. (2001) Modeling of metallic and ceramic powders compaction behavior. PhD thesis, Institut National Polytechnique de Grenoble, France.

Bortzmeyer, D. (1996) Die pressing and isostatic pressing. In *Materials Science and Technology*, Cahn, R.W., Haasen, P. and Kramer, E.J. Eds., vol. 17A, pp.127-152, VCH, Weinheim.

Brown, S.B. and Weber, G.A. (1988) A constitutive model for the compaction of metal powders. *Mod. Dev. Powder Metall.* **18-21**, 465-476.

Capurso, M. (1979) Extremum theorems for the solution of the rate problem in elastic-plastic fracturing structures. *J. Struct. Mech.* **7**, 411-434.

Chen, W.F. and Saleeb, A.F. (1982) *Constitutive equations for engineering materials: elasticity and modelling.* Wiley & Sons, New York.

Christensen, R.M. (1997) Yield functions/failure criteria for isotropic materials. *Proc. R. Soc. Lond.* **453**, 1473-1491.

Christensen, R.M., Freeman, D.C. and DeTeresa, S.J. (2002) Failure criteria for isotropic materials, applications to low-density types. *Int. J. Solids Struct.* **39**, 973-982.

Coffin, L.F. and Schenectady, N.Y. (1950) The flow and fracture of a brittle material. *J. Appl. Mech.* **17**, 233-248.

Cooper, A.R. and Eaton, L.E. (1962) Compaction behavior of several ceramic powders. *J. Am. Ceram. Soc.* **45**, 97-101.

De Finetti, B. (1949) Sulle stratificazioni convesse. *Ann. Mat. Pur. Appl.* **30**, 173-183.

Deis, T.A. and Lannutti, J.J. (1998) X-ray computed tomography for evaluation of density gradient formation during the compaction of spray-dried granules. *J. Am. Ceram. Soc.* **81**, 1237-1247.

Deshpande, V.S. and Fleck, N.A. (2000) Isotropic constitutive models for metallic foams. *J. Mech. Phys. Solids* **48**, 1253-1283.

Dougill, J.W. (1976) On stable progressively fracturing solids. *Z. Angew. Math. Phys.* **27**, 423-437.

Drucker, D.C. (1953) Limit analysis of two and three dimensional soil mechanics problems. *J. Mech. Phys. Solids* **1**, 217-226.

Drucker, D.C. (1956) On uniqueness in the theory of plasticity. *Quart. Appl. Math.* **XIV**, 35-42.

Drucker, D.C. (1964) On the postulate of stability of material in the mechanics of continua. *J. Mécanique* **3**, 235-249.

Duvaut, G. and Lions, J.L. (1976) *Inequalities in mechanics and physics.* Springer-Verlag, Berlin.

Eekelen, H.A.M. (1980) Isotropic yield surface in three dimensions for use in soil mechanics. *Int. J. Numer. Anal. Meth. Geomech.* **4**, 89-101.

Ehelers, W. (1995) A single-surface yield function for geomaterials. *Arch. Appl. Mech.* **65**, 246-259.

Ekeland, I. and Temam, R. (1976) *Convex analysis and variational problems.* North-Holland, Amsterdam.

Ewsuk, K.G. (1997) Compaction science and technology. *MRS Bull.* **22**, 14-16.

Franchi, A., Genna, F. and Paterlini, F. (1990) Research note on quasi-convexity of the yield function and its relation to Drucker postulate. *Int. J. Plasticity* **6**, 369-375.

Gajo, A., Bigoni, D. and Wood, D.M. (2004) Strain localization and band saturation in sand. *In preparation.*

German, R.M. (1984) *Powder Metallurgy Science.* MPIF, Princeton, New Jersey.

Glass, S.J. and Ewsuk, K.G. (1997) Ceramic powder compaction. *MRS Bull.* **22**, 24-28.

Gudehus, G. (1973) Elastoplastische Stoffgleichungen für trockenen Sand. *Ing. Arch.* **42**, 151-169.

Gurson, A.L. (1977) Continuum theory of ductile rupture by void nucleation and growth: part I, yield criteria and flow rules for porous ductile media. *ASME J. Eng. Mater. Tech.* **99**, 2-15.

Hausner, H.H. and Kumar-Mal, M. (1982) *Handbook of Powder Metallurgy.* Chemical Publishing.

Haythornthwaite, R.M. (1985) A family of smooth yield surfaces. *Mech. Res. Commun.* **12**, 87-91.

Hibbitt, Karlsson & Sorensen (2001) *ABAQUS Theory & User's Manuals*, Release 6.2, Pawtucket, RI, USA.

Hill, R. (1950a) *The mathematical theory of plasticity.* Clarendon Press, Oxford.

Hill, R. (1950b) Inhomogeneous deformation of a plastic lamina in a compression test. *Phil. Mag.* **41**, 733-744.

Hill, R. (1967a) The essential structure of constitutive laws for metal composites and polycrystals. *J. Mech. Phys. Solids* **15**, 79-95.

Hill, R. (1967b) On the classical constitutive laws for elastic/plastic solids. In *Recent progress in applied mechanics, The Folke Odkvist volume*, Broberg, B. Ed., pp.241-249, Almqvist & Wiksell, Stockholm.

Hill, R. (1968) On constitutive inequalities for simple materials-I. *J. Mech. Phys. Solids* **16**, 229-242.

Hill, R. (1978) Aspects of invariance in solid mechanics. In *Advances in applied mechanics*, Yih, C.-S. Ed., vol. 18, pp.1-75, Academic Press, New York.

Hill, R. and Rice, J.R. (1973) Elastic potentials and the structure of inelastic constitutive laws. *SIAM J. Appl. Math.* **25**, 448-461.

Hisieh, S.S., Ting, E.C. and Chen, W.F. (1982) A plasticity-fracture model for concrete. *Int. J. Solids Struct.* **18**, 181-197.

Hoek, E. and Brown, E.T. (1980) *Underground excavations in rock.* The Institution of Mining and Metallurgy, London.

Hoger, A. (1987) The stress conjugate to logarithmic strain. *Int. J. Solids Struct.* **23**, 1645-1656.

Hueckel, T. (1976) Coupling of elastic and plastic deformation of bulk solids. *Meccanica* **11**, 227-235.

Hueckel, T. and Maier, G. (1977) Incremental boundary value problems in the presence of coupling of elastic and plastic deformations: a rock mechanics oriented theory. *Int. J. Solids Struct.* **13**, 1-15.

Jaky, J. (1944) The coefficient of earth pressure at Rest. *J. Soc. Hungarian Arch.* , 355-358.

Kim, H.G., Gillia, O., Dorémus, P. and Bouvard, D. (2002) Near net shape processing of a sintered alumina component: adjustment of pressing parameters through finite element simulation. *Int. J. Mech. Sci.* **44**, 2523-2539.

Kim, K.T., Choi, S.W. and Park, H. (2000) Densification behavior of ceramic powder under cold compaction. *ASME J. Eng. Mater. Tech.* **122**, 238-244.

Lade P.V. (1997) Modelling the strengths of engineering materials in three dimensions. *Mech. Cohes-Frict. Mat.* **2**, 339-356.

Lade, P.V. and Kim, M.K. (1995) Single hardening constitutive model for soil, rock and concrete. *Int. J. Solids Struct.* **32**, 1963-1978.

Laroussi, M., Sab, K. and Alaoui, A. (2002) Foam mechanics: nonlinear response of an elastic 3D-periodic microstructure. *Int. J. Solids Struct.* **39**, 3599-3623.

Lee, E.H. (1969) Elastic-plastic deformation at finite strains. *J. Appl. Mech.* **36**, 1-6.

Lin, F.-B. and Bazant, Z. (1986) Convexity of smooth yield surface of frictional material. *ASCE J. Eng. Mech.* **112**, 1259-1262.

Lode, W. (1926) Versuche über den Einfluß der mittleren Hauptspannung auf das Fließen der Metalle Eisen Kupfer und Nickel. *Z. Phys.* **36**, 913-939.

Lordi, N.G. and Cuitiño, A.M. (1997) Compaction of pharmaceuticals. *MRS Bull.* **22**, 34-37.

Loret, B. (1992) Does deviation from deviatoric associativity lead to the onset of flutter instability? *J. Mech. Phys. Solids* **40**, 1363-1375.

Loret, B., Simões, F.M.F. and Martins, J.A.C. (2000) Flutter instability and ill-posedness in solids and fluid-saturated porous media. In *CISM Lecture Notes No. 414, Material instabilities in elastic and plastic solids*, Petryk, H. Ed., pp.109-207, Springer-Verlag, WienNew York.

Maier, G. and Hueckel, T. (1979) Non-associated and coupled flow-rules of elastoplasticity for rock-like materials. *Int. J. Rock Mech. Min. Sci.* **16**, 77-92.

Mandel, J. (1966) Contribution theorique a l'etude de l'ecrouissage et des lois de l'ecoulement plastique. Proc. 11th Int. Congr. Appl. Mech. (Munich 1964), pp.502-509, Springer-Verlag.

Matsumoto, R.K.L. (1986) Generation of powder compaction response diagrams. *Comm. Am. Cer. Soc.* **69**, C-246-247.

Matsuoka, H. and Nakai, T. (1977) Stress-strain relationship of soil based on the "SMP". Proc. Specialty Session 9, IX ICSMFE, pp.153-162, Tokyo.

Mollica, F. and Srinivasa, A.R. (2002) A general framework for generating convex yield surfaces for anisotropic metals. *Acta mater.* **154**, 61-84.

Naghdi, P.M., Essenburg, F. and Koff, W. (1958) An experimental study of initial and subsequent yield surfaces in plasticity. *J. Appl. Mech.* **25**, 201-209.

Naghdi, P.M. and Srinivasa, A.R. (1994) Some general results in the theory of crystallographic slip. *Z. Angew. Math. Phys.* **45**, 687-732.

Menétrey, Ph. and Willam, K.J. (1995) Triaxial failure criterion for concrete and its generalization. *ACI Struct. J.* **92**, 311-318.

Mróz, Z. (1963) Non-associated flow laws in plasticity. *J. Mécanique* **2**, 21-42.

Mróz, Z. (1966) On forms of constitutive laws for elastic-plastic solids. *Arch. Mech. Stosowanej* **18**, 1-34.

Newman, K. and Newman, J.B. (1971) Failure theories and design criteria for plain concrete. In *Structure, Solid Mechanics and Engineering Design*, Proc. 1969 Southampton Civil Engineering Conf., Te'eni, M. Ed., pp.963-995, Wiley Interscience, New York.

Ol'khovik, O. (1983) Apparatus for testing of strength of polymers in a three-dimensional stressed state. *Mech. Compos. Mater.* **19**, 270-275.

Ogden, R.W. (1984) *Non-linear elastic deformations.* Ellis Horwood, Chichester.

Ortiz, M. and Simo, J.C. (1986) An analysis of a new class of integration algorithms for elastoplastic constitutive relations. *Int. J. Numer. Meth. Eng.* **23**, 353-366.

Ottosen, N.S. (1977) A failure criterion for concrete. *ASCE J. Eng. Mech. Div.* **103**, 527-535.

Paul, B. (1968) Macroscopic criteria for plastic flow and brittle fracture. In *Fracture, an advanced treatise*, Liebowitz, H. Ed., vol. I, pp.313-496, Academic Press, New York.

Phillips, A. (1974) Experimental plasticity. Some thoughts on its present status and possible future trends. In *Symposium on the foundations of plasticity* (Warsaw, 1972), Sawczuk, A.A. Ed., pp.193-233, Nordhoff International Publishing, Leyden.

Petryk, H. (2000) General conditions for uniqueness in materials with multiple mechanisms of inelastic deformation. *J. Mech. Phys. Solids* **48**, 367-396.

Piccolroaz, A., Gajo, A. and Bigoni, D. (2002) Forming of advanced ceramics. In *Selected mechanical problems in structural ceramics*, Bigoni, D. Ed., pp.81-115, Polish Academy of Sciences, Warsaw.

Piccolroaz, A., Gajo, A. and Bigoni, D. (2003) Cold compaction of ceramic powders. *Mater. Eng.* **14**, 157-170.

Reed, J.S. (1995) *Principles of Ceramic Processing*. Wiley & Sons, New York.

Rice, J.R. (1977) The localization of plastic deformation. In *Theoretical and Applied Mechanics*, Koiter, W.T. Ed., pp.207-220, North-Holland, Amsterdam.

Roberts, A.W. and Varberg, D.E. (1973) *Convex functions*. Academic Press, New York.

Roscoe, K.H. and Burland, J.B. (1968) On the generalized stress-strain behaviour of 'wet' clay. In *Engineering Plasticity*, Heyman, J. and Leckie, F.A. Eds., Cambridge University Press, Cambridge.

Roscoe, K.H. and Schofield, A.N. (1963) Mechanical behaviour of an idealised 'wet' clay. Proc. European Conf. on Soil Mechanics and Foundation Engineering, Wiesbaden (Essen: Deutsche Gesellshaft für Erd- und Grundbau e. V.), vol. 1, pp.47-54.

Rowe, P.W. (1962) The stress dilatancy relation for static equilibrium of an assembly of particles in contact. *Proc. R. Soc. Lond. A* **269**, 500-527.

Rudnicki, J.W. and Rice, J.R. (1975) Conditions for the localization of deformations in pressure-sensitive dilatant materials. *J. Mech. Phys. Solids* **23**, 371-394.

Sansour, C. (2001) On the dual variable of the logarithmic strain tensor, the dual variable of the Cauchy stress tensor, and related issues. *Int. J. Solids Struct.* **38**, 9221-9232.

Salençon, J. (1974) *Applications of the theory of plasticity in soil mechanics*. Wiley & Sons, Chichester.

Schofield, A.N. and Wroth, C.P. (1968) *Critical state soil mechanics*. McGraw-Hill Book Company, London.

Sfer, D., Carol, I., Gettu, R. and Etse, G. (2002) Study of the behaviour of concrete under triaxial compression. *ASCE J. Eng. Mech.* **128**, 156-163.

Shield, R.T. (1955) On Coulomb's law of failure in soils. *J. Mech. Phys. Solids* **4**, 10-16.

Simo, J.C. and Hughes, T.J.R. (1987) General return mapping algorithms for rate-independent plasticity. In *Constitutive laws for engineering materials: theory and applications*, Desai, C.S. et al. Eds.

Simo, J.C. and Ortiz, M. (1985) A unified approach to finite deformation plasticity based on the use of hyperelastic constitutive equations. *Comput. Method. Appl. M.* **49**, 221-245.

Sridhar, I. and Fleck, N.A. (2000) Yield behaviour of cold compacted composite powders. *Acta mater.* **48**, 3341-3352.

Tasuji, M.E., Slate, F.O. and Nilson, A.H. (1978) Stress-strain response and fracture of concrete in biaxial loading. *ACI J.* **75**, 306-312.

Thompson, R.A. (1981b) Mechanics of powder pressing: II, Finite-element analysis of end-capping in pressed green powders. *Am. Ceram. Soc. Bull.* **60**, 244-247.

Truesdell, C. and Noll, W. (1965) The non-linear field theories of mechanics. In *Encyclopedia of Physics*, Flügge, S. Ed., vol. III/3, Springer-Verlag, Berlin.

Tvergaard, V. (1981) Influence of voids on shear band instabilities under plane strain conditions. *Int. J. Fracture* **17**, 389-407.

Tvergaard, V. (1982) On localization in ductile materials containing spherical voids. *Int. J. Fracture* **18**, 237-252.

Willam, K.J. and Warnke, E.P. (1975) Constitutive model for the triaxial behaviour of concrete. Presented at the seminar on Concrete structures subjected to triaxial stresses, pp.1-30, ISMES, Bergamo.

Willis, J.R. (1969) Some constitutive equations applicable to problems of large dynamic plastic deformation. *J. Mech. Phys. Solids* **23**, 405-419.

Willis, J.R. (1973) Self-similar problems in elastodynamics. *Phil. Trans. R. Soc. Lond. A* **274**, 435-491.

Willis, J.R. (1980) Polarization approach to the scattering of elastic waves— I. Scattering by a single inclusion. *J. Mech. Phys. Solids* **28**, 287-305.

Willis, J.R. (1991) Inclusions and cracks in constrained anisotropic media. In *Modern theory of anisotropic elasticity and applications*, Wu, J.J., Ting, T.C.T. and Barnett, D.M. Eds., pp.87-102, SIAM, Philadelphia. *J. Mech. Phys. Solids* **23**, 405-419.

Wood, D.M. (1990) *Soil behaviour and critical state soil mechanics.* Cambridge University Press, Cambridge.

Yang, W.H. (1980) A useful theorem for constructing convex yield functions. *J. Appl. Mech.* **47**, 301-303.

Yasufuku, N., Murata, H. and Hyodo, M. (1991) Yield characteristics of anisotropically consolidated sand under low and high stress. *Soils Found.* **31**, 95-109.

Zeuch, D.H., Grazier, J.M., Argüello, J.G. and Ewsuk, K.G. (2001) Mechanical properties and shear failure surfaces for two alumina powders in triaxial compression. *J. Mater. Sci.* **36**, 2911-2924.